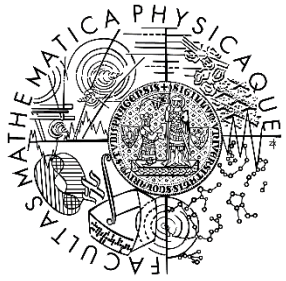

FACULTY
OF MATHEMATICS
AND PHYSICS
Charles University

DOCTORAL THESIS

František Čejka

Broadband kinematic ground motion modeling of tectonic earthquakes

Department of Geophysics

Supervisor of the doctoral thesis: prof. František Gallovič, PhD.

Study programme: Physics

Study branch: Physics of Earth and Planets

Prague 2024

I declare that I carried out this doctoral thesis independently, and only with the cited sources, literature and other professional sources. It has not been used to obtain another or the same degree.

I understand that my work relates to the rights and obligations under the Act No. 121/2000 Sb., the Copyright Act, as amended, in particular the fact that the Charles University has the right to conclude a license agreement on the use of this work as a school work pursuant to Section 60 subsection 1 of the Copyright Act.

In . . . . date . . . .

Author’s signature

There is one person I need to thank first: my supervisor, prof. František Gallovič, for his patience and guidance, which have been consistently present throughout my entire studies, from my bachelor's thesis to my Ph.D. journey. He is the person who is responsible for me standing here at this point in my life, presenting this work. Without his support through the years, I wouldn't be able to do this.

I want to thank my coauthors, especially Francesca Pacor and Sara Sgobba. Thanks to them and their projects, I was able to explore the issues presented here. They also hosted me twice at INGV Milano, and I won't forget the days spent there as they introduced me to their colleagues and their work in managing national seismic hazard.

I greatly enjoyed my time at the Department of Geophysics, its hospitality, and home-like environment. I spent almost 10 years there, and I am grateful to all the people I've met during that time. They are all very unique individuals, always ready to help and open to discussions about anything. The regular coffee breaks (apart from science discussions, of course) were a place for diverse worldviews that I enjoyed listening to and, as I grew into this community, also participating in. Special thanks go to prof. Jiří Zahradník, whom I secretly admired throughout the years for his never-ending positivity and excitement for seismology. He supported me through my studies with understanding and advice, and he always knew how to show me the joy within seismology. Another person who stands out is Ľubica, who was my collaborator on many projects, and she was always able to help me with anything I needed. Finally, there is a special group of people, my fellow students: Jakub, Jan, Libor, Martin, Burak, Vojtěch, and Filip, for being good friends both inside and outside academia; we made some unforgettable memories together.

I am thankful to my family, which grew bigger as I was doing my Ph.D. My wife and son both gave me the joy and energy to continue and not to give up. And my parents provided understanding that this was my path and supported me whenever I needed it.

My work was supported by several grants – Charles University project SVV 115–09/260581, grant SVV 260709 and the Czech Science Foundation (project 23-06345S). I also acknowledge the support from and the INGV "Ricerca Libera" 2021 project HSE-GMM ("A Hybrid Simulation-Empirical approach to model variability of ground motion in near-source region") and the project SECURE (Regional-Scale Earthquake Ground Motion PrediCtions ThroUgh Physics-based and EmpiRical ApproachEs: A Case study central Italy) within Pianeta Dinamico (Working Earth)—Geosciences for the Understanding of the Dynamics of the Earth and the Consequent Natural Risks (CUP code D53J19000170001) funded by the Italian Ministry of University and Research (MIUR).

Title: Broadband kinematic ground motion modeling of tectonic earthquakes

Author: František Čejka

Department: Department of Geophysics

Supervisor: prof. František Gallovič, Ph.D., Department of Geophysics

Abstract: Broadband earthquake ground motion simulations represent a promising approach to seismic hazard analysis. After validation of synthetics against recordings, it provides us the possibility to dense up the information needed to prepare accurate ground motion models. Here we develop broadband (0–10 Hz) kinematic source models of two disastrous events: 2016 Mw6.2 Amatrice in Italy and 2023 Mw7.8 Kahramanmaraş in Türkiye. The model utilizes integral and composite approaches to model rupture propagation at low and high frequencies, respectively. We adopt slip distribution, fault dimensions, and rupture velocity from available source inversions. First, we optimize those parameters by minimizing the spectral acceleration bias between modeled and recorded data at stations in the studied area. Then, we expand our models beyond the real stations by simulating ground motions at a grid of virtual stations and we test the robustness of the optimal model against a (nonergodic) ground motion model. For the Kahramanmaraş earthquake, we demonstrate that even a very rough estimate of major rupture parameters makes the ground motion simulations of such large events possible and may thus improve the efficiency of rapid, physics-based shaking estimation for emergency response and seismic hazard assessment. For the Amatrice earthquake, we use the set of virtual stations to model various scenarios of the event and study the ground motion variability by applying mixed-model analysis. Comparison with an empirical ground motion model (GMM) shows that the synthetic between-event variability exceeds the empirical value. We propose a way to restrict the scenario variability to conform with the empirical nonergodic GMM. The presented validation of the scenario variability can be generally utilized in scenario modeling for more realistic physics-based seismic hazard assessment.

Keywords: broadband ground motion modeling, kinematic earthquake source models, earthquake scenarios variability analysis

Název: Širokopásmové kinematické modelování seismických pohybů vyvolaných tektonickými zemětřeseními

Autor: František Čejka

Katedra: Katedra Geofyziky

Vedoucí dizertační práce: prof. František Gallovič, Ph.D., Katedra Geofyziky

Absrakt: Širokopásmové simulace zemětřesných pohybů představují slibný přístup k analýze seismického ohrožení. Po validaci syntetických dat pomocí reálných záznamů nám mohou umožnit získávat dodatečné informace potřebné k přípravě přesnějších modelů seismických pohybů. V této práci vytváříme širokopásmové (0–10 Hz) kinematické modely zdroje dvou katastrofických zemětřesení: Mw6,2 v Amatrice v Itálii v roce 2016 a Mw7,8 v Kahramanmaraş v Turecku z roku 2023. Použitý hybridní model zdroje kombinuje integrální a kompozitní přístupy k modelování na nízkých, respektive na vysokých frekvencích. Rozložení skluzu, rozměry zlomu a rychlost šíření trhliny přejímáme z dostupných inverzí zdroje. Další parametry nejprve optimalizujeme pomocí minimalizace odchylky spektrálního zrychlení mezi modelovanými a reálnými daty na stanicích ve studované oblasti. Poté náš model rozšíříme mimo reálné stanice na síť virtuálních stanic a testujeme robustnost optimálního modelu oproti (neergodickému) modelu zemětřesných pohybů. Na zemětřesení v Kahramanmaraşu demonstrujeme, že i velmi hrubý odhad hlavních parametrů zlomu umožňuje simulace seismických pohybů u takto velkých jevů a může tak zlepšit efektivitu rychlého, fyzikálně založeného, odhadu otřesů pro nouzové reakce a hodnocení seismického ohrožení. Pro zemětřesení v Amatrice využíváme soubor virtuálních stanic k modelování různých scénářů zemětřesení a zkoumáme variabilitu pohybů půdy pomocí vhodné statistické analýzy. Porovnání s empirickým modelem pohybu půdy ukazuje, že variabilita jevů vede k přecenění empirických hodnot. Navrhujeme způsob, jak omezit variabilitu scénářů tak, aby odpovídala empirickému neergodickému modelu. Předložené omezení variability scénářů může být obecně využito při jejich modelování pro fyzikálně realističtější hodnocení seismického ohrožení.

Klíčová slova: širokopásmové modelování pohybů půdy, kinematické modely zemětřesného zdroje, analýza variability scénářů zemětřesení

Contents

1. Introduction

1.1. Seismic hazard assessment

Seismic hazard assessment (SHA) plays a crucial role in understanding and mitigating the risks associated with earthquakes. It is a multidisciplinary field that integrates subjects as geology, tectonics, seismology, geodesy, statistics and engineering. By studying seismic hazards, scientists and engineers aim to develop strategies that enhance public safety and promote the design of resilient structures. Models developed for SHA encapsulates all facets of the earthquake process, the characteristics of the seismic source, the propagation of seismic waves, and the site-specific effects.

Over the years, seismic hazard assessment methods address ground shaking including their uncertainties by considering the seismotectonic setup of the area around the site and the available data on past earthquakes in the area. Those methods have evolved significantly and can be primarily divided into two methods:

Probabilistic seismic hazard assessment (PSHA) is a statistical method that considers full range of earthquake occurrence, e.g. their occurrence in time and space, their magnitude, source to site distances, tectonic features and ground motion prediction equations. Its first principles were introduced by Cornell (1969) and Esteva (1969). PSHA is typically considered a model that combines multiple component models with their uncertainty producing a hazard result.

Building such a model needs the following three main ingredients:

1. Seismicity rate model (SRM) including identification of possible earthquake sources.
2. Prediction of ground motion intensity as a function of earthquake magnitude, distance etc.
3. Uncertainty models for above mentioned ingredients.

For creating a SRM we need to make an assumption that future will look like the past (Gerstenberger et al., 2020). Then we identify earthquake sources with the help of paleoseismology and historical, and geological databases of previously active faults. In case of a low seismic activity region, we can describe source as a region where the earthquakes can occur anywhere.

To describe how is a given source capable of producing events with specific magnitude, we typically use the Gutenberg-Richter law (Ward, 1994) given as:

$$log\ \lambda_m = a - bm, \tag{1.1}$$

where λ_m is the rate of earthquakes with magnitude greater than m, and a and b are constants constrained from analysis of historical data. The value a refers to the overall rate of earthquakes in the region, b is a ratio between small and large magnitudes. There are also seismicity models with different magnitude-frequency distribution, e.g.

characteristic model (Wesnousky, 1999) but those are usually used for specific faults where additional information about possible earthquakes is known.

In creating the SRM we assumed as mentioned above the temporal stationarity of seismicity. We assume that earthquake behavior is stable across different time periods and therefore our observations are long term representative. This implies that our PSHA models are also meant to be temporarily stationary, and the general forecast of earthquakes is not temporal specific.

The second ingredient requires ground motion models that relate ground motion parameters such as peak ground acceleration (PGA) to distance for an earthquake of a given size. We look further into ground motion models (GMM) in the next chapter.

The uncertainty component is a key benefit of PSHA. Each of the particular models includes its own uncertainty and combining them together is one of the biggest challenges in PSHA with a lot of potential for future research. The main distinction of uncertainty is to aleatory and epistemic. The first describes intrinsic irreducible variability of earthquake process, the latter characterizes variabilities reducible by our further understanding of the earthquake process. Recognition of this distinction has then important implications for understanding PSHA because we need to correctly analyze it for better interpretation of the mean hazard. Another implication of the understanding of this distinction is the possibility of testing the PSHA model (Gerstenberger et al., 2020).

The last step of PSHA is combining all the knowledge based on previously mentioned models into one curve that represent the probability of exceeding different levels of ground motion at the site for a specific period. That can be written as (Reiter L., 1991):

$$E(z) = \sum_i^N \alpha_i \int_{m_0}^{m_u} \int_{r=0}^{r=\infty} f_i(m) f_i(r) P(Z > z|m,r) dr dm, \quad (1.2)$$

where *E(z)* is the expected rate of exceedances of GM level z during the specified time period t, α_i is mean rate of the occurrence of the earthquake between magnitudes m_0 and m_u for the i-th source within the time period t. $f_i(m)$ and $f_i(r)$ are probability densities of magnitude of source i, and source distance between the locations of source i and the site, respectively. $P(Z > z|m,r)$ is the probability that a given earthquake of magnitude m and epicentral distance r will exceed ground motion level z, which can be evaluated from GMM.

Deterministic seismic hazard assessment (DSHA) addresses ground shaking by considering the seismotectonic setup of the area (Krinitzsky, 1995; Romeo and Prestininzi, 2000) and determining one or more events of interest (e.g. 'maximum credible event' (MCE) or event given by PSHA deaggregation) on each identified source in studied area. Each of the events of interest is used to estimate the ground motion either with empirical attenuation relations (Reiter, 1991) or with use of empirical Green's functions (GF) or synthetic GF's with use of some source modeling method (see Chapter 2).

The most problematic part is to determine the event of interest for each possible earthquake source. There are multiple empirical relationships between magnitude and various fault rupture and tectonic parameters such as rupture length or fault area. Since each selected event of interest is treated separately, their influence on ground motion at the studied site can be explored in detail. Nevertheless, this is not a simple task as there are many parameters to consider as the magnitude, source distance, path effects, etc.

To sum this section up, both methods PSHA and DSHA can be used on their own or combined to provide complementary results for better-informed decision making. Both have their own advantages and disadvantages. Nowadays, in the field of SHA, the PSHA is more common and is used for most hazard ground motion models around the world (Gerstenberger et al., 2020). Despite this, the deterministic approach has its own unique value: as a result of such research there should be an effective ranking of the potential of seismic shaking in a given area. Such ranking can provide basis and guidance for building codes evaluation, determining building design to be effective against shaking effects. These results are often given in various maps of uniform requirements for each zone. These requirements are then mandatory to use in seismically active region to prevent disastrous consequences. Both earthquakes studied in this thesis are related to that.

Empirical ground motion models

The accurate estimation of expected ground motion is a major ingredient in DSHA and PSHA. The traditional approach to development of ground motion models (GMM) has been to combine global data from similar tectonic environments and then develop a model. Such a model is appropriately scaled for different magnitude, distance and site conditions as those are primary predictor variables.

This is called ergodic ground motion model, and it gives us a stable global mean of ground motions, applicable anywhere in the world with similar tectonic setting. However, the ergodic assumption introduces a considerable uncertainty which we need to account for in the hazard estimation. Moreover, it does not have to be accurate enough in specific regions as they can have systematically very different source or path conditions. Then some validation against regional records needs to be applied. It is recommended to test the model against seismic records of the given region and adjust it accordingly. This can be, for example, a constant added to the model's median.

The goal of reducing aleatory uncertainty and thanks to the large increase of regional/local datasets due to the great development in covering the locations with seismographs, leads to so called non-ergodic GMMs. Those are location-specific models that include explicitly modeled location-specific effects (e.g., big basin in a part of the region), reducing the aleatory variability for a given region. The site-specific effects are then assumed as an epistemic uncertainty, which can be reduced and better understood by gathering more data.

The goal of the GMM is obtained by fitting recorded trends by assuming an equation which generally has the following form (Al Atik et al., 2010):

$$Y = f(X_{es}, \theta) + \Delta, \tag{1.3}$$

where Y is a natural logarithm of observed ground motion characteristics, $f(X_{es}, \theta)$ is the prescribed GMM functional form with X_{es} being a vector composed of explanatory variables like magnitude, distance, site conditions, and θ is a vector of model parameters; Δ is a residual that describes the remaining ground motion component.

Following Al Atik (2010) further, Δ can be decomposed into two terms: ΔW and ΔB which are usually called within-event (W-E) and between-event (B-E) variability, respectively. Both are considered zero mean, independent and normally distributed random variables with their respective standard deviations τ and ϕ. The B-E residuals represent the average shift of observed ground motions of a given event from the GMM median. The W-E residuals are then shifts of observed ground motion at a given station from the event's median (GMM median + B-E residual). Those residuals are considered uncorrelated, and thus the total standard deviation of GMM σ can be written as:

$$\sigma = \sqrt{\tau^2 + \phi^2} \tag{1.4}$$

Both B-E and W-E residuals can be further decomposed to other terms (Al Atik et al., 2010) considering that the B-E residuals represent changes in stress drop, slip distributions or source depth between different events, the W-E residuals reflect on variations of the directivity, path, and site effects. We need to acknowledge those decompositions as they further reduce the aleatory variability of the GMM which is important for including the GMM to the computation of seismic hazard. As it is shown in Al Atik et al. (2010), the reduction of aleatory variability with the use of non-ergodic models can be significant. This complicates the modeling of GMM because the global median has to be adjusted by epistemic uncertainty of non-ergodic assumption for each site/source combination.

1.2. Strong motion modeling

For detailed evaluation of seismic hazard and seismic risk, seismic engineers need, as an input, broadband seismograms. There are generally two ways how to obtain these. First, we can rely on the datasets of real data, which are growing rapidly in last decades. This can be seen especially in the example of the Türkiye earthquake (Paper 1), where dense network of stations is installed around the fault almost in every direction. But even though a considerable densification of these datasets, there is still scarcity in the records and especially close to the fault. This serves as a motivation for the other way of obtaining the broadband seismograms, the strong motion modeling.

In the strong motion modeling, we can model the earthquake source radiation and wave propagation and thus create synthetic strong motion waveforms that have similar characteristics as the real recordings. For this we need a realistic source model and

include path and site effects. The modeling should also involve some type of validation against the real records from the area. That can be done simply by comparison of waveforms with recordings or more in detail by computing synthetic GMM and compare it against current empirical GMMs as they contain present knowledge of historic ground motion.

There is a variety of strong motion simulation procedures that take different approaches to the characterization of the earthquake source, seismic wave propagation, and site response.

Types of source models

Source models are commonly divided into two categories:

Dynamic models are based on the physics of faulting. They are based on small-scale laboratory experiments to determine and theoretically describe the friction laws. Dynamic source model combines the friction law with the elastodynamic equation to govern the temporal and spatial distribution of stress and displacement on the fault. As a result, we obtain physics-based rupture propagation. Unfortunately, the dynamic models are computationally demanding as they are a nonlinear problem, but there was a great progress recently using supercomputing including GPU acceleration (Premus, 2023) that makes dynamic modeling more feasible.

Kinematic models of the earthquake source describe each point on the fault in terms of the slip rate function describing the rupture propagation. Major shortcoming is the lack of physics of the earthquake source. Nevertheless, they are still very useful for modeling the seismic wavefield, including its various source-related features such as directivity (Haskell, 1964), or for scenario modeling.

We can divide the kinematic source models into four categories: integral, stochastic, composite and hybrid. All methods aim to generate the ω-squared source spectrum that is widely observed.

The integral method is characterized by prescribing the kinematic variables of the fault (Andrews, 1980; Bernard et al., 1996). The wavefield is then calculated by the representation theorem. This approach requires GFs synthetized for a relatively dense grid of points on the fault depending on the maximum considered frequency.

The stochastic method is the simplest method and is most applicable at high frequencies. It requires prescribing a desired envelope of the signal based on the observation of past earthquakes (for example as a white noise; Boore, 1983). Then one generates random signal tapered by this envelope. The main problem is this approach has no physical background.

The composite method uses the subevents, or subsources occurring on the fault. Each of them is characterized by its source time function and its contribution is summed to get the desired seismic moment and spectral shape. This method can be combined with

empirical Green's functions (EGF), where aftershocks instead of synthetic Green's functions are used. More about composite modeling can be found in Frankel (1991), Irikura and Kamae (1994), Gallovič and Burjánek (2007), etc.

The hybrid method combines the above-mentioned methods in different frequency bands to exploit their advantages and suppress their weaknesses. The methods can be joined and related together in various ways. In this thesis, we use the Hybrid Integral-Composite model (HIC) introduced by Gallovič and Brokešová (2007).

Hybrid Integral-Composite model (HIC)

The HIC model utilize the slipping of virtual subsources that are randomly distributed on the fault plane, can overlap and have various sizes, to describe the faulting process. These subsources are used in both frequency bands, at low frequency for an integral type of model and at high frequency for a composite type. Another key assumption is that relation between the subsources' mean slips and number-size distribution follows the k-squared slip distribution (k is the radial wave number) along the fault as we want to keep the usual ω-squared source spectrum. This assumption implies that number-size distribution follows the power law with fractal dimension D = 2 and the mean slip of a subsource is proportional to its dimension (Andrews, 1980).

We assume different contribution of subsources related to the spatial wavelength. On large scales, we utilize the abovementioned integral approach to compose a rupture from subsources propagating over the whole fault at a constant velocity. The generated wavefield is then given by summing contributions from all source points coherently.

On the other hand, we assume a chaotic rupture process at the small scales, therefore, is not describable by simple space-time distribution of slip function. We assume that subsources act as individual point subevents, which are equivalent to randomly distributed point sources. This implies that the final wave-field contribution of all subsources sums incoherently, thus directivity effect disappears at high frequencies.

For computing this type of source model, we need to develop the database of subsources. This includes their: positions, mean slips, corner frequencies and dimensions. Our fault is a rectangle and has dimensions $L \times W$ and we derived the subsources' dimensions. In the original work (Gallovič and Brokešová, 2007), subsources' dimension was rectangle with $l_n = L/n$ and $w_n = W/n$, and the number of subsources at level n was $N(n) = 2n - 1$. We call n as the subsource level and in this work, it is set up from 2 to 8. At each n, the dimensions of the subsources are the same, therefore the mean slip and corner frequency is the same either. The position of the subsources is distributed randomly, apart first few levels that respect the slip distributions given by inversions or scenario properties.

For large aspect ratio $L \gg W$ the rectangle subsources would be too narrow, thus the subsource geometry was modified to squares with $l_n = W/n$ and $w_n = W/n$. To keep the

density of the subsources coverage of the fault, the number of subsources changes with modifying factor as:

$$N(n) = (2n - 1)\frac{L}{W} \tag{1.5}$$

Now we have two separate models, one calculated by the integral approach up to a frequency f_2. The composite approach is used for frequencies larger than f_1. Assuming that $f_1 < f_2$, those two models overlap in part of their frequency ranges. A smooth transition in this band is utilized between two models in order to properly navigate between two styles of faulting. For this transition, we apply weighted averaging utilizing $sin^2(x)$ and $\cos^2(x)$, where $x = (\pi/2)((f - f_1)/(f_2 - f_1)\,(f_2 - f_1))$.

Determination or choice of f_1 and f_2 is a key factor in computation as it can have a gross effect on the results. It also determinates how dense the discretization of the fault needs to be and therefore the computational power. The width of the band also determines how chaotic or coherent the faulting would be, which has its critical role as it is shown further in this work.

1.3. Content of this thesis

This thesis utilizes kinematic source modeling using hybrid integral-composite approach to model earthquake waveforms in a broadband frequency range and use this for strong motion modeling for a given area of interest. Both earthquakes presented in this thesis (2023 Mw7.8 Kahramanmaraş, Türkiye, and 2016 Mw6.2 Amatrice, Italy) are for the showcase examples of this study.

To categorize this study, we mimic deaggregation of PSHA (in the sense of choosing one specific earthquake setting) to use a deterministic approach to assess the seismic hazard of a specific earthquake in Central Italy and Eastern Türkiye. We expand the view of the controlling earthquake by using different scenarios of its rupture evolution. For this study we firstly validate our forward model (Papers 1&2) by comparing synthetics with real recordings for each earthquake and then we utilize the code to generate possible scenarios of a given earthquake with the same magnitude (Paper 3).

The Kahramanmaraş earthquake (Paper 1) demonstrates how quickly we were able to use kinematic models to estimate hazards relatively well. We reported that even a rough estimation of source parameters and a relatively simple velocity model can lead to satisfying results in ground motion modeling. For simplicity we adopted a planar 300 km fault geometry, with a simple kink in the middle, as suggested by quick reports after the event. We used first estimates of magnitude and utilized ISOLA (multiple point-source inversion) and GNSS data (kinematic slip inversion from static data) to get some knowledge of the slip distribution that could be used in our strong motion modeling.

Firstly, we looked for a suitable broadband rupture model scenario. For a set of 101 stations, we modeled ground motions at each one of them and compared complete waveforms with recordings. This comparison led to the adjustment of the rupture velocity as we can directly see a shift in directivity pulses at different branches of the fault. We also compared parameters such as spectral acceleration, which is a peak measure of motion of damped linear oscillator representing a building with a given resonance frequency. We computed this value across multiple frequencies up to 10 Hz and compared them with real records for each component and station. Following Graves and Pitarka (2010) we then compared the mean values of stations and their components for each scenario.

This comparison led to selection of a plausible source model, which we used to simulate ground motions at a grid of virtual stations, obtaining a rough estimate of the ground motions in the studied area, including the sites close to the source. Generally, ground motions at sites close to the fault system are very demanded by engineers as this area is very hard to predict and earthquakes usually cause the biggest damage here.

In Paper 1 we show how the near-fault zone is affected by the different slip distributions even though the far-field ground motions keep relatively similar properties. This points to some unpredictability in the close vicinity of the fault, or a need for a statistical approach as we do not know how the slip develops during the earthquake

beforehand. However, the far-field areas are relatively intact by slip distribution on the fault if we assume the same rupture speed, direction, and dimensions (see further Paper 1), which can be used by engineers and hazard seismologists to better evaluate risks connected to earthquake ground motions.

We use the **Amatrice earthquake** for further validation (Paper 2) of our method. We utilize the HIC model using parameters following the dynamic inversion by Gallovič et al. (2019) and two dominant velocity models in the area. From there we carry out grid-search for optimal source model parameters, similarly to Paper 1, by minimizing the spectral acceleration bias between the modeled and recorded data up to 10 Hz. For this comparison we select recordings from a set of referential rock stations based on site characterization by Lanzano et al. (2022) to minimize the effect of significant site effects.

After finding the optimal model, we expand beyond the simulation of the real data and add 400 virtual stations to the area to test the robustness of the model by comparing spectral accelerations obtained from synthetic records with the empirical non-ergodic ground motion model SEA21 (Sgobba et al. 2021) in Central Italy for rock sites. The results are showing good agreement with the GMM SEA21 in both median and variability. We believe that this validation is an important step before using synthetic models to generate scenarios of the demanded earthquake.

In Paper 3 we expand the Amatrice case study and perform fully synthetic scenario modeling of an earthquake of magnitude 6.2 on the Amatrice fault. This simulates the situation after a PSHA deaggregation, when we can learn that some earthquakes are more relevant to the final hazard assessment than others. The scenarios were produced by assuming different fault sizes, asperities, rupture velocities, nucleation points and high-frequency radiation parameter a (for further details see Paper 3). All waveforms were calculated up to 10 Hz using two main velocity models in the area.

After generating the scenarios, we studied B-E and W-E variability (among other parameters) in our dataset. We found that the B-E variability exceeds the empirical value provided by the local non-ergodic GMM. Therefore, we considered the non-ergodic GMM as a natural constraint to our synthetic models as it contains the shaking history of the area and deep understanding of the important ground motion effects. We analyze the role of source parameters and restrict the dataset to keep the B-E variability within the empirical value of the GMM. We also demonstrate the pivotal role of the stress parameter for the dataset restriction.

In the last chapter of this thesis, we present summary of conclusions and future outlook for a field of a fast strong motion modeling as the SHA is a field with a possible large impact on safety of society.

2. Broadband strong ground motion modeling of the 2023 Mw7.8 Kahramanmaraş, Türkiye, earthquake including long-period directivity pulses

This chapter was published as Čejka et al. (2023) in Communications Earth & Environment Collection "The 2023 Kahramanmaraş Earthquake Sequence". We made only small notational and stylistic edits.

2.1. Abstract

Damages due to large earthquakes are influenced by broadband source effects that remain enigmatic. Here we develop a broadband (0-10 Hz) source model of the disastrous 2023 Mw7.8 Kahramanmaraş, Türkiye, earthquake by modeling recordings of 100 stations. The model combines coherent and incoherent rupture propagation at low and high frequencies, respectively. We adopt a planar 300 km long kinked fault geometry from geology and pre-constrain the slip model from seismic and geodetic data. We demonstrate that the southwestward rupture propagation was delayed by ~15 s and that the observed strong waveform pulses can be explained by the directivity effect due to a specific combination of the coherent and incoherent components. We show that even a rough estimate of major rupture parameters makes the ground motion simulations of such large events possible, and may thus improve the efficiency of rapid, physics-based, shaking estimation for emergency response and seismic hazard assessment.

2.2. Introduction

At 01:17 UTC (04:17 Türkiye Time) on February 6, 2023, the broader Türkiye-Syria border region was hit by a destructive Mw7.8 earthquake. It occurred on the East Anatolia Fault (EAF) zone, see Fig. 2.1. The EAF is a major left-lateral strike-slip contact between the Anatolian microplate and the Arabian plate (Duman and Emre, 2013; Karabulut et al., 2023). This significant tectonic structure is represented in the Türkiye Seismic Hazard Map (by Disaster and Emergency Management Authority, AFAD). Nevertheless, the human and material losses were enormous, mainly due to collapses of constructions nonconforming with the building code (Hall, 2023; Dal Zilio and Ampuero, 2023; Gürer et al., 2023; Lekkas et al., 2023; Hancılar et al., 2023; Cetin and Ilgaç, 2023). The event belongs to the largest continental earthquakes experienced in the last ~100 years worldwide, including the 2001 Mw7.8 Kunlun, China, and the 2002 Mw7.9 Denali, Alaska, events. As common for such large shallow earthquakes, the Kahramanmaraş rupture produced meters-long surface displacements along the activated parts of the EAF zone (Karabacak et al., 2023; Lekkas et al., 2023; Cetin and Ilgaç, 2023).

Early geodetic and seismic data investigations agree on a 300 km long rupture, featuring a large change of the fault strike near longitude 37°E (further referred to as a kink between the major SW and NE fault segments). The epicenter was situated approximately 30 km east of EAF; the earthquake initiated on the Narlı (also Nurdagi Pazarcik) splay fault, oriented NNE, located near the EAF kink, and then the rupture was transferred to EAF, where it propagated bilaterally (Goldberg et al., 2023; Mai et al., 2023; Zahradník et al., 2023; Petersen et al. 2023; Melgar et al., 2023; Okuwaki et al., 2023). The earthquake reactivated segments that ruptured in 1513, 1872, and 1893 (see Taymaz et al., 2021). In the NE segment, the earthquake terminated before reaching the Pütürge

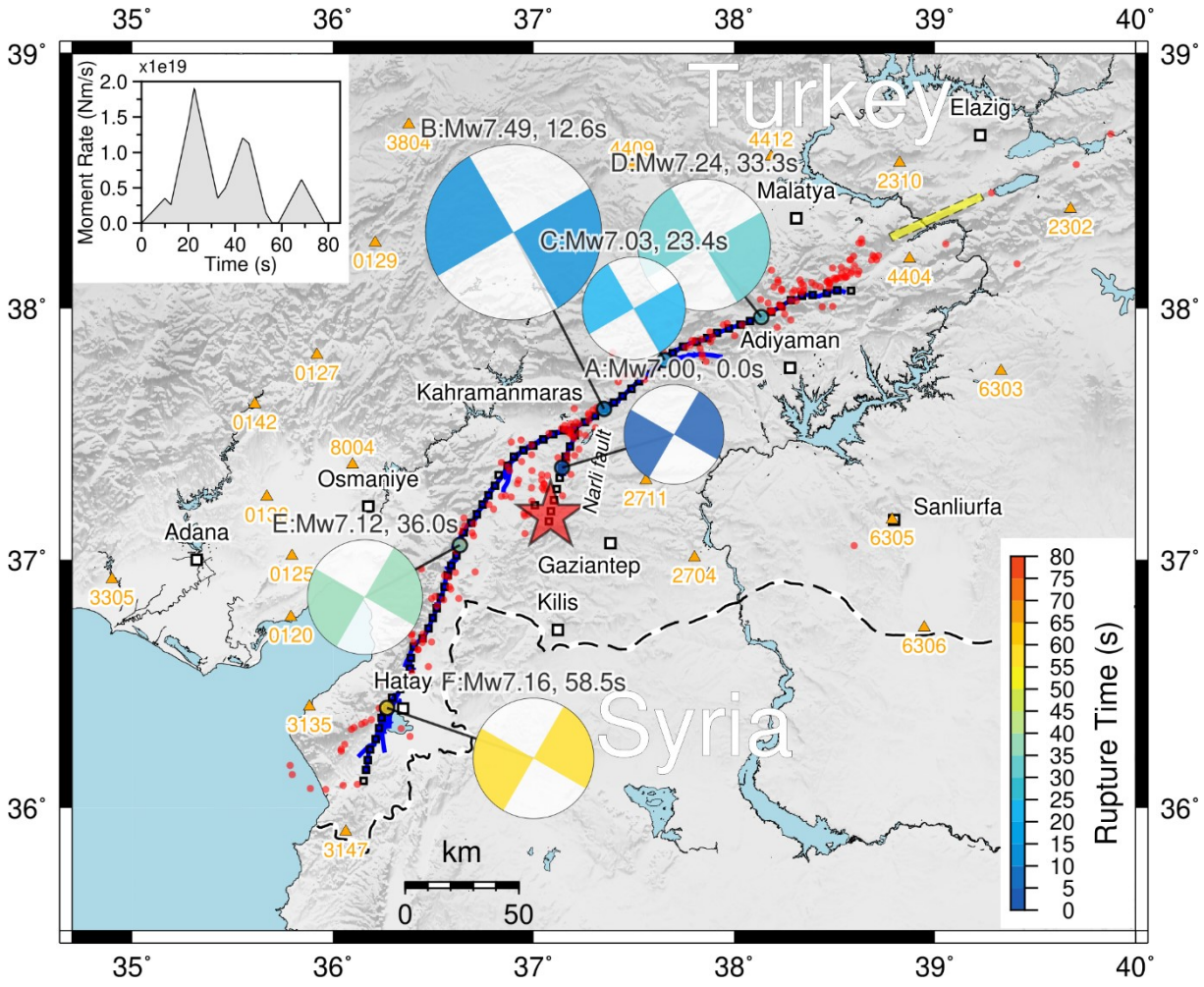

Figure 2.1: Multi-point seismic model of the 2023 Mw7.8 Kahramanmaraş, Türkiye earthquake. Space-time moment release is shown by beachballs with radii scaled assuming constant stress drop (i.e., seismic moment to power 1/3) and colored by rupture time relative to the origin time (see the color scale). Focal mechanisms were fixed differently for the SW and NE segments. The major episodes (marked A-F) are detailed in Tab. S1. Star and triangles depict the epicenter and used stations, respectively. The grid of trial sources is shown with small black squares along the faults (blue lines) mapped by Reitman et al. (2023). Aftershocks located by AFAD are shown as red dots (https://deprem.afad.gov.tr/event-catalog). Yellow rectangle depicts the 2020 Mw6.8 Elazığ earthquake rupture from the dynamic inversion of Gallovič et al. (2020). For a stability assessment of this model, see Figs. S2-S4. Inset is the moment-rate function of this 6-subevent model.

segment of EAF, which hosted the 2020 Mw6.8 Elazığ earthquake (e.g., Taymaz et al., 2021). For the Elazığ earthquake, the dynamic source inversion of Gallovič et al. (2020) revealed a cascading activation of several rupture segments, possibly expected also in the 2023 Kahramanmaraş event. Indeed, Melgar et al. (2023) inverted 12 three-component GNSS and 8 three-component strong motion recordings of the 2023 earthquake for rupture propagation on curved faults, revealing variable rupture speed and strongly inhomogeneous slip distribution. Basic characteristics of the slip heterogeneity agree with the InSAR and teleseismic data inversion by Mai et al. (2023). Rosakis et al. (2023), Abdelmeguid et al. (2023), and Wang et al. (2023) resolved supershear stages within the rupture. Moreover, dynamic models by Abdelmeguid et al. (2023), Jia et al. (2023), and Wang et al. (2023) revealed a ~10-s delay of the rupture, back-propagating towards SW

from the EAF fault kink. In particular, their dynamic modeling suggests that the initial NE propagation along EAF is necessary (but not sufficient) to trigger delayed nucleation of the SE propagating rupture. The delay of the back-propagating rupture is also indicated in the teleseismic back projections of Okuwaki et al. (2023).

So far, all the 2023 Kahramanmaraş earthquake modeling studies have been limited to low-frequency (<1 Hz) seismic data at subsets of available near-fault stations. The recorded peak ground motions generally exceed expectations from empirical models (Mai et al., 2023). Moreover, the observed broadband near-field data feature strong, band-limited long-period pulses, significantly amplifying the velocity waveforms (Wu et al., 2023). These pulse-like motions can cause significant irreversible structural deformation increasing the collapse risk to high-rise buildings and large-span bridges (Hall et al., 1995; Champion et al., 2012). Correct modeling of these pulses is not yet fully established, requiring a careful balance between smooth (coherent) and variable (incoherent) rupture propagation at low and high frequencies, respectively.

Here we utilize the complete set of recordings from 100 strong motion instruments within a 150 km fault distance. The data density ranks the earthquake among the best-recorded worldwide. We first determine stable features from fast static slip inversion of GNSS data and multiple point-source inversion of a subset of low-frequency waveforms to constrain large-scale characteristics of the source model. We then supplement the large-scale model with stochastic high-frequency features to simulate the earthquake in a broad frequency range (0.05-10 Hz) and identify rupture processes that most significantly affect the strong ground motions. The model is validated against observed ground motions in time and spectral domains. Ground motions at a dense set of virtual receivers are calculated to complement the observations by modeling. We also illustrate the sensitivity of the model to individual source features in the Methods section. Finally, we discuss the importance of prior knowledge of the individual source parameters in the ground-motions estimation for rapid emergency response and seismic hazard assessment.

2.3. Results

Low-frequency waveforms: Multiple point-source inversion

We select data from 21 strong-motion stations having good azimuthal coverage, being free of instrumental disturbances, and featuring no obvious timing errors (for details, see Zahradník et al., 2023). We search for multiple point-source (MPS) subevents with the ISOLA software (Zahradnik and Sokos, 2018) using a grid of trial source points designed along mapped fault ruptures (Reitman et al., 2023). The MPS model parameters are centroid positions, times, moments, and possibly also focal mechanisms of major subevents, subsequently retrieved from observed waveforms by iterative deconvolution (Kikuchi and Kanamori, 1991); see Methods.

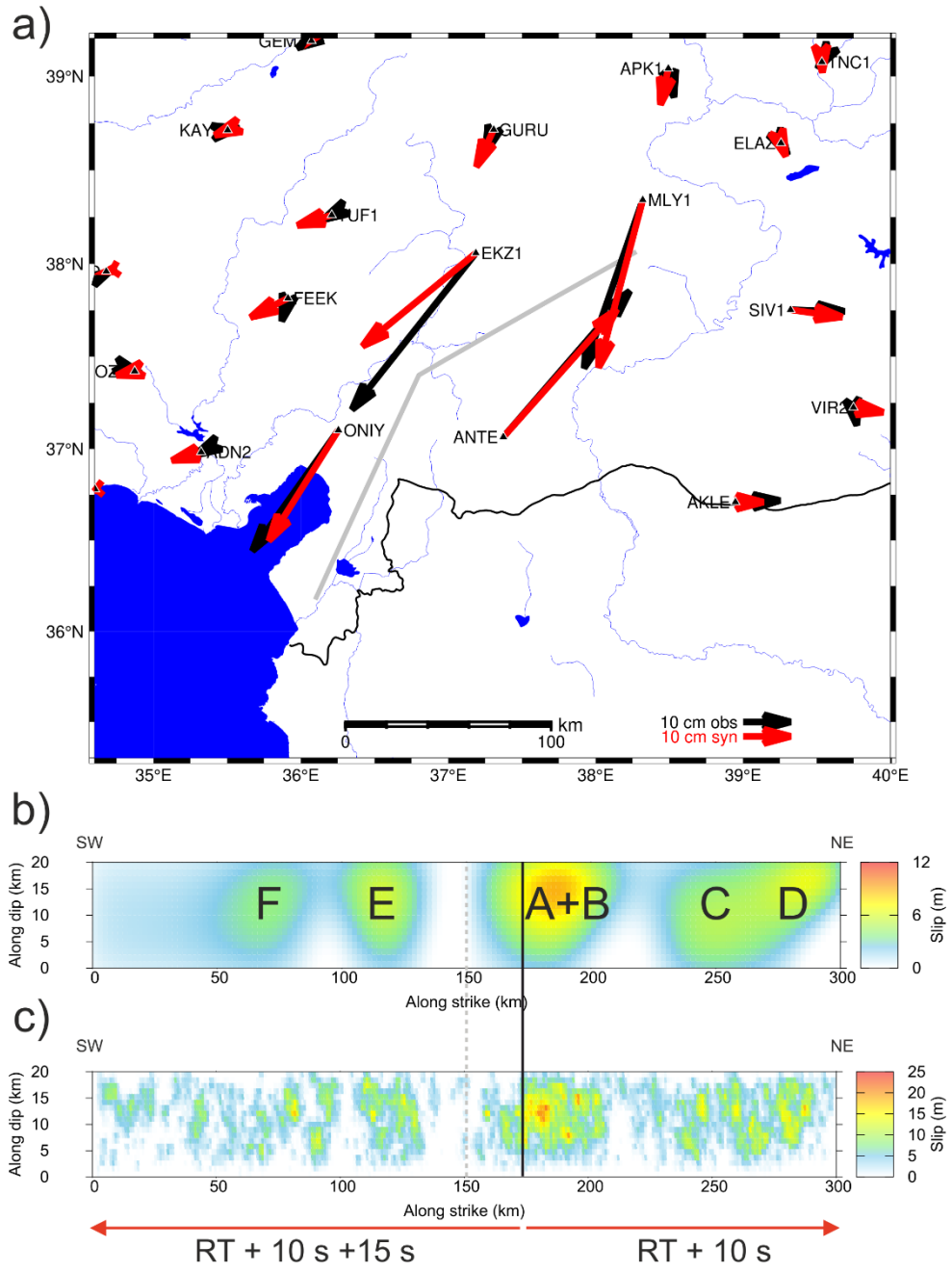

Figure 2.2: a) Fit of GNSS horizontal displacements from the slip inversion of the 2023 Mw7.8 Kahramanmaraş, Türkiye earthquake. Gray line shows the trace of the assumed vertical fault. b) Preferred slip model from the GNSS inversion. The approximate assignment to the MPS subsources of Fig. 2.1 is labeled A-F. Vertical solid line denotes the intersection with the splay fault (excluded from our modeling). Dashed line marks the fault kink (see panel a). c) Slip distribution obtained by summing slip contributions from all subsources in the HIC model. The subsources are placed randomly following the probability density function obtained by normalizing the slip distribution in panel b to unit integral (see Methods for more details). The main features of the rupture kinematics are schematically shown by the red arrows at the bottom (bilateral rupture propagation at constant velocity from the splay fault intersection with depicted rupture delay added to rupture time RT).

The MPS model can quickly reveal the possibly space-time-separated episodes (asperities) of complex segmented earthquakes. Due to the low-parametric character of the MPS model, the inversion is highly flexible, thus enabling fast examination of hundreds of scenarios from which robust solution characteristics can be identified. A disadvantage

is that although the subevent moment is retrieved, slip cannot be estimated until independent information about the subevent spatial size (length, area) is available from further modeling.

Varying trial source positions, frequency ranges, and station subsets produce slightly variable results (see Methods and Figs. S2.1-S2.4). The stable model features across these variations are summarized in the 6-subevent model in Fig. 2.1 and Tab. S2.1: The moment release started on the Narlı splay fault with a relatively weak episode (A) near the origin time. The largest moment release (B) occurred on the NE segment of EAF, spatially entered at ~10 km from the junction of the Narlı fault with EAF, starting 12.6 s after the origin time and being followed by a smaller subevent C (~ 45 km, 23.4 s). The other major episodes (D, E) occurred almost simultaneously in the NE and SW branches (starting 33.3 s and 36.0 s after the origin, centered at ~90 and ~80 km from the junction, respectively). They thus represent a bilateral rupture with a delay towards SW. The rupture terminated after a significant late moment release in SW (F, at ~150 km from the junction, starting at 58.5 s). The position and timing are best resolved for the major episodes B and D (see Methods and jackknife test in Fig. S2.2). The moment-rate function of the 6-subevent model has three major peaks (see inset of Fig. 2.1).

GNSS static displacements: Kinematic slip inversion

For the static slip inversion using the LinSlipInv code (Gallovič et al., 2015), see Methods, we use published GNSS static horizontal coseismic displacements (Fig. 2.2a; Taymaz et al., 2023). Five stations recorded offsets larger than 10 cm in the N or E components. We approximate the fault by a 300 km long planar rupture, with a kink in its middle, i.e., two major planar fault branches. We neglect the initial splay fault rupture. We assume a vertical fault of a 20 km width corresponding to the regional seismogenic width (Ozer et al., 2019).

The inversion is stabilized by spatial smoothing and positivity constraints (see Methods). The optimal smoothing is found by a grid search based on the resulting data misfit and inferred seismic moment. The data fit and slip distribution for the preferred model are shown in Figs. 2.2a and 2.2b, respectively. As discussed in Methods, the depth resolution of the GNSS inversion is poor (due to the vertical fault geometry and surface measurements), while the lateral resolution is ~50 km. Nevertheless, the slip model suggests a patch-like (segmented) moment release, as also indicated by the multiple point-source MPS model explained above.

Comparing the GNSS and MPS seismic model, we can assign timing to the slip patches in Fig. 2.2; see also Tab. S1: Geodetic patches A+B on the NE segment are linked with the 1st and 2nd MPS episodes starting at 0 and 12s, C and D are related with the 3rd and 4th seismic episodes starting at 23 and 33 s, respectively. Subsources E and F are linked with the 5th and 6th seismic moment release that occurred 36 and 59 s, respectively, on the SW segment.

The models agree in basic characteristics with other published source models. For example, our position of major asperities on the NE segments B and D agrees with Goldberg et al. (2023), Melgar et al. (2023), and Mai et al. (2023). Our patches on the SW segment are an analogy of the Goldberg et al. (2023) model and the geodetic slip inversion result of Mai et al. (2023). Note that the SW segment is the place of the largest difference between the geodetic and teleseismic models of Mai et al. (2023). Our moment-rate function agrees well with Golberg et al. (2023), Melgar et al. (2023), Okuwaki et al. (2023), and Jia et al. (2023) up to ~55 s. This corresponds to the space-time robustness of our subevents B and D. At later times, affected mainly by the SW segment, the time functions differ among studies, our being relatively close to Jia et al. (2023).

Modeling of broadband ground motions

To model strong ground motions in a broad frequency range (0.05-10 Hz), we utilize the kinematic Hybrid Integral-Composite (HIC) approach (Gallovič and Brokešová, 2007); see also Methods for all details. The model represents the rupture process by randomly distributed overlapping rectangular subsources with fractal number-size distribution. The hybrid approach combines coherent wavefield contribution from the rupture propagation over the subsources at low frequencies and incoherent contribution from the subsources treated as point sources at high frequencies. In addition, the point sources are considered to feature random variations of the focal mechanism to weaken the radiation pattern at high frequencies to a realistic level. The wavefields are crossover combined in a frequency range of 0.1-0.4 Hz for stations within 10 km from the fault and 0.05-0.2 Hz elsewhere. The hybrid combination of the two modeling approaches simulates the directivity effect that weakens with increasing frequency (see Methods for tests demonstrating the adequacy of the crossover bands). We assume a constant rupture velocity for simplicity. We utilize synthetic Green's functions in the entire frequency range, considering a 1D regional velocity model by Acarel et al. (2019) with added shallow low-velocity layers to account for high-frequency amplification of a generic rock site; see Methods and Fig. S2.6 for results with the original velocity model of Acarel et al. (2019).

The seismic and GNSS data inversions indicate an uneven ("patchy" or asperity-like) structure of the rupture and a time delay of the subevents on the SW fault branch. We use the same 300 km long, kinked fault geometry in the broadband modeling as in the GNSS inversion. We do not simulate the initial rupture propagation along the Narlı fault to keep the broadband model simple. Instead, we assume that the rupture formally starts at the intersection of EAF with the Narlı fault and shift the synthetics on both the NE and SW segments by 10 s (Fig. 2.2c). No additional station-specific time shifts are applied. We constrain the random spatial distribution of the subsources (independently of their size) by the slip distribution from the GNSS inversion (see Methods). The subsources then concentrate in the asperity areas, as can be seen from Fig. 2.2c, which displays a

realization of the slip distribution obtained by summing contributions of the subsources.

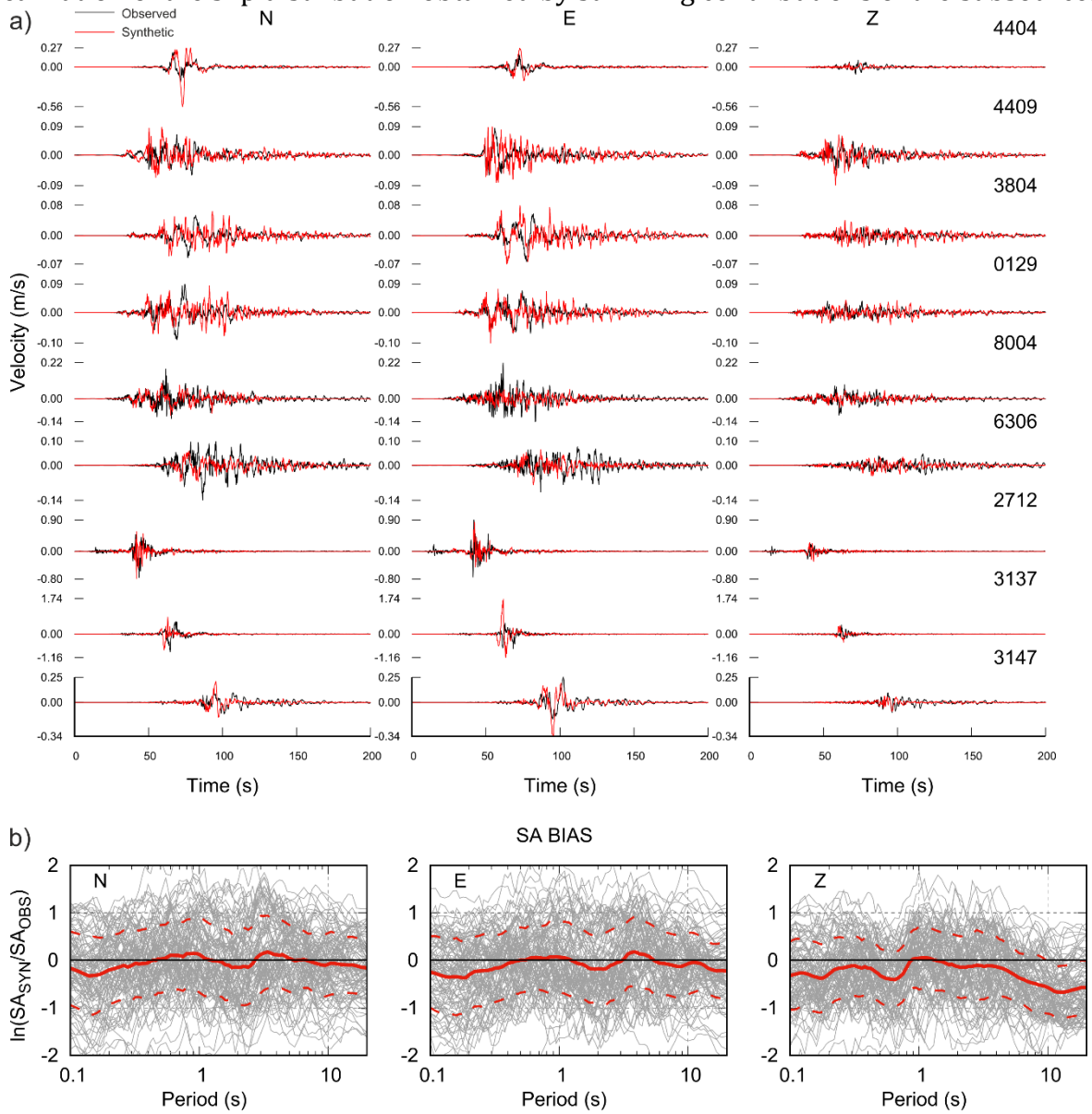

Figure 2.3: Modeling result for the preferred broadband source model. a) Comparison between synthetic (red) and observed (black) three-component velocity waveforms for selected stations from around the fault (see Fig. 2.4a); see Fig. S2.7 for all 100 stations. b) Spectral acceleration (SA) modeling bias (Eq. 1) plotted for individual components as a function of a period (gray lines). Mean and ±1 standard deviation over stations are depicted by red solid and dashed lines, respectively.

The slip distribution is considered in the low-frequency (integral) part of the simulations, while the same subsources are consistently used in the high-frequency (composite) modeling.

Having prescribed the layout of the subsources, we perform trial-and-error calculations to constrain the remaining rupture parameters (rupture velocity v_r, and stress parameter $\Delta\sigma$). In addition, we also search for the delay of the SW segment from the splay fault intersection (see illustration in Fig. 2.2c). We determine plausible values by comparing the synthetics in the time domain and the response spectra with

observations. We quantify the data fit for all 100 available stations using the modeling bias of spectral accelerations (SA) following the standard approach of Pitarka et al. (2021). We evaluate SA residuals $r_j(T_i)$ at each station's component j between synthetics M_j and recordings O_j at period T_i,

$$r_j(T_i) = \ln \frac{M_j(T_i)}{O_j(T_i)}. \quad (2.1)$$

The preferred model has values of v_r = 3.0 km/s, $\Delta\sigma$ = 13 MPa, and a 15-s delay of the SW portion of the rupture propagation (Fig. 2.2c). The Methods section includes sensitivity tests demonstrating the deteriorating effect on the data fit when changing rupture velocity (Test I) and rupture delay (Test II). Changing the slip distribution (Test III) suggests this effect is only important to the near-fault region.

Fig. 2.3a compares velocity synthetics with recordings at a subset of 9 stations from around the fault (Fig. 2.4a) to demonstrate the strong spatial variability of the ground motions (see also Fig. S2.7 for all 100 stations). The synthetics explain the overall maximum amplitudes and durations quite well. The preferred model explains the timing, width, and amplitudes of strong velocity pulses dominating the recordings close to the fault (2712, 3137) and in the strike directions of the fault (stations 4404 and 3147), due to the significant directivity effect (Baltzopoulos et al., 2023). Nevertheless, the sensitivity test in Methods confirms that the directivity effect is band-limited likely due to a decoherence of the rupture propagation at small scales. Note that the slightly later arrival of the main pulse at 3137 suggests local variations in rupture velocity that are not targeted by the modeling.

Fig. 2.3b shows the SA modeling bias r_j (gray curves) and its mean and variability evaluated for each component as the average and standard deviation at each period (red solid and dashed curves, respectively). Fig. 2.3b documents an almost zero mean bias at horizontal components and periods. The bias at the vertical components is slightly negative, especially at longer periods. This underestimation of the observation is likely due to the constant (vertical strike-slip) mechanism considered in the modeling, while real data might be affected by (so far poorly resolved) variations of the rupture geometry, including the potential activation of several splay faults. Overall, the modeling results are satisfactory, considering they were derived under simplifying assumptions, especially regarding the wave propagation effects. Indeed, we use only a 1D velocity model of a generic rock site (see Methods), i.e., we neglect site effects due to specific shallow subsurface layers and do not consider any 3D velocity variations (structures like sedimentary basins). For example, synthetics for coastal lowlands stations 0119 and 0120 located on the western side of the Iskenderun Gulf lack strong later peaks, suggesting particular unmodeled complexity in the wave propagation (see Fig. S2.7).

Besides the real stations, we further calculate synthetics on a uniform grid of 460 virtual receivers surrounding the fault and plot the resulting peak ground velocities (PGV) in Fig. 2.4a. The peak values are rotationally independent mean values (GMRotD50; Boore,

2010). Comparison with the real data (color triangles) suggests an overall good fit. The spatial variability of the observations in places with more seismic stations (e.g., near the SW termination of EAF) suggests localized amplification due to site effects.

To reveal possible distance and azimuthal dependencies, Fig. 2.4b shows a comparison of the observed and synthetic PGV, peak ground displacements (PGD) and accelerations (PGA), all GMRotD50, as a function of station azimuth (measured from the north) and Joyner-Boore fault distance. Both observed and synthetic PGD and PGV (and less clearly PGA) exhibit significant azimuthal dependence with maxima in the fault strike directions (azimuths -155° and 60°). This suggests that the radiated ground motions were strongly directive, and the model captures the observed directivity effect well. We point out that the observed weaker azimuthal dependence of PGA than PGV and PGD is explained in the HIC model by the transition from the coherent to incoherent summation, as we also address in Methods. The synthetics also capture the distance dependence of the ground motion peak values. It all suggests that the wave propagation effects, such as scattering from small-scale random 3D velocity perturbations (likely existing in real medium), do not strongly deteriorate the directivity effect with distance.

2.4. Discussion and Conclusions

We have modeled source process and ground motions due to the disastrous 2023 Mw7.8 Kahramanmaraş, Türkiye, earthquake. In agreement with other published models, the low-frequency seismic and GNSS data inversions indicate an asperity-like structure of the rupture and a significant delay of the rupture propagation southwestward from the intersection of EAF with the initiating Narlı splay fault. The main focus of the present paper is on source modeling extended to broadband frequencies of engineering interest.

To model strong ground motions in a broad frequency range (0.05-10 Hz), we have utilized the kinematic Hybrid Integral-Composite (HIC) approach. By comparison with data in time and spectral domains, we have found plausible values of three main model parameters: stress parameter $\Delta\sigma$ = 13 MPa controlling the strength of the high-frequency radiation, the 15-s time delay of the SW fault segment, and constant rupture velocity v_r = 3.0 km/s (representing a mean over the fault). We point out that we intentionally keep the model relatively simple regarding details of the rupture propagation (e.g., constant rupture velocity) because the HIC technique is considered a strong-motion prediction tool, intended for general applicability expecting only a rough prior knowledge of earthquake scenario details (Ameri et al., 2011). The model explains the peak ground motions (PGD, PGV, PGA) well, including their distance dependence and azimuthal variability controlled by the directivity effect. The synthetics explain durations and overall spectral content in terms of small mean bias of the response spectra over 100 stations. Also explained are strong band-limited directivity pulses due to coherent rupture propagation at large scales, which are significant not only close to

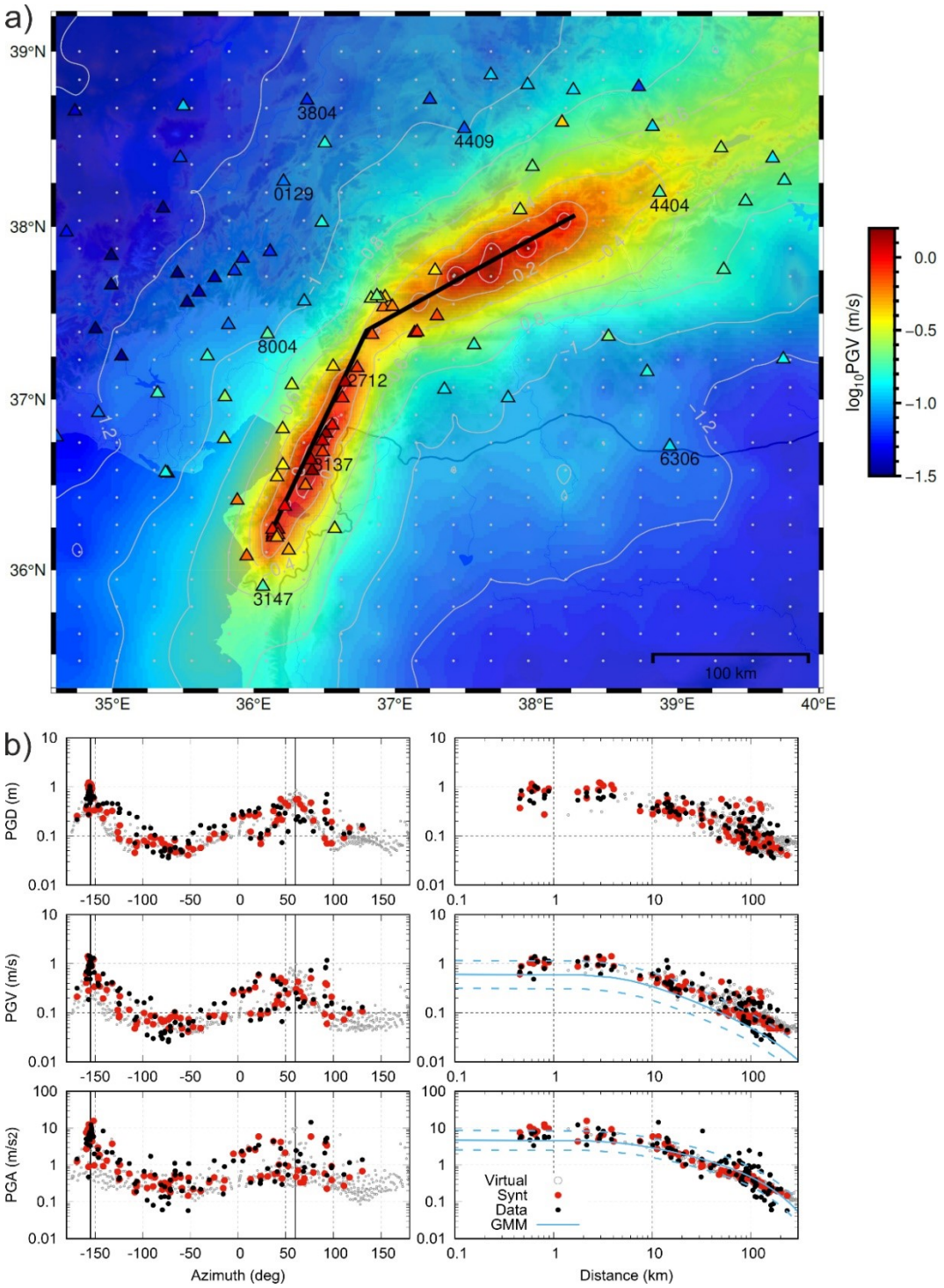

Figure 2.4: Comparison of synthetic and observed peak ground motions, assuming rotationally-independent mean values (GMRotD50; Boore, 2010). a) Modeled horizontal peak ground velocities (PGV) interpolated from synthetics at virtual stations (gray points) for the preferred broadband model. The trace of the assumed vertical fault is shown by the black line. Real stations are indicated by triangles color-coded by observed PGV; station names are shown only for those with waveforms in Fig. 2.3a. b) Peak ground displacements (PGD), velocities (PGV), and accelerations (PGA) from horizontal components as a function of azimuth (left) and distance (right). Black and red dots are observed and synthetic values at the real stations, respectively; gray circles correspond to the virtual stations. Black vertical lines in the left panels indicate the SW and NE azimuths of the fault. The ground motion model (GMM) of PGV and PGA (NGA-West2; Boore et al., 2014) is plotted as a blue line in the distance-dependent plots for reference.

the fault but also at further distances (Fig. 2.2). The comparison with observations points to the limitations of the model. They are mainly related to using an 'average' model of a rock station, which cannot capture local high-frequency amplifications due to shallow velocity reduction, generally denoted as site effects, or broader 3D structures as sedimentary valleys. Future studies can pinpoint such details of individual stations and incorporate them into the modeling.

The HIC approach combines coherent wavefield contribution from the rupture propagation at low frequencies and incoherent contribution from randomly distributed overlapping subsources with fractal number-size distribution at high frequencies. The hybrid combination of the two modeling approaches simulates the directivity effect that weakens with increasing frequency. As we show in comprehensive numerical tests (see Methods), this type of directivity enables properly explaining the observed strength of the directivity velocity pulses and the azimuthal dependence of the peak motions. The latter is stronger for PGD and PGV, while rather weak for PGA (Fig. 2.4a). Moreover, in the PGV and PGD distance plots, the directivity is seen up to ~100 km (Fig. 2.4b). Contrarily, the tests show that despite considering crossover band at slightly higher frequencies for near-fault stations, the coherency of the radiated wavefield must still be limited to low frequency (see Methods and Fig. 2.5). It all suggests that limited high-frequency directivity is a source effect, as also observed for small events by Pacor et al. (2016) and Colavitti et al. (2022). The possible explanation is due to the significant complexity of the short-scale rupture propagation that inhibits the high-frequency directivity effect (Taufiqurrahman et al., 2022; Gallovič and Valentová, 2023).

Another interesting aspect of the simulations is that although our broadband rupture model does not include significant coseismic surface slip found in field observations (Cetin and Ilgaç, 2023; Karabacak et al., 2023), no prominent wavefield components are 'missing' in the frequency range considered, especially at larger distances from the fault. As Kaneko et al. (2008) demonstrated, neglecting shallow velocity strengthening rheology or very large fracture energy, which would reduce coseismic slip close to the surface, leads to very strong surface waves. Since such waves do not appear in the recordings, the fault slip at the surface likely emerged very slowly, possibly as a very early afterslip (such as documented for the Parkfield earthquake; Jiang et al., 2021), not radiating significant seismic waves. Therefore, not accounting for surface rupture does not deteriorate the simulations if one is not interested in the fault displacement hazard.

Sensitivity tests in Methods demonstrate how various specific source parameters (crossover frequency band in Fig. 2.5, rupture velocity in Fig. 2.6a, delay of the SW part of the rupture in Fig. 2.6b, slip distribution in Fig. 2.7) are imprinted in the observed recordings. For example, response spectra, commonly used in seismic codes, are affected by the rupture delay very weakly and by the value of constant rupture velocity rather mildly. Also, a generic slip model unconstrained by the GNSS data provides similar response spectra as the preferred model. The formation of broadband directivity pulses can be captured even with limited knowledge of the rupture velocity once the fault size

and rupture direction are known. The present paper thus not only extends so-far published knowledge of the 2023 fault rupture to engineering frequencies, but also serves as a potential sample workflow for rapid physics-based ground-motion estimations for similar future earthquakes that are so far based on interpolation and empirical ground motion models (ShakeMap, Worden et al., 2018).

In seismic hazard assessment, none of the rupture parameters, such as slip distribution, rupture velocity, and location of the nucleation point, can be anticipated for a future event. Therefore, they must be treated as epistemic uncertainty through scenario simulations in physics-based seismic hazard assessment. Our results emphasize the strong ground motion variability due to the source effects, which must be included in such applications. Despite many efforts to have these effects in empirical approaches in a simplified manner (e.g., Spudich et al., 2014; Spagnuolo et al., 2016), the physics-based modeling implicitly accounts for them, including their frequency dependence.

2.5. Methods

Multiple point-source inversion of seismic data

We use the ISOLA software, which inverts complete seismograms for a multi-point source (MPS) model. ISOLA has been continuously upgraded and applied to reveal earthquake complexities (Sokos and Zahradnik, 2013; Sokos et al., 2016; Zahradnik and Sokos, 2018; Liu et al., 2018; Liu and Zahradnik, 2020; Hicks et al., 2020; Turhan et al., 2023). Besides low-parametric character, another advantage is that MPS solutions are robust to errors in earthquake location and source-geometry specification. It is because subevents are space-time grid-searched in an almost arbitrary set of trial source positions and rupture times. The rupture process is not a priori constrained to start at the hypocenter or to continually proceed along a planar fault segment within prescribed rupture-speed limits.

Even the low-parametric MPS inversions are vulnerable to parameter tradeoffs. Therefore, for example, Duputel and Rivera (2017) preferred to fix the spatial positions of the subevents. Analogously, other constraints were discussed by Yue and Lay (2020). Tradeoffs between space-time moment variations and non-double-couple (non-DC) moment tensors might be particularly dangerous. The latter typically accompanies multi-type faulting subevents whose correct structure can only be revealed if seeking 100% DC-constrained subevents (Sokos et al., 2020), or prescribing a given focal mechanism.

Several frequency ranges were examined for the 2023 event. Finally, we adopt the minimum inverted frequency of 0.01 Hz to avoid instrumental noise. To avoid errors due to possible inadequacy of the velocity model, we choose the maximum frequency of 0.05 Hz. The same 4th-order causal Butterworth bandpass filter 0.01-0.05 Hz is applied to the real instrumentally corrected seismograms and synthetics, and both are integrated into displacements. We use synthetic full-wavefield Green's functions in the velocity model of Acarel et al. (2019); see section Crustal velocity model. Moment-rate of each subevent is a triangular function of 20-s duration. The fit between real and synthetic

bandpass filtered displacement waveforms is quantified with variance reduction, VR = 1-|obs-syn|^2/|obs|^2, where |.| is the L2 norm. The temporal grid search starts at the origin time and ends after 70 seconds. For the preferred mode, the focal mechanism is constrained as follows: strike/dip/rake = 30°/90°/0° on the SW segment of EAF and the Narlı splay fault, and 60°/90°/0° on the NE segment. The model has variance reduction VR = 0.70, and the waveform fit of the 21 strong-motion records is shown in Fig. S2.1.

The stability of the solution is checked by station jackknifing (repeating inversions, each time removing one station); see Fig. S2.2. As the MPS depth resolution was poor, we report stable results at a constant depth of 7.5 km in the Results section. The largest moment release episodes (B and D) on the NE segment of EAF are also the most stable. The least stable is the weak moment release on the Narlı fault. The lower resolution of the SW (F) subsource can be attributed to the limited southwestward coverage of suitable stations (i.e., located further from the fault). The total seismic moment of this model is 4.0 x 10^{20} Nm; i.e., moment magnitude Mw7.7 is underestimated by ~0.1 due to the absence of frequencies below 0.01 Hz.

Even better data fit (VR = 0.77) can be achieved if allowing space variation of the DC-constrained focal mechanism; see Fig. S2.3. It is analogical to allowing varying rake angle in published slip inversions; e.g., Goldberg et al. (2023) found an oblique-slip component on EAF near the splay. Normal/reverse faulting components have been geodetically proposed to supplement major strike-slip faulting on EAF (Özkan et al., 2023). Non-uniform aftershock mechanisms (Petersen et al., 2023) indicate that even the mainshock might have included short segments that differ from strike-slip, similar to fault complexity which was indeed identified on the western termination of the second February 6 Mw7.5 mainshock (Okuwaki et al., 2023; Zahradník et al., 2023). Fig. S2.3 demonstrates that MPS with a free DC mechanism confirms the strike-slip faulting on the NE segment, with strike ~60° agreeing with fault geometry. However, a possible focal mechanism variation on the SW segment is less clear. As inferred by low solution stability in the jackknife test (Fig. S2.4), we cannot strictly define any stable departure from strike-faulting during mainshock there. Free DC mechanism could also mislocate weak NS episodes around 25 s onto the Narlı fault. Thus, in the preferred model, we use two fixed focal mechanisms.

A preliminary MPS model of 2023 Türkiye mainshocks was released 14 days after the earthquake as an EMSC report, see Data and Resources. We make this note to emphasize the usefulness of the simple MPS method, implying that after data acquisition and quality check, extensive source-inversion testing can be performed shortly after a similar disastrous event. Similarly, the GNSS inversion can be applied quickly once the data and fault geometry are retrieved.

Kinematic slip inversion of GNSS data

We use linear slip inversion of coseismic GNSS displacements to image the slip distribution using open-source code LinSlipInv (Gallovič et al., 2015). We assume a planar fault with a kink. Synthetic displacements are calculated according to Okada (1992). The

inversion is stabilized by the positivity constraint (Lawson and Hanson, 1974) and by prescribing an isotropic correlation function of model parameters with k^{-2} amplitude spectrum (where k is the radial wavenumber), which smooths the slip distribution. The smoothing strength is controlled by a non-dimensional ratio between the standard deviations of the model parameters and data (further called the relative smoothing weight). The optimal smoothing is found by a grid search based on the resulting data misfit and inferred seismic moment.

We test the strength of the smoothing through varying relative smoothing weight s_w in a sufficiently wide range to observe the sensitivity of the inversion. Fig. S2.5 demonstrates that the GNSS data are almost equally well-fitted for any $s_w \leq 2$. Moment decreases below 4.5×10^{20} Nm for $s_w < 0.8$ and $s_w > 8.0$. The moment peaks for $s_w = 2$ at $M_0 = 4.8 \times 10^{20}$ Nm with VR = 0.61, see Fig. 2.2. For examples of stronger and weaker smoothing models, see Fig. S2.5. We note that the data fit at the EKZ1 station can be improved by allowing a spatially varying strike and dip with only a minor effect on the slip distribution (Zahradník et al., 2023). Nevertheless, here we prefer a simpler and more robust model of Fig. 2.2.

The dependence of the inverted slip models on the smoothing strength allows for a rough estimate of the inversion resolution. Indeed, the weaker the smoothing is, the more concentrated the slip patches are (Fig. S2.2). The minimum patch size for the preferred smoothing level suggests a lateral resolution of about ~50 km. The depth resolution is lower than the width of the fault due to the vertical geometry and the use of surface stations.

Broadband Hybrid Integral-Composite source model

For the broadband ground motion simulations, we use the Hybrid Integral-Composite (HIC) technique by Gallovič and Brokešová (2007), which was previously applied to modeling of, e.g., the 2009 Mw6.2 L'Aquila (Central Italy; Ameri et al., 2012) or the 2011 Mw7.1 Van (Eastern Turkey; Gallovič et al., 2013) earthquakes. It represents the rupture process by overlapping rectangular subsources with random slip distribution having k^{-2} decay at high wavenumbers k. The subsources are randomly distributed on the fault with fractal number-size distribution; the number of subsources increases linearly with decreasing subsource size. The subsources are characterized by a constant stress-drop scaling, composing a slip distribution on the whole fault with k^{-2} decay. We constrain the random spatial distribution of the subsources (independently of their size) by prescribing a probability density function (PDF) over the fault. It is considered equal to the slip distribution from the GNSS inversion (Fig. 2.2b) plus a water level of 10% of the slip maximum; further, the PDF is normalized to a unit integral. Thus, the subsources tend to localize in the asperity areas, but not exclusively there due to the water level (compare Fig. 2.2c and 2.7a for the constrained and unconstrained case).

The subsources are treated differently in the low- and high-frequency ranges. As described below, the two procedures result in seismograms, which are then combined in a crossover frequency interval (f_1, f_2) by weighted averaging of the real and imaginary

parts of their Fourier spectra using $\cos^2$ and $\sin^2$ functions. The two approaches are as follows (see Gallovič and Brokešová, 2007, for more details).

Up to frequency f_2, the integral of the representation theorem (Aki and Richards, 2002) is evaluated: The fault is discretized into a regular grid of subfaults. At each subfault, the slip is computed as a sum of contributions from all subsources covering the subfault. The rupture time is calculated from the distance of the subfault to the nucleation point of the earthquake and the prescribed (constant) rupture velocity v_r. The slip velocity function has Brune's pulse shape with a constant rise time of 0.1s. We note that it is shorter than the reciprocal of f_2 and thus does not affect the synthetics. Green's functions (GFs) are calculated from the center of each subfault, and the synthetics are obtained by convolving slip rates with the GFs and integrating over the fault. In this approach, the directivity of the rupture propagation is well captured at low frequencies due to the coherent summation of the subfaults' wavefield contributions.

Above f_1, the composite approach is used: The individual subsources are treated as point sources with Brune's source time function, described by their respective seismic moments and corner frequencies (assuming a constant stress drop scaling). Synthetics for a given subsource are obtained by convolution of the source time functions (Brune pulse) with GFs calculated from the subsource's center. These contributions are then shifted by their respective rupture time, calculated as the time that the rupture needs to reach the center of the subsource, considering the same rupture velocity v_r as in the integral approach, and summed. In contrast to the integral part, the directivity effect is suppressed due to the incoherent summation of the subsources' wavefield contributions. We add random variations in strike, dip, and rake to the mechanisms of the subsources to weaken the effect of the radiation pattern at high frequencies, in agreement with empirical studies (e.g., Kotha et al., 2019; Trugman et al., 2021)

The seismic moments of the subsources m_{0i} are constrained so that their sum gives the earthquake's total scalar seismic moment M_0. In the composite approach, the subevents' corner frequencies are adjusted so that the resulting high-frequency acceleration plateau of the event has a prescribed height. For the Brune omega-square source time function, the height of the acceleration spectral plateau is equal to $A = M_0 f_c^2$ with f_c being the event corner frequency, respectively. We assume that f_c is related to the stress drop of a crack model (e.g., Brune, 1970; Kaneko and Shearer, 2015; Wang and Day, 2017; Gallovič and Valentová, 2020),

$$\Delta\sigma = \frac{7}{16}\left(\frac{f_c}{k v_s}\right)^3 M_0, \tag{2.2}$$

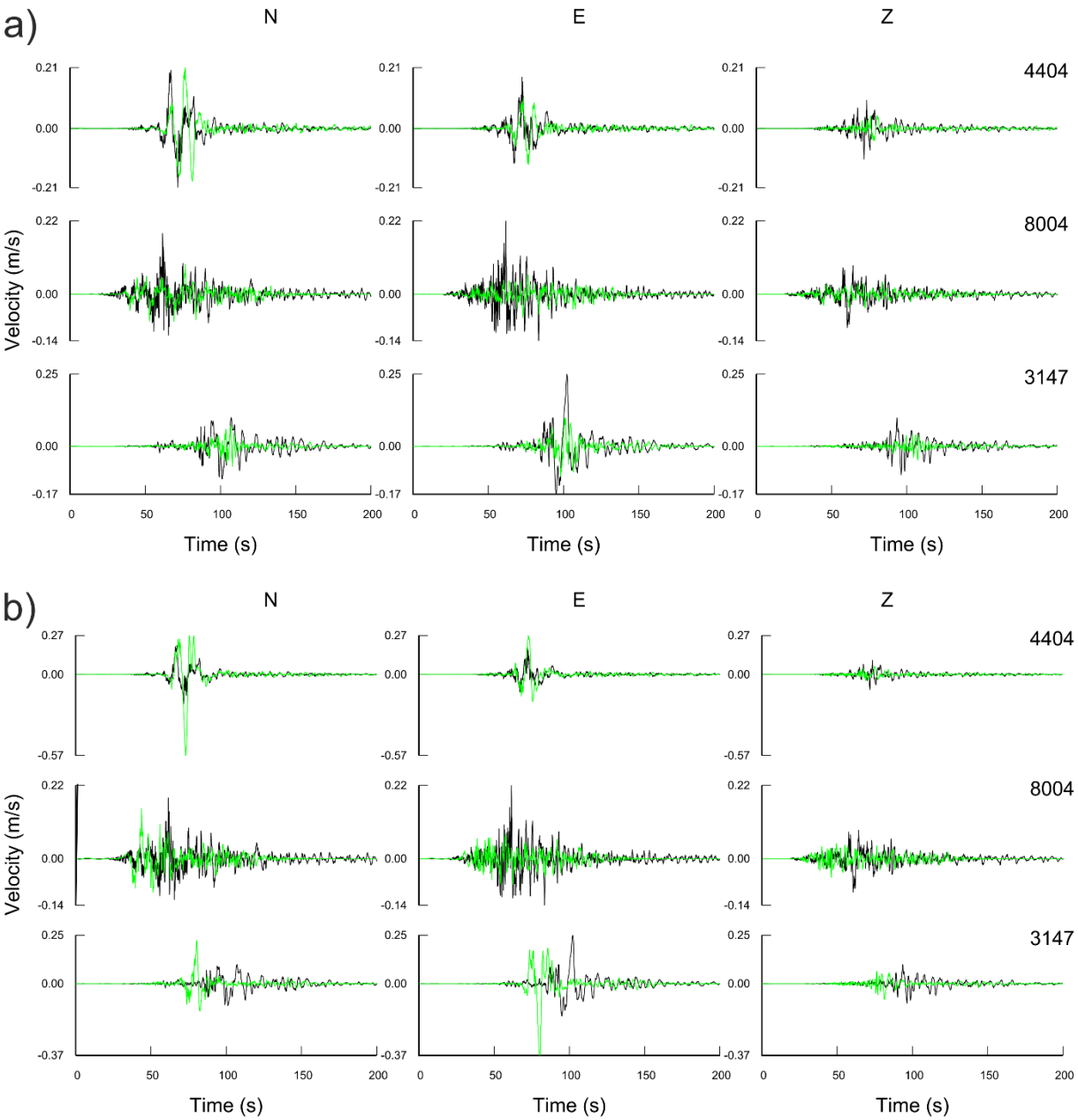

Figure 2.5: Effect of the coherent (low-frequency) rupture propagation modeling on the broadband ground motion simulations. a) Left: Broadband synthetic (green) and observed (black) velocity waveforms for the crossover at higher frequencies (0.25-1.0 Hz) than applied in the preferred model. Right: Spectral acceleration (SA) modeling bias for horizontal components as a function of period (gray lines). Mean and ±1 standard deviation over stations are shown by green solid and dashed lines, respectively. The red line is the mean SA bias for the preferred model (Fig. 2.3b) for reference. The test shows the overestimation of the directivity effect due to assuming coherent rupture propagation up to too high frequencies. b) Same denotation as in panel a, but for omitted coherent part of the simulation, i.e., for a purely incoherent composite model. It demonstrates an underestimation of the directivity effect when the coherent rupture propagation at large scales are omitted.

where v_s is the shear-wave velocity, and k is a parameter depending on the details of the rupture model (e.g., heterogeneity of slip and rupture velocity). Since $\Delta\sigma$ is treated rather formally in the HIC model, we refer to it as the stress parameter and consider $k = 0.37$ (Brune, 1970). We consider the corner frequency of the subsources as $\hat{f}_{ci} = \frac{av_r}{l_i}$, where l_i is the subsource length, and a is an unknown parameter. Assuming incoherent summation

of the subsources' contributions at high frequencies, the total height of the earthquake spectral plateau squared is,

$$A^2 = \sum_i m_{0i}^2 \widehat{f_{ci}^4}. \quad (2.3)$$

For prescribed M_0 and $\Delta\sigma$, parameter a can then be determined from Eqs. (2.2) and (2.3).

To summarize, the HIC model parameters for fixed M_0, fault area, and nucleation point are: i) the layout of subsources (and thus the resulting slip distribution), ii) rupture velocity v_r, and iii) stress parameter $\Delta\sigma$. We point out that it is straightforward to introduce specific time delays in the rupture propagation, as needed here, by increasing the rupture times of the subfaults and subsources. The parameters are constrained based on preliminary geodetic and low-frequency seismic data inversions and by trial-and-error comparisons of the broadband simulations with the recordings in both time and frequency domains.

Following Ameri et al. (2012), we assume two crossover frequency ranges depending on the station distance from the rupture. While we consider 0.1-0.4 Hz for stations within 10 km from the fault, we use 0.05-0.2 Hz elsewhere. We perform two tests to demonstrate the adequacy of the considered crossover frequency ranges and facilitate discussion regarding their significance. Firstly, we test the crossover at higher frequencies (0.25-1.0 Hz), i.e., applying the coherent integral technique to higher frequencies. Fig. 2.5a shows the corresponding velocity waveforms for the selected stations and the SA bias for all stations, including its mean and variability. The SA bias shows systematic overestimation in the 2-10 s period range. The waveform comparison then demonstrates that it is due to unrealistically strong directivity amplification in the integral (coherent) part of the synthetics. Secondly, assuming only the composite model (i.e., omitting the integral approach in the low-frequency band) leads to significant underestimation at periods larger than ~5 s, see Fig. 2.5b. This is due to the incoherent summation of the wavefield contributions of the subsources that reduce the directivity effect, contradicting the observations. Indeed, this is expressed by the inhibited velocity pulses in the synthetics at all selected stations shown in Fig. 2.5b.

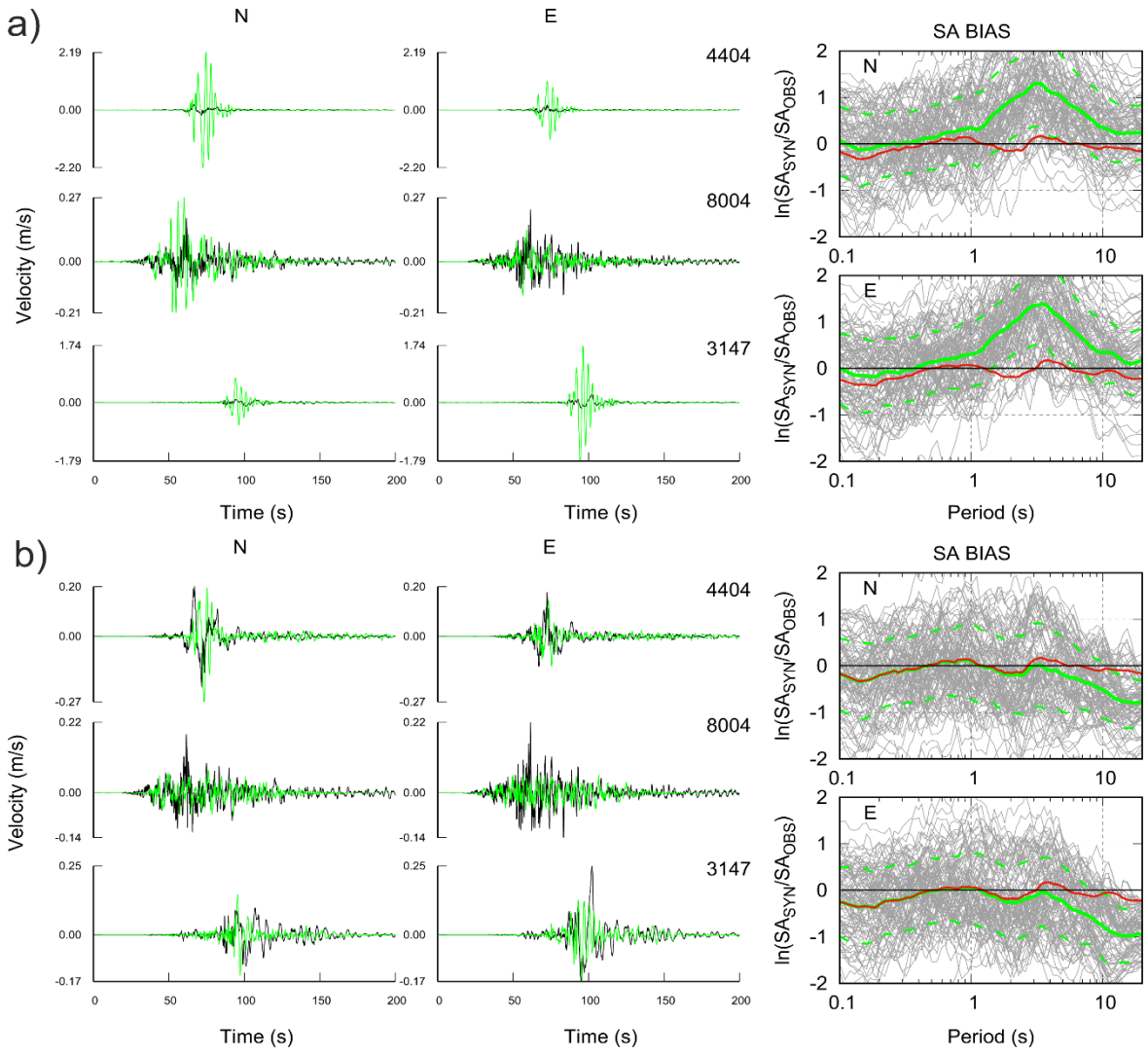

Figure 2.6: Effect of rupture velocity and delay of the SW fault segment on broadband synthetic (green) and observed (black) velocity waveforms. a) When assuming the rupture velocity of 2.5 km/s instead of 3 km/s considered in the preferred model (Test I), the peak values are underestimated, and the directivity pulse is weakened. b) When neglecting the delay in the SW segment (Test II), the main pulse arrives too early than the observed one at western stations 8004 and 3147. Contrarily, the eastern station 4404 remains unaffected.

We point out that the preferred frequency ranges are smaller than ~1 Hz, typically assumed in broadband simulation methods that combine the deterministic calculations at low frequencies with stochastic approaches at high frequencies (e.g., Graves and Pitarka, 2010). Ameri et al. (2012) used considerably higher crossover frequency ranges (1.5-2 Hz for near-field and 0.15-0.6 Hz for far-field stations) in their modeling of the Mw6.3 L'Aquila earthquake, perhaps due to the smaller magnitude of the studied event. The loss of coherency needed even for the very near-fault stations suggests complexity in the rupture propagation at short scales. In dynamic rupture modeling, such an effect can be attained by considering small-scale random variability of rupture geometry (Taufiqurrahman et al., 2022) and/or random perturbations of the fracture energy and initial stress (Gallovič and Valentová, 2023). Nevertheless, the composite model is an efficient, practical approach that approximates such strong heterogeneity of the rupture

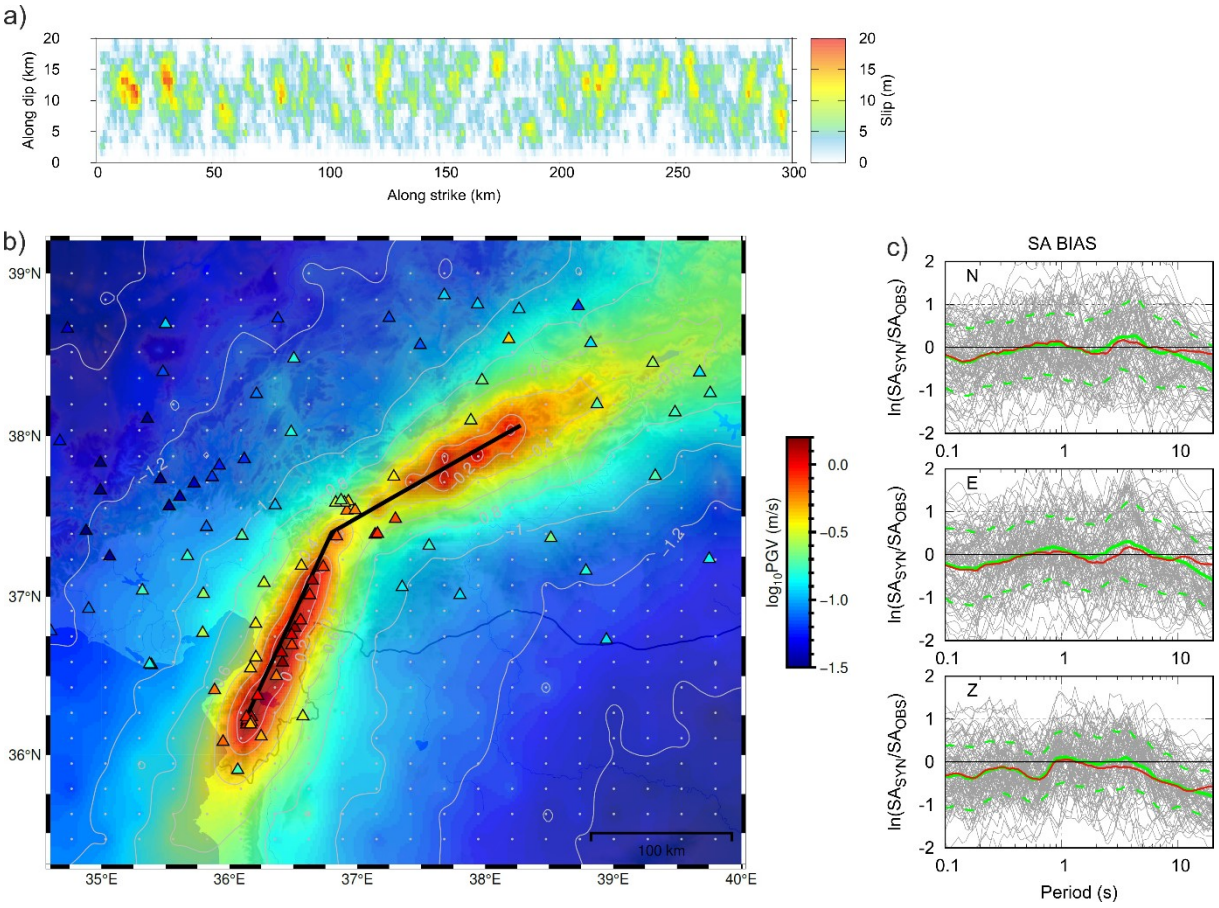

Figure 2.7: Effect of slip distribution constraint (Test III). Here we assume a uniform spatial probability density function for the subsources instead of constraining them by the GNSS slip inversion. a) HIC model slip distribution obtained by summing all the subsource contributions. b) Horizontal peak ground velocities (GMRotD50 PGV) interpolated from simulated seismograms at virtual stations; compare with Fig. 2.4a. Black line shows the vertical fault plane. Real stations are shown by triangles color-coded by observed PGV. c) Modeling spectral acceleration (SA) bias as a function of period (gray lines). Mean and ±1 standard deviation over stations are shown by green solid and dashed lines, respectively. The red line is the mean SA bias for the preferred model (Fig. 2.3b) for reference.

propagation at short scales by the incoherent summations of the wavefield contribution from subsources treated as point sources.

Crustal velocity model

Both ISOLA and HIC use code Axitra (Cotton and Coutant, 1997) based on the discrete wavenumber method (Bouchon, 1981) to calculate synthetic full-wavefield Green's functions in the full frequency range in a 1D layered medium. For the low-frequency inversion by ISOLA, we employ the 1D velocity model of Acarel et al. (2019), see Tab. S2.2. The model has a 2-km thick subsurface layer with S-wave velocity Vs of 2.78 km/s, which is adequate for low-frequency modeling but does not sufficiently describe site effects. For the broadband modeling, we have thus added 5 shallow layers to approximate a generic rock site with 800 m/s subsurface Vs30 S-wave velocity, see Tab. S2.3. Fig. S2.6 shows how adding these layers correct the systematic frequency dependent-underestimation of synthetics present in the spectral bias plot with the original velocity model.

Sensitivity of the broadband model

Lower rupture velocity (Test I). Fig. 2.6a illustrates the effect of assuming a lower rupture velocity v_r = 2.5 km/s on velocity waveforms for three selected stations, namely 8004, lying west of the fault kink, and stations 4404 and 3147 located at the NE and SW terminations of the rupture, respectively. The directivity pulses are less well-fitted at the three stations. In particular, at NE station 4404, the single pulse at the north component splits in two with smaller amplitudes, unlike in the observations. Similar effects can be seen on the east component of station 3147 lying in SW. We point out that the described effects are consonantly affecting other stations in similar directions.

No rupture delay in the SW segment (Test II). If the 15-s rupture delay of the SW segment is not considered, the directivity pulses of the velocity synthetics in the SW stations arrive systematically too early. It is visible in Fig. 2.6b for station 3147 lying close to the SW termination of the rupture. Contrarily, stations lying to NE, such as 4404 in Fig. 2.6b, remain unaffected as the wavefield contribution from the opposite side of the fault is minor, due to the geometrical distance. Station 8004, located west of the NE part of the fault, but north of the SW segment, also exhibits poor timing of the synthetic initial directivity pulse, suggesting that the rupture was delayed already at the intersection (junction) between EAF and the NNE-striking Narlı splay fault, not at the fault kink. Note that the physical mechanism for the time delay of the rupture backpropagating along EAF from the junction towards SW was also independently proposed by Abdelmeguid et al. (2023) and Jia et al. (2023). Indeed, their dynamic simulation shows that the SW rupture propagation along EAF became mechanically viable only after enough stress drop (and thus slip) occurred along the NE part of EAF.

Uniform distribution of subsources (Test III). We test a generic model unconstrained by the GNSS data. Here we assume a uniform spatial PDF for the distribution of the subsources; see an example in Fig. 2.7a. The slip distribution is still heterogeneous but does not concentrate in asperities as in Fig. 2.2c. All other parameters, including the time delay of the SW fault branch, remain the same. Fig. 2.7b shows the resulting PGV map. Both the constrained (Fig. 2.4a) and unconstrained PGV maps are similar along the SW branch of the rupture, while the PGV values are smaller for the unconstrained model of Fig. 2.7b along the NE segment, especially in the epicentral area. The latter is because the near-fault PGVs are dictated by the directivity pulse that develops only after the rupture passes a sufficient distance. Nevertheless, as confirmed by the SA bias in Fig. 2.7c, the fit is like that of the preferred model. This test suggests that the details of the slip distribution are less important than other source parameters, even at near-fault regions.

2.6. Supplemental Material

Table S2.1. Multiple point-source seismic model (subevents ordered with increasing time). The notation A-F refers to Fig. 2.1 and Fig. 2.2 of the main text.

Lat (°)	Lon (°)	Time (s)	Moment (x1020 Nm)	Strike (°)	Dip (°)	Rake (°)	Notation
37.3680	37.1418	0.00	0.34957	30.	90.	0.	A
37.6013	37.3516	12.6	1.91770	60.	90.	0.	B
37.7952	37.6532	23.4	0.38297	60.	90.	0.	C
37.9654	38.1347	33.3	0.81435	60.	90.	0.	D
37.0584	36.6329	36.0	0.53111	30.	90.	0.	E
36.4041	36.2696	58.5	0.61556	30.	90.	0.	F

Table S2.2. Velocity model of Acarel et al. (2019) used for low-frequency inversions.

Layer top depth (km)	Vp (km/s)	Vs (km/s)	Density (g/cm3)	Qp	Qs
0.000	4.850	2.780	2.670	500	250
2.000	5.720	3.280	2.844	500	250
8.000	5.770	3.310	2.854	500	250
12.000	5.840	3.360	2.868	1000	500
16.000	6.080	3.520	2.916	1000	500
20.000	6.190	3.570	2.938	1000	500
24.000	6.280	3.610	2.956	1000	500
28.000	6.400	3.680	2.980	1000	500
32.000	7.400	4.180	3.180	1000	500
34.000	7.550	4.340	3.210	1000	500
38.000	7.840	4.380	3.268	1000	500
42.000	7.950	4.520	3.290	1000	500

Table S2.3. Velocity model of Acarel et al. (2019) with added shallow layers for broadband modeling, approximating a generic rock station with Vs30 = 800 m/s.

Layer top depth (km)	Vp (km/s)	Vs (km/s)	Density (g/cm3)	Qp	Qs
0.000	1.490	0.800	1.900	100	50
0.060	2.230	1.200	2.000	200	100
0.160	3.160	1.700	2.100	400	200
0.250	3.900	2.100	2.250	500	250
0.500	4.460	2.400	2.400	500	250
1.000	4.850	2.780	2.670	500	250
2.000	5.720	3.280	2.844	500	250
8.000	5.770	3.310	2.854	500	250
12.000	5.840	3.360	2.868	1000	500
16.000	6.080	3.520	2.916	1000	500
20.000	6.190	3.570	2.938	1000	500
24.000	6.280	3.610	2.956	1000	500
28.000	6.400	3.680	2.980	1000	500
32.000	7.400	4.180	3.180	1000	500
34.000	7.550	4.340	3.210	1000	500
38.000	7.840	4.380	3.268	1000	500
42.000	7.950	4.520	3.290	1000	500

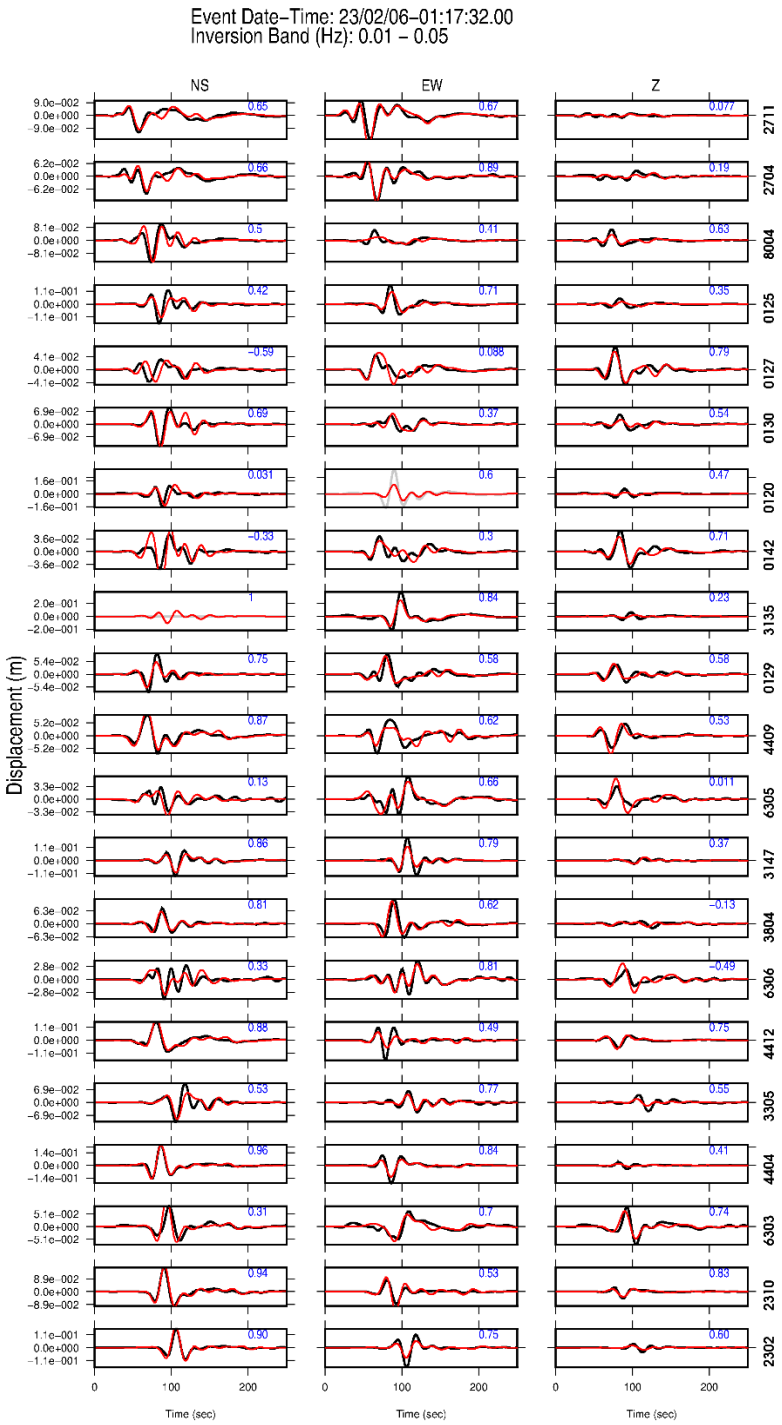

Figure S2.1. Waveform fit between observed (black) and synthetic (red) displacement data for the multiple point-source model of Fig. 2.1 (see the station locations therein); frequency range 0.01-0.05 Hz, global variance reduction VR = 0.70. Blue numbers depict VR per component. The 0120 (E) and 3135 (N) components were not inverted due to instrumental disturbance (abrupt change of baseline); for plotting, the 3135 (E) observed trace was zeroed.

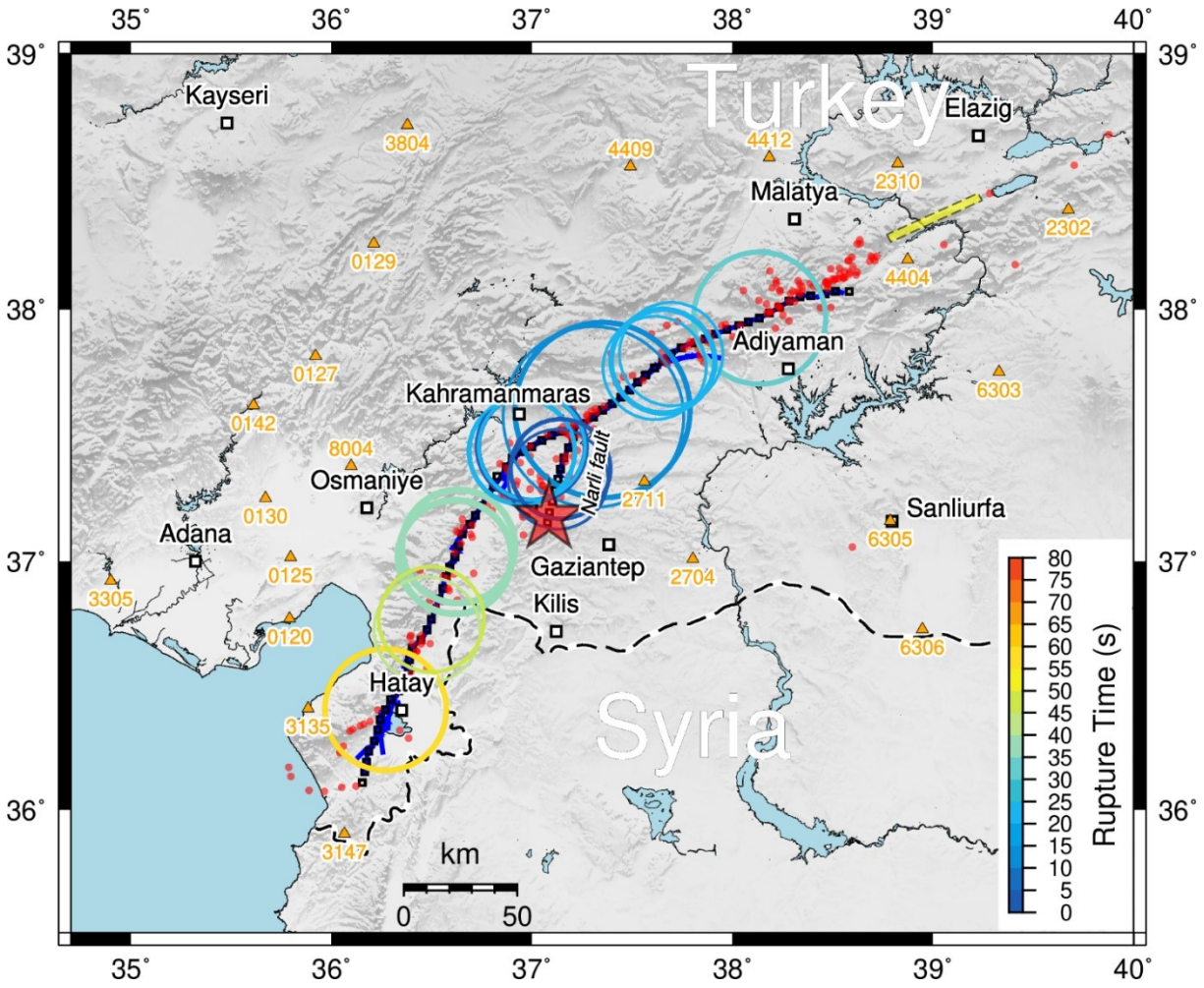

Figure S2.2. Stability of the seismic model by a jackknife test. Analogy of Fig. 2.1 of the main text. Instead of beachballs, subevents are shown by concentric circles with radii scaled assuming constant stress drop (i.e., seismic moment to power 1/3), and colored with rupture time. The concentric circles represent variability during repeated inversions in which each time one station is removed from inversion (a jackknife test).

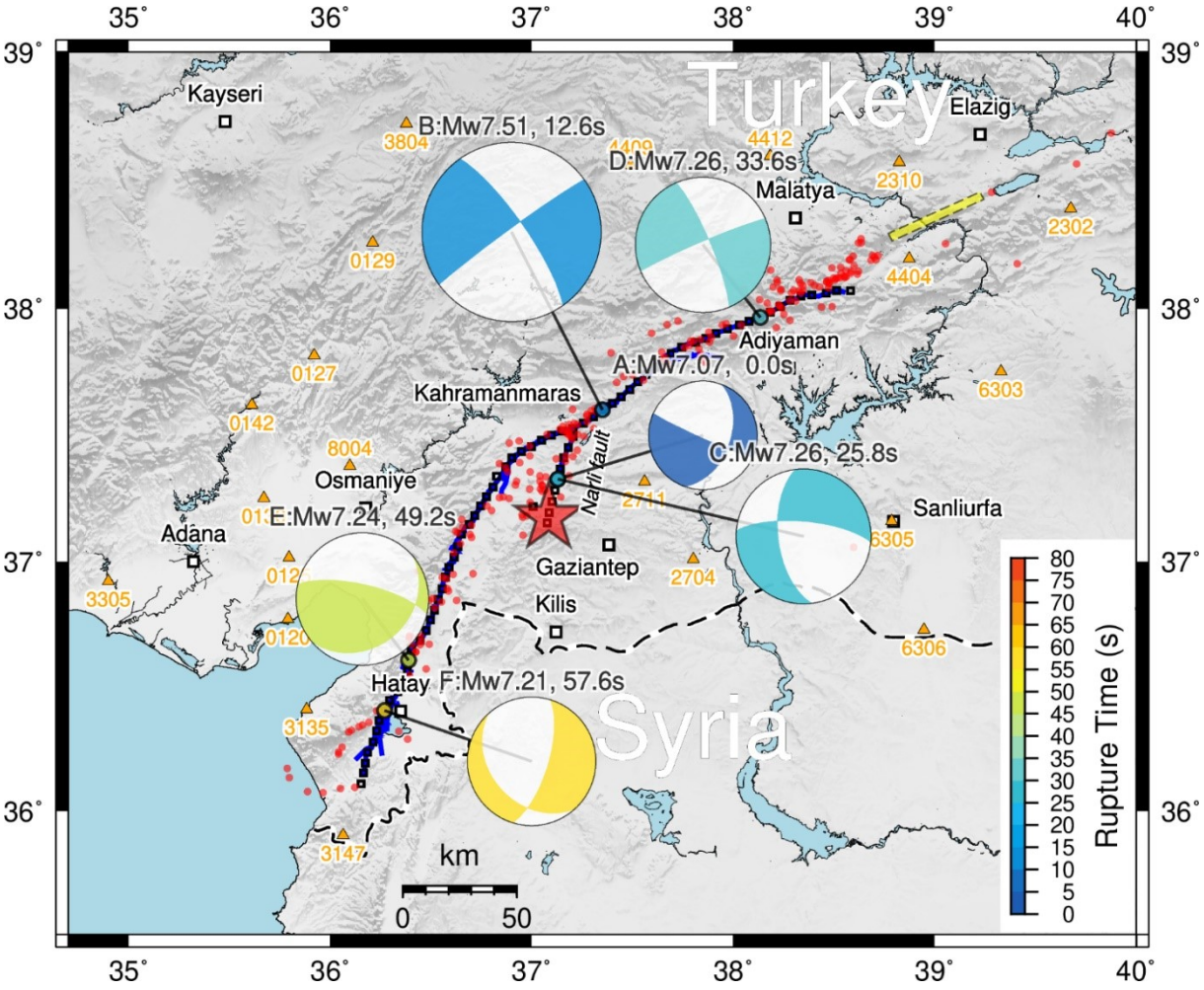

Figure S2.3. The best-fit seismic model with free DC-constrained mechanisms. Notation as in Fig. 2.1 of the main text. Major subevents B and D remain the same as with the constrained-mechanism solution of Fig. 2.1. Position and timing of the earliest weak subevent (A) also remain unchanged. Subevent C (time ~25 s) is mislocated on the Narlı fault.

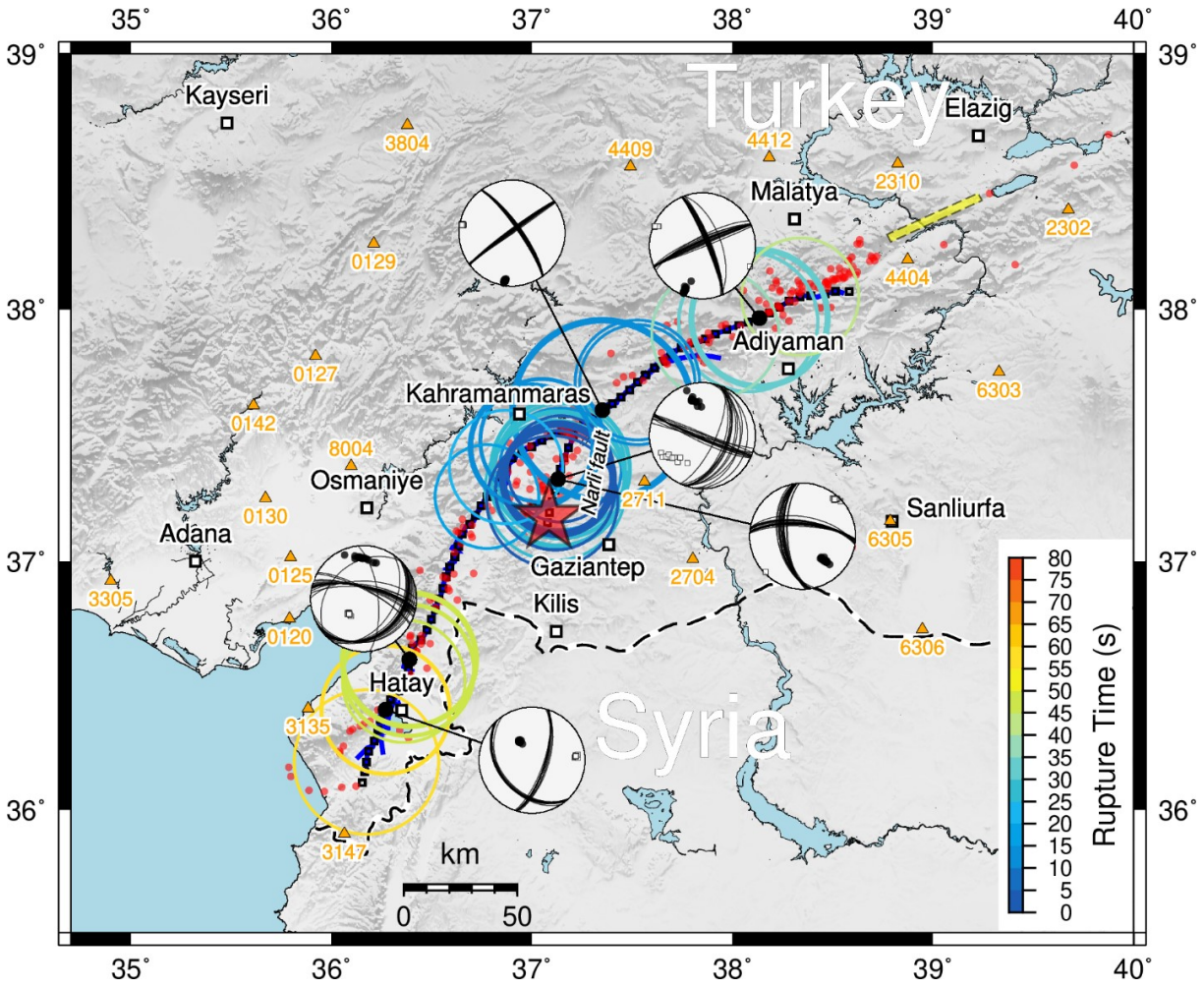

Figure S2.4. Limited stability of the model with free DC-constrained mechanisms. Notation as in Fig. S2.3. P and T axes in beachballs are shown by the filled and open symbols, respectively.

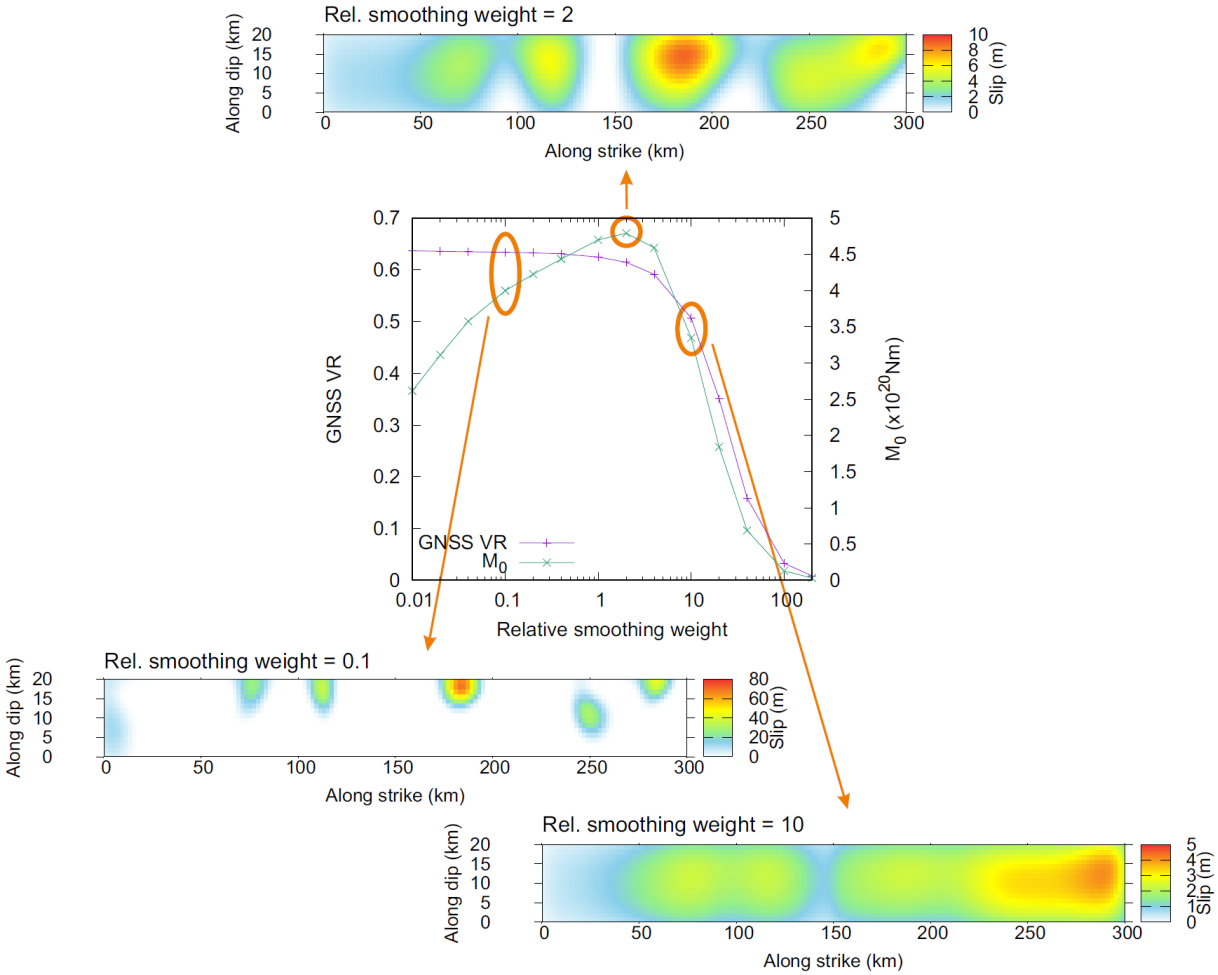

Figure S2.5. Inversion of GNSS data using various relative smoothing weights. Compare with Fig. 2.2 of the main text. The middle graph shows the dependence of the GNSS variance reduction and resulting seismic moment on the relative smoothing weight parameter of the inversion. The three slip distributions are examples for weak (bottom left), strong (bottom right), and preferred (top) choices of the smoothing strength; note the different color scales. The latter model is characterized by good variance reduction and maximum seismic moment, and is used in the main text to constrain the distribution of the HIC model subsources.

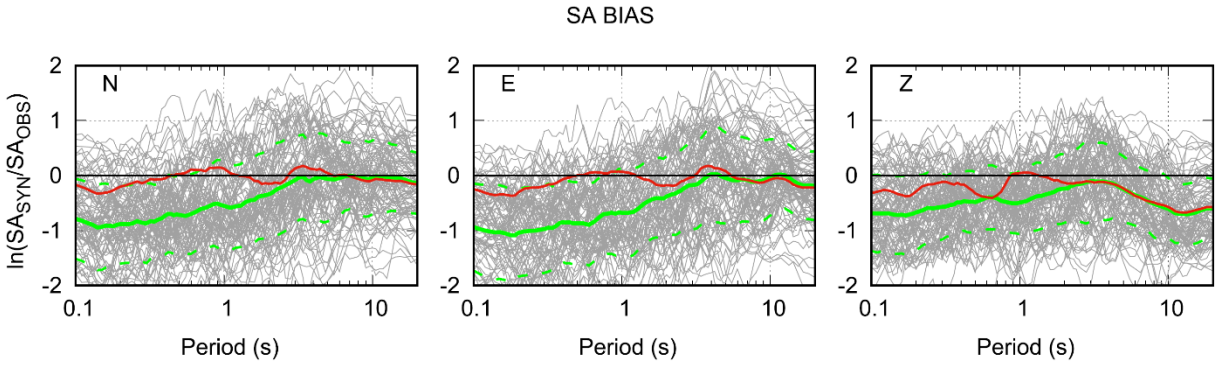

Figure S2.6. Effect of shallow low-velocity layers of the crustal model considered in the broadband modeling. Modeling spectral acceleration (SA) bias as a function of the period (gray lines) when considering the original velocity model of Acarel et al. (2019), see Tab S2. Mean and ±1 standard deviation over stations are shown by green solid and dashed lines, respectively. The systematic negative bias at low periods confirms the necessity of considering a realistic decrease of seismic velocities towards the surface. Indeed, in the case of the preferred model that includes such shallow low-velocity layers, see Tab. S3, the mean SA bias is closer to zero (red line, same as in Fig. 2.3b).

Figure S2.7 (the map following this caption and waveforms available in Supplemental material at: https://www.nature.com/articles/s43247-023-01076-x#Sec16). Multi-slide comparison of seismograms (displacements, velocities, accelerations) and smoothed acceleration amplitude spectra of all 100 stations and components in frequency range 0.05-10 Hz. Data and synthetics are in black and red, respectively. Waveforms start at the origin time 1:17:32.0 UTC. Station locations are shown on the first slide and also below here.

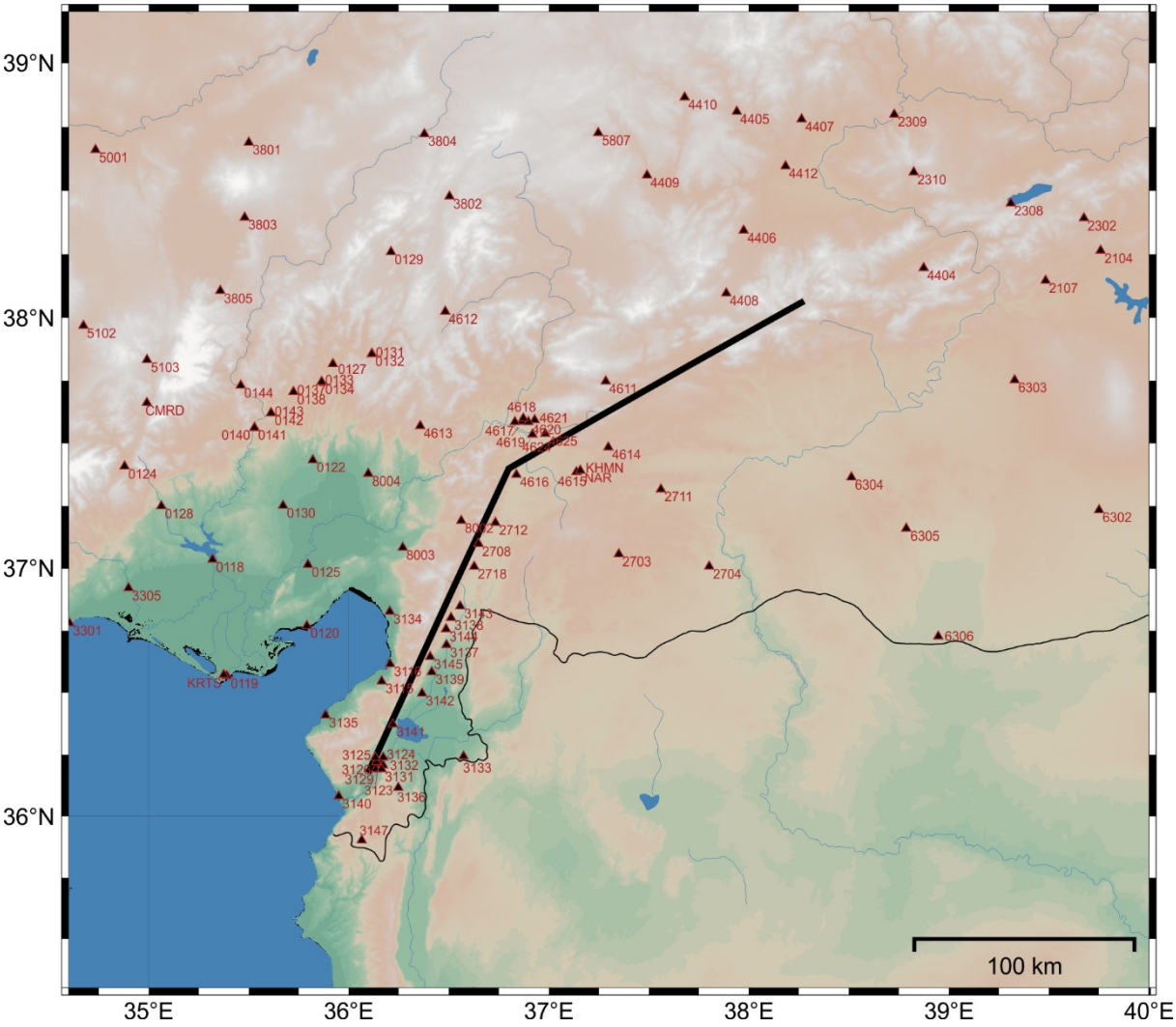

3. Ground motion modeling of the 2016 Mw6.2 Amatrice (Italy) earthquake by a broadband hybrid kinematic approach, including empirical site effects

This chapter was published as Čejka et al. (2024a) in Seismological Research Letters. We made only small notational and stylistic edits

3.1. Abstract

The region of Central Italy is well known for its moderate to large earthquakes. Events such as the 2016 Mw6.2 Amatrice earthquake generated in the shallow extensional tectonic regime motivate numerical simulations to gain insights into source-related ground motion complexities in the near-source region. We utilize a hybrid integral-composite kinematic rupture model by Gallovič and Brokešová (2007) to simulate the Amatrice earthquake in a broadband frequency range (up to 10 Hz). In the first step, we optimize the input source parameters using a grid-search method by minimizing the spectral acceleration bias between synthetic and recorded strong-motion data at reference rock stations within 50 km of the source. To verify the robustness of the optimal model, we simulate the ground motions at 400 virtual stations and compare their spectral accelerations with the predictions of an empirical nonergodic ground motion model (GMM) for rock sites in Central Italy (Sgobba et al., 2021). The synthetics show a good agreement with the empirical model regarding both median and variability. Finally, we account for local site effects at non-reference stations by combining the simulations on rock with empirical site terms derived by the nonergodic GMM. The site-corrected spectral responses generally improve the match with the observations, demonstrating a successful fusion of numerical simulations with empirical estimates toward reproducing near-source ground motions.

3.2. Introduction

The Central Italy region is well known for its relatively large seismicity and complex tectonic structure. It features mainly seismogenic NNW-SSE-oriented structures driven by the extensional tectonic regime of the Central Apennines. Many damaging earthquakes struck this area over the last centuries, the most recent being the 2009 Mw6.3 L'Aquila event and the 2016–2017 Amatrice–Visso–Norcia seismic sequence. This sequence was initiated by the Mw6.2 Amatrice earthquake on August 24, 2016, 01:36 UTC, with the most devastating consequences, causing 299 fatalities, building collapses, and damage with macroseismic intensities up to XI (Galli et al., 2016). The earthquake ruptured NW-SE oriented normal fault located in the south-east bend of the Sibillini Thrust which is a main compressional structure in the area (Pizzi et al., 2017; Fig. 3.1a). Given the significance of this event, several studies in the literature have focused on the implementation of advanced simulation techniques to generate synthetic waveforms in a broad frequency range, e.g., with hybrid methods (Pischiutta et al., 2016; Pischiutta et al., 2021), or dynamic models (Gallovič et al., 2019; Taufiqurrahman et al., 2023; Gallovič and Valentová, 2023).

The physics-based ground motion simulations are a promising tool to fill the observational gaps in the near-source region (Ameri et al., 2012; Bradley et al., 2017; Paolucci et al., 2021; Valentová et al., 2021; McCallen et al., 2021; Pitarka et al., 2021a, 2021b), connecting various source-related complexities, such as the distribution of slip, rupture time, rise time, with peculiar features of the spatial distribution of observed shaking due to radiation pattern and directivity. They can also complement the empirical

ground motion models (GMMs) that are one of the main prediction tools used in seismic hazard assessment, especially in the epicentral areas, and for evaluating the seismic response of strategic structures such as power plants, infrastructure or buildings in urban areas. For example, the so-called hybrid simulations are employed frequently due to their efficiency in a broad frequency range (Mai and Beroza, 2003; Gallovič and Brokešová, 2007; Graves and Pitarka, 2010; Graves et al., 2011; Paolucci et al., 2018). The hybrid methods combine the high-frequency stochastic approaches (e.g., von Karman distributions) with the deterministic rupture models at low frequencies that may come from kinematic source inversions (Ameri et al., 2012; Razafindrakoto et al., 2018; Ojeda et al., 2021; Pischiutta et al., 2021) or even dynamic source modeling (Akinci et al., 2017). Unlike the empirical GMM, the ground motion simulations can provide a 3-component time series comprising complex source and propagation effects. Yet, their results need to be validated against observations to simulate reliable ground shaking.

In this work, we simulate broadband (up to 10 Hz) strong ground motions of the Mw6.2 Amatrice earthquake using the Hybrid Integral-Composite (HIC) kinematic model of a finite-extent rupture introduced by Gallovič and Brokešová (2007). The wave

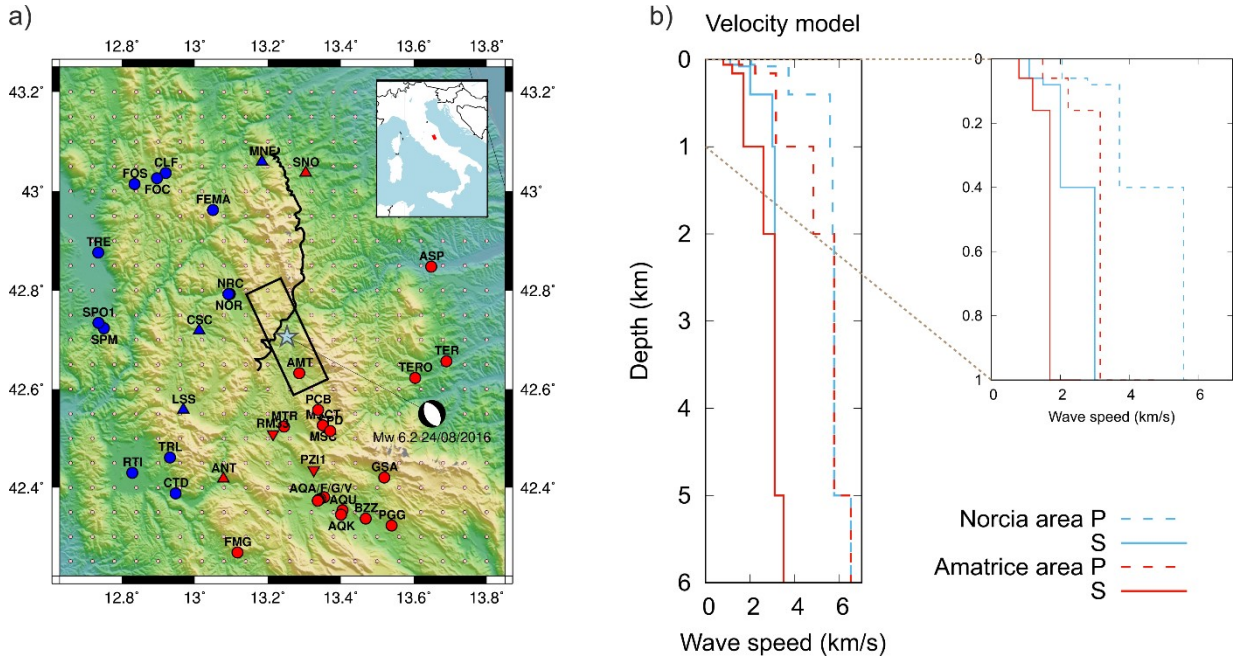

Figure 3.1: Study area and velocity models. a) Epicentral area of the 2016 Amatrice earthquake. The fault plane adopted from Pizzi et al. (2017) is shown by the black rectangle. Network stations are shown by triangles and circles, color-coded by the adopted crustal model: Circles correspond to the non-reference station, triangles to the reference stations with all components used in the model optimization, and inverted triangles depict stations for which only vertical components are considered in the optimization. The faulting mechanism and centroid location are shown by the beach ball (INGV-webservice). Mainshock epicenter (light blue star) is adopted from the relocated catalog by Chiaraluce et al. (2017). Black curves correspond to the Sibillini Thrust separating different crustal regimes of the Norcia and Amatrice area. Pink circles are 400 virtual stations used for comparison with a ground motion model. The inset shows a map of Italy with the study area depicted by a black rectangle. b) Velocity models used to calculate Green's functions for stations in the Norcia (blue) and Amatrice (red) area, see also Tab. S1. The models coincide below 2 km. The inset zooms in the uppermost 1 km.

propagation is implemented by numerical calculation of synthetic Green's functions (GF) in regional 1D crustal velocity models in a broad frequency range. The HIC approach was previously validated by modeling several strong earthquakes, e.g., the 1980 Mw6.9 Irpinia (Central Italy; Ameri et al., 2011), the 2009 Mw6.3 L'Aquila (Central Italy; Ameri et al., 2012), the 2011 Mw7.1 Van (Eastern Turkey; Gallovič et al., 2013), or recently the 2023 Mw7.8 Kahramanmaraş (Turkey; Čejka et al., 2023) earthquakes.

In the first step, we calibrate source-related parameters of the HIC method on a set of reference stations best matching the observed data given a specific metric (Graves and Pitarka, 2010; Ojeda et al., 2021). In this primary calibration phase, in addition to the metric adopted to assess the goodness of fit of the model, the choice of the reference sites also plays a critical role, given the complexity of the geomorphological setting in Central Italy (Felicetta et al., 2021, and references therein). In this case, the number of reference stations is limited and thus two validation exercises are performed to support the applicability of the optimal source model: i) comparison of the simulated ground motions of the 2016 Amatrice earthquake on a dense set of virtual rock-site stations with the predictions of regional nonergodic GMM (SEA21, Sgobba et al., 2021), and ii) comparison of ground motions with recordings at non-reference stations with significant site effects, representing additional observations independent of the optimization process. As for the latter, we correct the synthetic acceleration spectra simulated on rock by empirical site amplification functions derived from nonergodic GMM calibrated in Central Italy (Sgobba et al., 2024).

This work, in addition to validating the broadband source model of the 2016 Amatrice earthquake on a smaller set of reference stations, follows a more systematic approach by integrating empirical amplification functions in numerical simulations over a more comprehensive data set in a broad frequency range, taking advantage of the complete consistency in modeling assumptions. Our study, therefore, aims to propose a methodological example for correcting the simulated ground motions on rock with the repeatable site contributions of nonergodic GMM to reproduce the ground motions on generic sites. This task is very challenging and thus possible only in densely monitored areas and with good empirical estimates, such as Central Italy.

3.3. Data and methods

Near-source recordings

Due to the frequent seismicity, the Central Apennines in Italy are well covered by seismic stations belonging to the National Accelerometric Network (code IT, operated by the Italian Department of Civil Protection, DPC) and the National Seismic Network (code IV, operated by the Istituto Nazionale di Geofisica e Vulcanologia, INGV). The Amatrice earthquake was recorded by 38 accelerometric stations of the IV and IT permanent networks within 50 km of the epicenter (Fig. 3.1a), see Data and resources. For model calibration, we choose seven reference stations with weak or no site amplifications selected using the multiproxy technique RRIM (Reference Rock Identification Method)

developed by Lanzano et al. (2020, 2022) (colored triangles in Fig. 3.1a). This approach identifies reference recording stations on the base of several proxies for the site response, related both to the analysis of geophysical and seismological data and to the geomorphological features of the site. Almost all the selected reference stations are installed on rigid soils with V_{s30} varying in the 550-1100 m/s range and are free from resonance phenomena (see Tab. S3.1).

The reference sites considered in the model optimization comprise two groups: the first contains five stations, already identified as reference in Lanzano et al. (2022), for which all three components are used (LSS, MNF, ANT, SNO, CSC; upside triangles in Fig. 3.1a); the second group includes two additional stations, for which we consider only the vertical components, (PZI1, RMM33; inverse triangles in Fig. 3.1a). Although they do not exhibit prominent amplifying effects, they do not exceed the minimum score selected in the RRIM methodology to be classified as good reference sites. They were included in the optimization to improve the azimuthal coverage towards the south.

We filter all recordings by a Butterworth filter between 0.05 and 10 Hz.

Source model

In the Hybrid Integral-Composite (HIC) technique, the rupture process is represented by overlapping rectangular subsources randomly distributed on the fault with fractal number-size distribution, where the number of subsources decreases linearly with increasing subsource size. The subsources are characterized by a constant stress-drop scaling, composing a slip distribution with k^{-2} decay at high wavenumbers k. These subsources are treated differently in the low- and high-frequency ranges, and each of these procedures results in a seismogram in partially overlapping frequency bands. Below, we explain the two methods in more detail (see also Gallovič and Brokešová, 2007).

- Up to f_2, the *integral* of the representation theorem is calculated: The fault is discretized to a regular grid of subfaults. At each subfault, the slip is computed as a sum of contributions from all subsources covering the subfault. The rupture time is calculated from the distance of the point to the nucleation point and the prescribed (constant) rupture velocity. The slip velocity function has Brune's pulse shape with constant rise time. The synthetic waveforms are obtained by convolving slip rates with Green's functions (GFs), calculated from the center of each subfault, and subsequently summing all subfaults' contributions over the fault. The advantage of this approach is that the directivity of the rupture propagation is well captured at lower frequencies due to the coherent summation of the subfaults' wavefield contributions.
- Above f_1, *the composite* approach is used: The individual subsources are treated as point sources with Brune's source time function, described by their respective seismic moments and corner frequencies (assuming the constant

stress drop). In addition, we allow a random variation in the mechanism of the subsources to weaken the radiation pattern at high frequencies. Synthetics for a given subsource are obtained by convolution of the Brune source time functions (Brune, 1970) with GFs calculated from the subsources' centers. These contributions are then shifted in time by their respective rupture times, calculated as the time the rupture needs to reach the subsource, considering a constant rupture velocity. All the subsources' contributions are then summed. In contrast to the integral part, the directivity effect is suppressed due to the incoherent summation of the subsources' wavefield contributions.

The cross-over frequency section (f_1, f_2) is treated in the Fourier domain by weighted averaging of the real and imaginary parts of the two seismograms from the two approaches using $\cos^2$ and $\sin^2$ functions as weights. Since the low- and high-frequency synthetics are based on the same subsource distribution and synthetic Green's functions, the cross-over combination does not require any specific manual fine-tuning.

The subevents' corner frequencies are adjusted so that the resulting high-frequency acceleration plateau of the event has a prescribed height. For the omega-square source model, the height of the acceleration spectral plateau is equal to $M_0\hat{f}_c^2$ with M_0 and $\hat{f}_c$ being the total scalar seismic moment and the event corner frequency, respectively. In the HIC model, we generalize the corner frequency as

$$\hat{f}_c = \frac{av_r}{\sqrt{LW}}, \tag{3.1}$$

where L and W are the rupture length and width, respectively, v_r is the rupture velocity, and parameter a is a parameter controlling the strength of the high-frequency radiation, with a value close to 1 as suggested by previous studies (Ameri et al., 2009, Ameri et al., 2011; Gallovič and Brokešová, 2007; etc.).

To validate the HIC source model for the Amatrice earthquake, we adopt a fixed fault plane, M_0 and subsource layout similar to the slip model from Bayesian dynamic source inversion by Gallovič et al. (2019). The optimization parameters are rupture velocity v_r and parameter a.

Crustal velocity models

To calculate the synthetic waveforms, we employ the synthetic GFs that were pre-calculated in the 1D velocity models using the Axitra code (Cotton and Coutant, 1997). The GFs are filtered in the frequency range 0.05-10 Hz, the same as used for the records.

We consider a specific 1D velocity model for each of the two major geological domains divided by the Sibillini Thrust, which is the main structural discontinuity in the area (Fig. 3.1a): i) the SSE unit of the Sibillini Thrust, which lies on the Laga formation (Amatrice area) and ii) the carbonate unit to the NNW of the thrust (Norcia area). For the Amatrice area, we adopt the crustal velocity model proposed by Ameri et al. (2012) which showed

a good fit between the observed and simulated ground motions for the 2009 L'Aquila earthquake. The crustal model was supplied by three subsurface layers in dynamic source modeling of the 2016 Amatrice earthquake by Gallovič et al. (2023) resulting in a good fit of broadband ground motions with both observations and regional GMM. For the Norcia area, we adapt the 1D velocity model of Bianchi et al. (2010) in the topmost kilometer by resampling the shear wave array profile Vs performed at stations CSC (Cascia) and LSS (Leonessa). The results of the above-mentioned geophysical measurements are available in the ITACA database (see Data and resources). For the GF calculation, the fault is embedded completely in the northern and southern medium for northern and southern stations, respectively. However, since the two models differ only up to 2 km depth, where almost no slip is generated, neglecting two different crustal models on the fault has negligible effect. The two velocity models proposed for the Amatrice and Norcia area are shown in Fig. 3.1b and Tab. S3.2.

The anelastic attenuation is modeled by depth-dependent quality factor Q (see also Tab. S2 and Fig. S3.1) and high-frequency decay parameter κ (Anderson and Hough, 1984). Following Castro et al. (2022), we adopt κ = 0.03 s as a mean value for all the stations. The effect of different choice of κ on ground motion is explored in the Supplementary Text S3.1 and Fig. S3.2.

Evaluation of the modeling performance

To assess the fit between the simulated ground motions and the observations, we adapt the method of Graves and Pitarka (2010). Firstly, we evaluate the logarithm of the ratio between spectral acceleration (SA, 5% damping) of synthetic records and observed data,

$$r_j(T_i) = ln\left(\frac{M_j(T_i)}{O_j(T_i)}\right), \tag{3.2}$$

where $r_j(T_i)$ is an SA residual at each station's component j and period T_i, and O_j and M_j are observed and modeled SA responses, respectively. Then we compute the model's SA bias at each period as

$$B(T_i) = \frac{1}{N}\sum_{j=1}^{N} r_j\,(T_i), \tag{3.3}$$

where N is the number of all site components considered in the model assessment.

The standard deviation $\sigma(T_i)$ is computed as

$$\sigma(T_i) = \left\{\frac{1}{N}\sum_{j=1}^{N}\left[r_j(T_i) - B(T_i)\right]^2\right\}^{1/2}. \tag{3.4}$$

To describe the model fit by a single number, B^2-value, we take the average of $B^2(T_i)$ over all periods, i.e.,

$$B^2 = \frac{1}{M}\sum_{i=1}^{M} B^2\,(T_i), \tag{3.5}$$

where M is the number of periods. The optimal model is chosen as the one with minimal B^2-value over the source parameters.

Here we deviate from the standard approach of Graves and Pitarka (2010), in which the B-value is calculated as an average value of SA bias over all stations, periods and components. In our experience, this can promote models that generate positive and negative SA bias over different periods, still having the B-value close to zero. Contrarily, taking the B^2-value as in Eq. (3.5) guarantees that the optimal model provides SA bias close to zero over the whole inspected period range.

We also explore the variability of the SA bias using the mean σ^2-value defined as

$$\sigma^2 = \frac{1}{M}\sum_{i=1}^{M} \sigma^2\,(T_i), \tag{3.6}$$

In an ideal case, the minima in the B^2 and σ^2 values overlap, suggesting that the optimal model generates ground motions most similar to the observed ones not only in average over the reference stations but also individually at each station (Gallovič, 2016).

Regional empirical ground motion models

To validate our optimal source model, we use empirical ground motion models in two ways: first, the simulated ground motions are validated against the GMM prediction using a grid of virtual rock sites; second, we combine empirical site correction terms evaluated from the GMM at non-reference stations with the simulated ground motions on rock and compare them with the observations.

In particular, we compare the synthetic predictions from HIC with a fully nonergodic GMM calibrated specifically for Central Italy by Sgobba et al. (2021), referenced as SEA21. In this nonergodic model, the variability terms are decomposed via mixed-effect regression and geospatial analysis into systematic effects of the path (δP2P), site (δS2S), source zone (δL2L), and event-specific correction (δB_e). The residual term δW_0 accounts for all other (nonsystematic) effects.

To evaluate the empirical ground motion for the Amatrice earthquake at rock sites using SEA21, the median prediction is corrected by δB_e and δL2L corrections specific to the Amatrice source. The corresponding standard deviation is then composed of the remaining variability terms due to the path (ϕ_{P2P}), the reference sites (ϕ_{S2Sref}), and aleatory standard deviation (ϕ_0). This process is used to ensure the best consistency between the empirical model and the numerically simulated features. For example, assuming the GMM generic median value without the event-specific correction can result in simulations overestimating the GMM, as the Amatrice-specific correction is positive. On the other hand, assuming the complete variability in GMM (between- and within-event

including non-reference sites) could be incorrectly interpreted as underprediction of variability in the simulated ground motions.

In the second step of our validation process, we aim to improve synthetic predictions at non-reference sites using empirical site functions named δS2S. These correspond to the systematic amplifications observed at generic sites over all events when compared to the median GMM prediction at the reference-rock level. We evaluate these functions as random-effect terms of the regression model which lacks an explicit scaling trend with V_{s30}, hence, they can be considered as amplification factors of the site in comparison to the reference-rock condition. Therefore, these functions are ideal proxies for the site response, as suggested by Bard et al. (2020) and Loviknes et al. (2021). Here, instead of considering the δS2S of Sgobba et al. (2021), which are based on a model calibrated on 36 reference sites, we prefer to adopt the site-to-site terms derived by Sgobba et al. (2024, SEA24) that are based on the same approach as SEA21 but calibrated only on 6 reference sites, including the three (LSS, MNF, SNO) used in this study in the optimization of the source model. In this way, the reference rock motions between the optimized simulations and the GMM predictions are consistent, facilitating the application of the SEA24

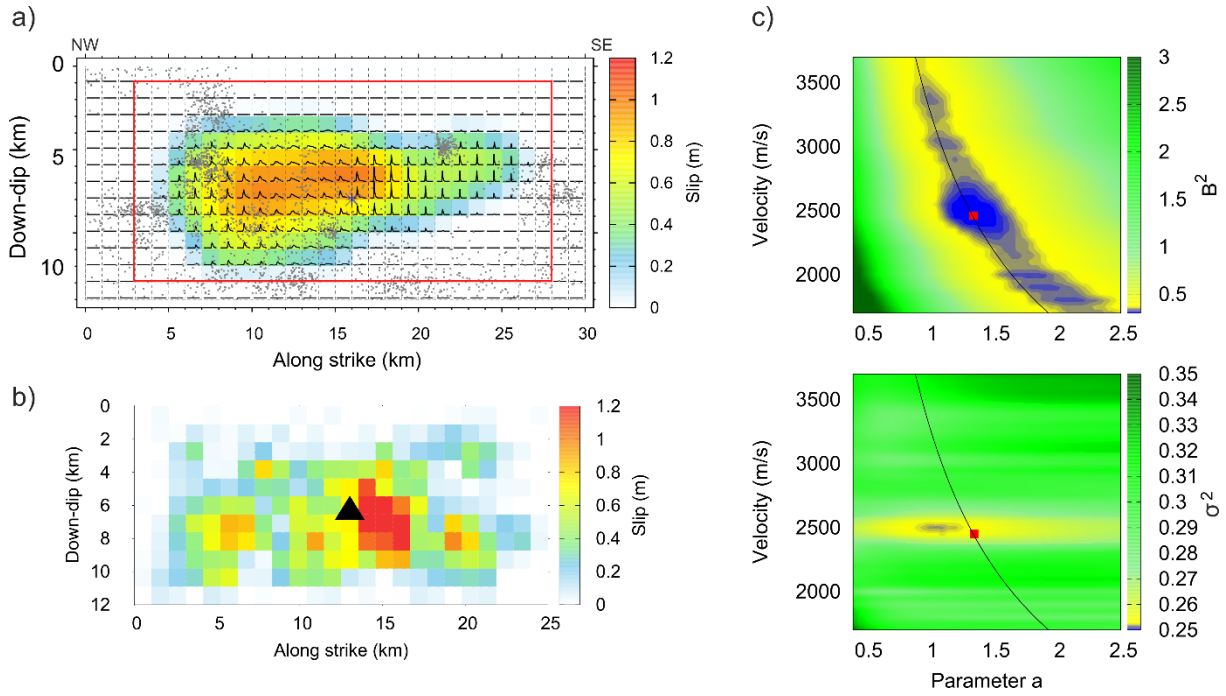

Figure 3.2: Slip model of the 2016 Amatrice earthquake and results of the optimization of the broadband model. a) Slip distribution of the 2016 Mw6.2 Amatrice earthquake from the dynamic source inversion by Gallovič et al. (2019). Blue star is the nucleation point, gray dots are aftershocks. Red rectangle depicts the area utilized in the HIC modeling. b) Slip distribution generated for the broadband modeling based on probability density in panel a). Black triangle is the nucleation point. c) Result of the grid search over parameters a and v_r for an optimal model of the 2016 Amatrice earthquake in terms of B^2 (top) and σ^2 (bottom) values (see Eqs. 3.2-3.6). The red square shows the model with minimal B^2 with v_r = 2.45 km/s and a = 1.35. Black line delineates models with the same corner frequency f_c as the optimal model (see Eq. 3.1).

empirical site corrections to the synthetic spectra. Note that the synthetics are not corrected for other systematic terms, such as δL2L and δP2P, as the kinematic simulations

have already been optimized for the source, and the propagation terms are negligible in our frequency range.

3.4. Results

Optimal HIC model of the Amatrice earthquake

Following the kinematic and dynamic source models of Pizzi et al. (2017) and Gallovič et al. (2019), we set the strike/dip/rake angles to 155/45/-85 degrees, the latitude, and longitude of the epicenter to 42.7063° N, 13.2532° E, and the scalar seismic moment to 2.6×10^{18} Nm. We resemble the best-fitting slip model of the dynamic source inversion by Gallovič et al. (2019) by fixing the fault dimension to 25x12 km^2 and randomly generating the subsources distribution considering the dynamic slip model as a spatial probability density function, see Figs. 3.2a and 3.2b.

The cross-over frequency range partitions the deterministic and stochastic rupture behavior and can be generally treated as a free parameter. To keep our validation simple, we adopt values that were found in a previous HIC application for an event of similar magnitude in Central Italy, the 2009 Mw6.3 L'Aquila earthquake (Ameri et al., 2012), i.e., f_1 = 0.15 Hz and f_2 = 0.6 Hz. The cross-over frequency range is presumably related to the corner frequency of the event (and thus magnitude) and covers the frequency band where the source directivity is generally observed (Pacor et al., 2016; Colavitti et al., 2022). Nevertheless, the precise values of the cross-over frequencies may be event-dependent; therefore, in Supplementary Text S3.2 and Fig. S3.3, we discuss the effects of different values on the modeling in more detail.

The rupture velocity v_r and parameter a are optimized with a grid search method. For parameter a, we assume range 0.4-2.5, with step 0.1. The rupture velocity is varied between 1.7 km/s and 3.7 km/s (close to the S-wave velocity), with a step of 0.1 m/s. The grid search results over v_r and a in terms of the B^2-value and σ^2-value are shown in Fig. 3.2c. The set of optimal models with lower B^2-values are distinguished in Fig. 3.2c by the blue-colored region. The optimal model with minimal B^2-value is characterized by parameter a = 1.35 and rupture velocity v_r = 2.45 km/s, slightly slower than in other studies (Cirella et al., 2018; Tinti et al., 2016; Gallovič et al., 2019).

The plot of the B^2-value in Fig. 3.2c exhibits a clear trade-off between parameters a and v_r. This trade-off can be explained by the pivotal role of corner frequency f_c in the waveform modeling (see Eq. 3.1). In our model, the corner frequency is also related to the so-called stress parameter, $\Delta\sigma = \frac{7}{16}\left(\frac{f_c}{0.37 v_s}\right)^3 M_0$, characterizing the high-frequency acceleration plateau. The optimal model has a corner frequency of 0.19 Hz and stress parameter of 3.6 MPa. Fig. 3.2c shows the line of constant corner frequency following Eq. (1), showing perfect agreement with the valley of low B^2-values. We note that our corner frequency and stress parameter are similar or lower than the empirical estimates for the Amatrice earthquake derived from empirical studies ranging 0.2-0.35 Hz and 3.4-9MPa,

respectively (Morasca et al., 2019; Morasca et al., 2022; Kemna et al., 2021; Supino et al, 2019; Calderoni and Abercrombie, 2023; Gallovič et al., 2019).

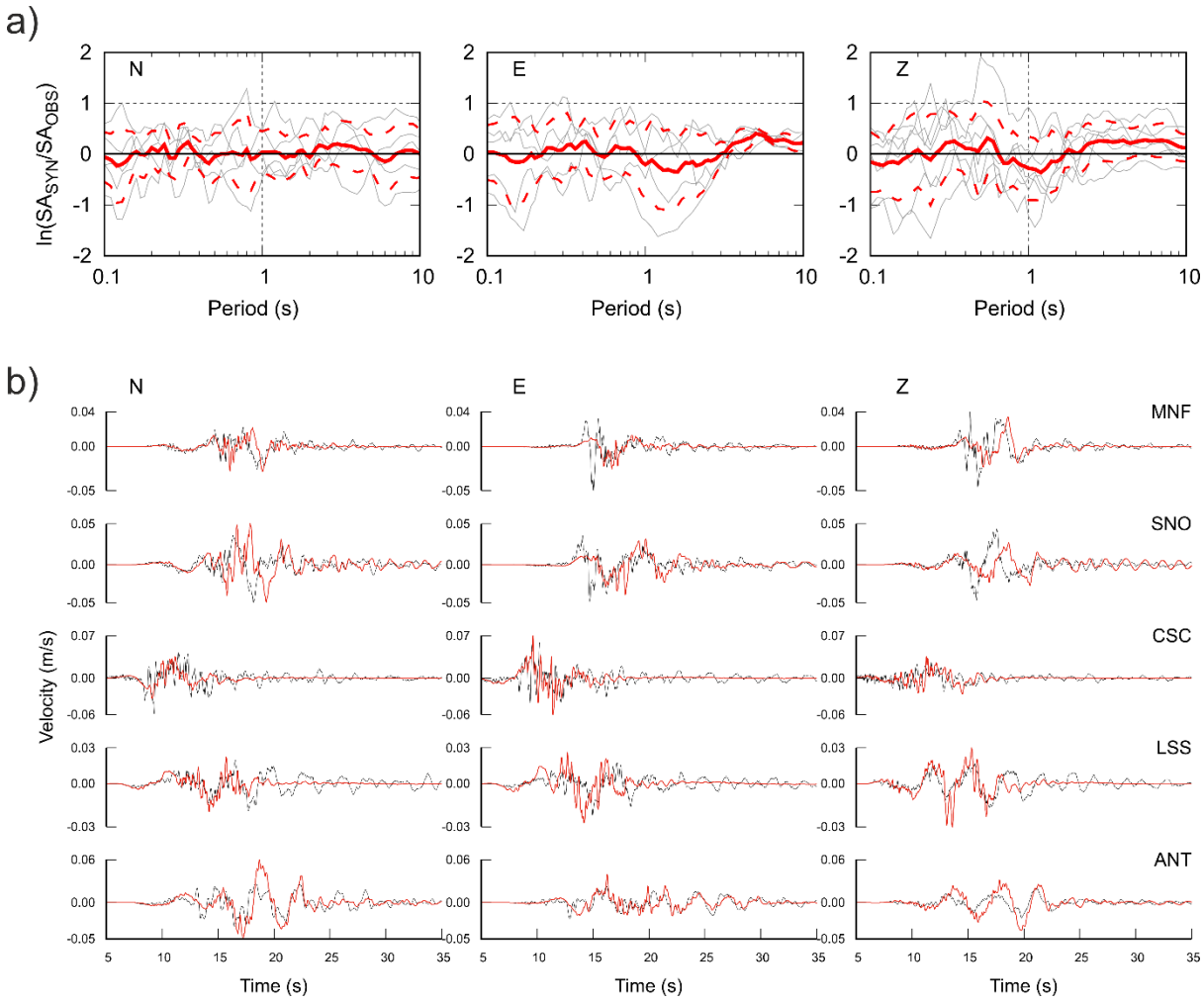

Figure 3.3: Comparison of ground motions of the optimal HIC model against real data at reference sites. a) SA bias for each component as a function of the period between the observed and synthetic waveforms for the optimal model at the reference stations (gray lines). Red solid and dashed lines represent the mean and standard deviations over the stations. b) Comparison of the observed (black line) and synthetic (red line) velocity waveforms for the optimal model at 5 reference stations.

The σ^2-value representing the mean variability of the SA residuals in Fig. 3.2c shows very low sensitivity to parameter a but a very clear minimum in v_r around 2.5 km/s. The source model with minimal σ^2-value underestimates the observed ground motions due to the too low value of parameter a and thus has a significantly higher B^2-value (0.3786 cf. with 0.2841 of the optimal model). On the other hand, the source model with minimal B^2-value has the σ^2-value only slightly higher than the minimum (0.2543 cf. with 0.2516), thus matching not only the SA averaged over the stations but also suggesting that this optimal model belongs to those with low variability in the SA bias (the yellow region in Fig. 3.2c bottom). The dependence of σ^2 primarily on v_r is related to the rupture directivity effect affecting the variability of ground motions in different azimuths, unlike parameter a that affects all stations equally.

Fig. 3.3a shows the period-dependent component-wise SA bias (Eq. 3.3) for the optimal model for the individual reference stations together with its mean and standard deviation. The mean SA bias is close to zero, showing a generally good fit between the simulations and observations on reference stations. The variability of the SA residuals (gray and red dashed lines in Fig. 3.3a) generally decreases with increasing period, suggesting that the optimal HIC source model well represents the large-scale features. On the other hand, the increase of the variability towards the short periods (i.e., high frequencies) demonstrates the increasing small-scale complexity in the path effects even at the reference stations (3D structures like sedimentary basins, topography, scattering in fractured rocks). The high-frequency ground motions are generally more challenging to capture, although the stations are reference rock sites.

Fig. 3.3b shows a relatively good fit between the observed and simulated velocity waveforms for the optimal model at 5 reference stations. We see a relatively good low-frequency waveform fit for stations LSS and CSC located perpendicularly to the rupture propagation. For station ANT oriented to the south, we observe long-period pulses resulting from the directivity both in the synthetics and observations. The waveforms at two stations towards the north, MNF and SNO, show similar pulses but with a temporal delay in the synthetics (see pulses in the later times at N and Z components). The latter can be assigned to different rupture velocities in the northern and southern parts of the rupture, as also indicated by the dynamic source inversion (Gallovič et al., 2019), whereas modeled with a constant value in our present simplified simulations.

Ground shaking prediction on rock sites

We simulate the ground motions for the optimal model at a regular grid of 400 virtual stations. Fig. 3.4a shows the geometric mean of horizontal components of SAs at three frequencies, 0.5, 3, and 10 Hz (periods 2 s, 0.33, and 0.1), as a function of azimuth and Joyner-Boore distance (pinkish dots). Fig. 3.4a also includes observations at reference stations (triangles), the remaining (non-reference) stations (circles), and synthetic values for the optimal model at all stations (red triangles and circles). The azimuthal dependence exhibits four lobes at approximately 90-degree intervals resulting from the source radiation pattern (note that this concerns mainly the more distant stations). This is consistent with the empirical observations of Kotha et al. (2019), who evidenced for normal faulting that ground motion residuals show a four-lobed azimuthal trend, with minima in the strike-parallel (azimuths 155° and -25°) and strike-perpendicular directions (azimuths 65° and -115°), and maxima in between. We note that this pattern would be even stronger if we neglected the random variations of the subsource focal mechanisms in the composite part.

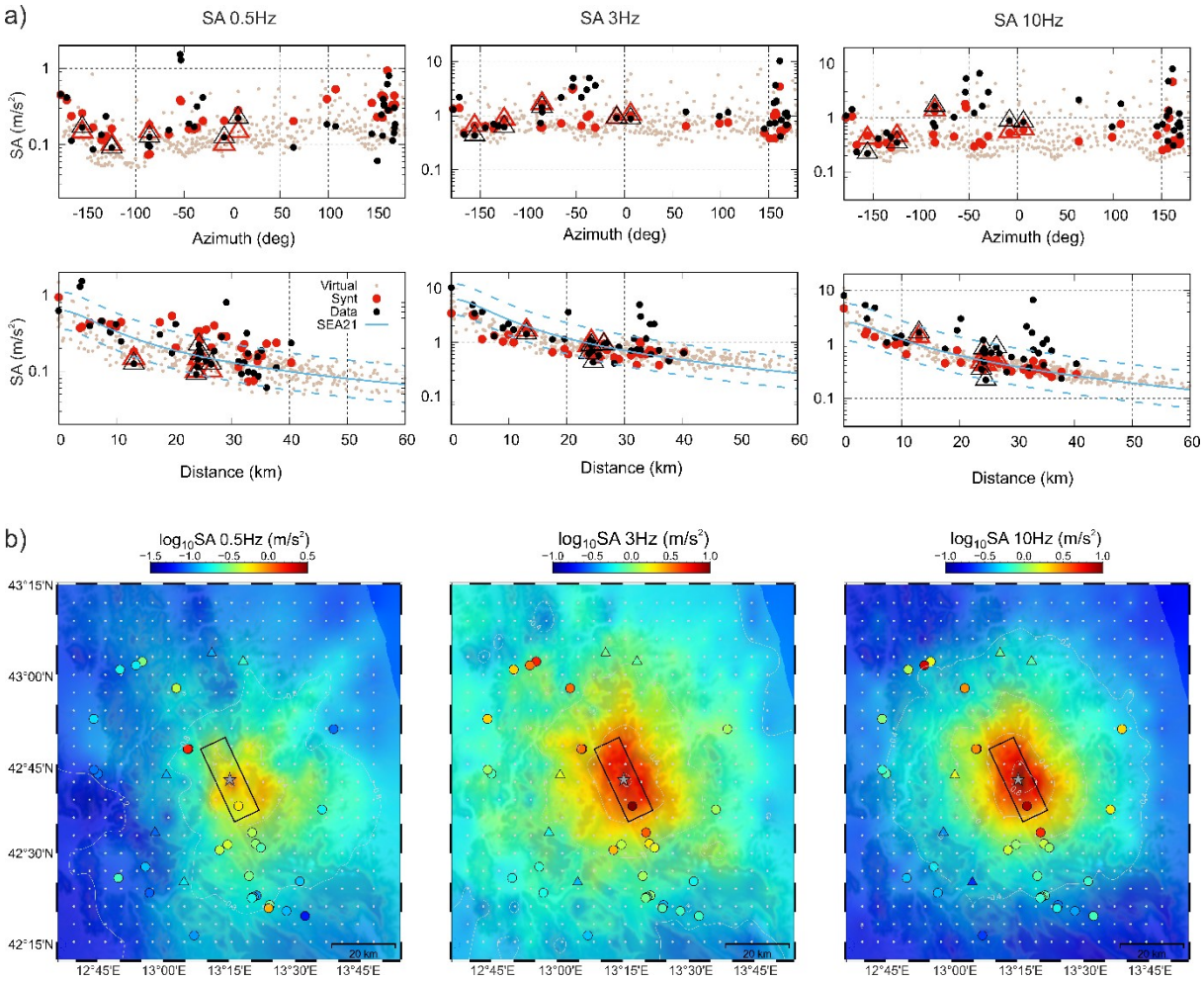

Figure 3.4: Shaking distribution expressed by the geometric mean of horizontal components of simulated SAs at 0.5, 3, and 10 Hz for rock crustal models. a) Geometric mean of horizontal SAs as a function of azimuth (top) and distance from the source (bottom). Black triangles and dots represent the peak values observed at reference and non-reference stations, respectively. Red triangles and dots show the corresponding synthetic values, while pinkish dots correspond to the simulations on a grid of 400 virtual stations around the fault (see Fig. 3.1a). The blue curves show the median and standard deviations of predictions by the ground motion model of Sgobba et al. (2021, SEA21). b) The SA maps are interpolated from the predictions at virtual stations (pink points). Black rectangle shows the fault, star depicts the epicenter. Triangles and circles show corresponding color-coded observed values at the real reference and non-reference stations, respectively. The simulated SAs agree with the observations at the reference sites. The simulated SAs are underestimated at higher frequencies (3 and 10 Hz) at non-reference stations due to the unaccounted site effects.

In the distance plots of Fig. 3.4a, the synthetics and observations are supplemented by the prediction of the regional nonergodic ground motion model SEA21. The agreement between reference station observations, synthetics, and GMM is very good at all periods, including the variability. Moreover, the agreement is also good for most non-reference stations at the lowest frequencies (0.5 Hz), as the site effects are negligible. With decreasing periods, the variability of the simulations decreases when compared to GMM. This is because our 1D crustal models are too simple to account for complex 3D small-scale path and site effects on the variability (Pitarka et al., 2021b). The simulations agree with the median prediction of GMM at 10 Hz. At 3 Hz, the simulations underestimate SEA21 at distances shorter than 30 km while showing a good fit at larger distances. This

may indicate inaccuracies in the GMM model in the near-source region because it is mainly constrained by observations at larger distances where the recordings are more abundant.

Fig. 3.4b presents the map view of the simulated geometric mean of horizontal components of SAs at the same frequencies (i.e., the spatial distribution of shaking at bedrock) interpolated from the synthetics at the virtual stations. The maps illustrate the near-source features caused by the rupture process, as site effects are not included. For example, the presence of a patch of relatively strong shaking near the epicenter reflects the slip asperity (Fig. 3.2b). The spatial pattern also agrees with the observed directivity at the Amatrice town to the S-SE edge of the fault projection (Fig. 3.4b on the left) where low-frequency pulses (about 0.5 Hz) at the AMT station have been recorded. This effect is indeed well captured by the low-frequency shaking that includes seismic wave coherency in the synthetics. At higher frequencies (3 and 10 Hz, Fig. 3.4b), an asymmetric distribution of the shaking can be noticed, with slightly larger values toward the N-NE region (Adriatic coast), perhaps due to the footwall (i.e., radiation pattern) effect.

Fig. 3.4b also includes the observed values at all (reference and non-reference) stations. The predicted and simulated values at reference stations agree relatively well for all frequencies, while the simulations substantially underestimate the observed values at non-reference sites (also evidenced in Fig. 3.4a). Therefore, to provide more realistic estimates, the synthetic ground motions need to be supplemented by site contribution at non-reference stations.

Ground shaking at non-reference sites

To explore the performance of the broadband simulations and site effect modeling at the non-reference stations, we apply the empirical site corrections δS2S of SEA24, introduced above, to the synthetics calculated for rock conditions, where available. We apply both the mean site amplifications δS2S, as well as the δS2S corrected for the event-specific effects δW_0, with reference to the Amatrice earthquake (Colavitti et al., 2022; Sgobba et al., 2024). The latter represents the leftover residuals between the recordings of the Amatrice earthquake and the nonergodic ground motion model containing the systematic source, path, and site effects. We include the event-specific residuals δW_0 (i.e. Amatrice specific contribution) because the local amplifications may not be completely separated from the source and path effects, which is often expressed as increased variability of the empirical site response terms. Indeed, the site-average response (i.e., the δS2S calculated as the arithmetic mean from many events) can differ from the event-specific amplifications due to the source-site configuration, station topographical conditions or other site and propagation effects (Pilz et al., 2022; Lanzano et al., 2017).

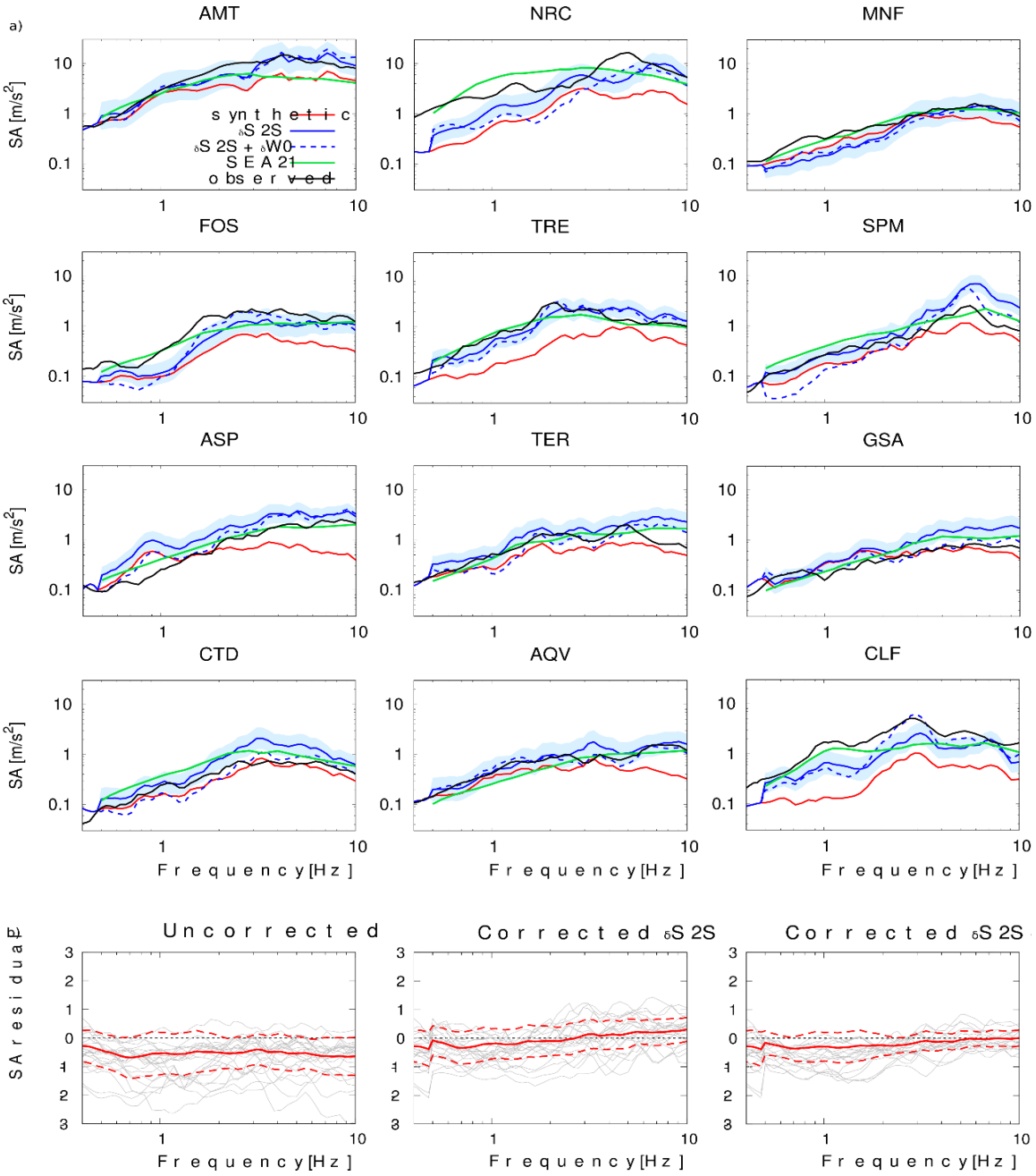

Figure 3.5: a) Examples of site-corrected SAs at (non-)reference stations (see also Fig. S3.5 for the full set). Black curves show the observed SAs, red lines correspond to the SAs simulated using the 1D rock site crustal models. Blue solid lines are synthetic SAs after applying mean site-correction δS2S and blue shaded region marks their uncertainty in terms of ±1 standard deviation. Blue dashed curves show site-corrected SAs assuming both mean site-term δS2S and Amatrice-specific residual δW_0. Green curves show the GMM prediction by Sgobba et al. (2021) including source, path and site terms. b) SA bias of geometric mean of horizontal components for all stations (including the non-reference stations) between observations and simulations on rock site without empirical site corrections (left); simulations corrected using the mean site-specific terms (δS2S) (center); simulations corrected using the site-specific (δS2S) and residual (δW0) terms (right). Gray curves show the SA residuals for each station, red solid and dashed lines show the mean and standard deviations, respectively.

The resulting SAs are compared in Fig. 3.5a for a subset of 12 stations characterized by different source-to-site azimuths, including two near-source stations (AMT, NRC) and one reference rock site (MNF) for comparison (see Fig. S3.4 of the Supplement for the

remaining stations). We also show the prediction by SEA21 including all source, site, and path-specific terms. Overall, the comparison between observed, corrected synthetic SAs, and SEA21 prediction is good.

At AMT, the corrected SAs agree well with observations, while SEA21 underestimates them at higher frequencies. On the contrary, at NRC located in a large basin (Luzi et al., 2019), the corrections amplify the synthetic spectrum over the whole frequency range but do not fully explain the observed data at frequencies below 2 Hz and the prominent peak at 5 Hz, perhaps due to a missing localized slip patch and/or complex interactions between source and basin. At reference site MNF, the simulated, corrected, SEA21, and observations agree well, confirming the consistency of the empirical and numerical models. The SAs for stations SPM and TRE, located west of the fault, are strongly affected by site amplifications and agree with observations only when the mean and Amatrice-specific site corrections are included, except for the 6 Hz peak at station SPM which, although present in the data, is overestimated in the synthetics by both types of corrections. For most stations (FOS, ASP, TER, AQV), the site correction is significant at frequencies above 2 Hz. The discrepancies at lower frequencies (see stations FOS, ASP) may indicate an improper crustal model used for the wave propagation simulation.

For most cases shown in Fig. 3.5a, the synthetic predictions corrected for the average site effect ($\delta S2S$) are very close to that obtained by applying the Amatrice-specific correction ($\delta S2S+\delta W_0$). On the other hand, in some cases, the specific corrections show (frequency-dependent) discrepancies from the average. For instance, at station GSA located on a relief, where the topography affects the site response depending on the source-to-site path, we see that the synthetics with Amatrice-specific site corrections are much closer to the observation. Similarly, the CTD station shows local effects better captured by the $\delta S2S+\delta W_0$ correction, most likely due to peculiar installation effects and soil-structure interaction (the station is located inside an electrical cabin). At AQV situated in the valley, the site-corrected spectrum is very close except for the peak at ~3 Hz generated by the rock-site simulations but then over-amplified by the mean site correction. At the CLF station located in a basin, the SAs with mean site correction $\delta S2S$ underestimate the observations in the whole frequency range. Contrarily, the $\delta S2S+\delta W_0$ site correction reproduces the observed basin resonances better for frequencies >1 Hz, whereas the peak at 1 Hz is underestimated. In this case, complex valley edge effects may occur, whereby valley resonances are amplified or not depending on the portion of the basin traversed by the seismic waves. This effect is probably caused by an impedance and velocity contrast between the soft sedimentary coverage of the basin and the underlying bedrock, as found by borehole investigations (Pischiutta et al., 2016). These 2D/3D effects and resonances at low frequencies could also be responsible for surface wave generation in the coda portion of the recordings. However, such an effect cannot be captured by the specific amplification response $\delta S2S+\delta W_0$, which is instead calculated by the empirical site curve only on the S-phase of the signal (Sgobba et al., 2021), thus not taking into account the later arriving surface waves.

For the sake of completeness, Fig. 3.5b shows the bias calculated for the geometric mean of the horizontal SAs for all stations using the original simulations on rock, SAs corrected by site-specific term δS2S, and SAs corrected by the Amatrice-specific amplification using both δS2S and δW_0 terms. The underestimation by the rock site simulations over all frequencies is improved by applying the δS2S corrections. We see a weak overestimation of the observations only at the highest frequencies. The SA bias variability decreases when applying the δS2S corrections, and moreover, when including the Amatrice-specific correction δW_0, we observe a very good fit to data and a very low variability for frequencies above 2 Hz. This confirms that the residual term δW_0 can be a good proxy for the source-specific site amplification at higher frequencies unaccounted for in the simulations.

3.5. Discussion and Conclusions

We have validated the kinematic HIC broadband source model of the Mw6.2 Amatrice earthquake by fitting the observed spectral accelerations between 0-10 Hz at reference rock stations (i.e., with weak or no site effects). We found the optimal ranges for rupture velocity and parameter *a* controlling the high-frequency radiation. However, these parameters show a trade-off indicating that the observed ground motions are constrained primarily by the event corner frequency aggregating the two parameters. We inspected the synthetic ground motions generated by the optimal HIC model and compared them with predictions of the regional nonergodic model by Sgobba et al. (2021). For the reference rock sites, we see a good agreement with observations and empirical model in the far field, showing the potential of the simulations to replace and/or integrate the uneven or missing near-source observations.

The presented validation is an important step before the construction of ground shaking scenarios because it may reveal the important ingredients for reproducing with greater accuracy the spatial anisotropy of the near-source ground motions related not only to the rupture mechanisms. For example, to generate realistic Mw6.2 rupture scenarios on the Amatrice fault by the HIC method in Čejka et al. (2024b), we have adopted the same fault orientation, the two regional crustal models and the cross-over frequency range and varied the fault size, slip distribution, nucleation position, rupture velocity v_r and parameter *a*, and explored the effects of the individual source parameters on the ground motion variability.

To improve the modeling at non-reference stations (i.e., stations with significant site effects), we have applied the empirically derived site corrections to the synthetic SAs (simulated for reference rock conditions) for all available stations. We note that the additional source model validation at non-reference sites may unveil any missing features of the source model only after the site correction is applied to the synthetics. The general underestimation observed in the rock-site simulations over all frequencies is improved when applying the empirically derived site corrections, suggesting their ability to capture local features due to topography, installation conditions, impedance contrasts, and effects related to source-site configuration. The remaining deficiencies are likely related to the

very complex local structure (such as basin-edge induced surface waves). They can thus hardly be explained without 3D wave propagation modeling and perfect knowledge of the velocity model. Despite this, when we optimize the kinematic source model on a good set of reference stations, we can provide fast, realistic estimates of ground motions by applying empirical site corrections to the synthetic ground motion spectra calculated in simple crustal models.

The proposed method is an example of how synthetic and empirical site predictions can be combined. This is a key aspect because, in practical use, simulations must be adjusted to consider site effects, which are one of the primary contributors to ground shaking variability, especially in areas with complex geomorphology. More generally, providing synthetic time series that capture the distinct features of ground motion in a particular region, including proper crustal attenuation and soil response, can be helpful in engineering applications. This is especially useful when selecting near-source records compatible with a given design spectrum, as strong-motion records at short epicentral distances of medium-to-large earthquakes are often scarce. As a result, they can be used as input for dynamic structural analysis in engineering and geotechnical applications, providing valuable insights and contributing to the development of the seismic risk assessment and design scenario tools.

3.6. Supplemental Material

Table S3.1: Site proxies of the reference stations used in this study. The information is taken from the Italian Accelerometric Archive ITACA (https://itaca.mi.ingv.it). The geological description is inferred from the geological map at different scales. VS30 may be estimated from measured (Meas) S-wave profile or from Topography (Topo). TOP is the topographic class in accordance with the Italian seismic code (NTC2019) – T1: Flat surface, isolated slopes and cliffs with average slope angle $i \leq 15°$; T2: Slopes with average slope angle $i > 15°$; T3: Relief with ridge width much smaller than the base and average slope angle $15° < i \leq 30°$; T4: Relief with ridge width much smaller than the base and average slope angle $i > 30°$. HV indicates the spectral ratio between horizontal and vertical components obtained from: (1) Fourier spectra of in situ noise measurements (HVNSR); (2) 5% damped elastic response spectra (HVRS). HV type indicates the shapes of the HV curves - P: peaked; F: Flat; BB: Broad band. Final score is the RRIM score (ranging from 0 – 8) reported by Lanzano et al. (2022).

NET CODE	STA CODE	GEO Scale	GEO Description	VS30 [m/s]	VS30 method	TOP	HV	HV type	Final score
IT	ANT	5000	Dolostone	912	Meas	T1	HVNSR	P	4.86
IT	CSC	10000	Stone	698	Meas	T4	HVNSR	F	4.98
IT	LSS	10000	Limestones	1091	Meas	T2	HVNSR	F	6.48
IT	MNF	10000	Limestones	1060	Meas	T2	HVNSR	F	6.96
IT	SNO	10000	Eluvial-colluvial deposits	429	Topo	T3	HVNSR	F	5
IT	RM33	100000	Limestones	552	Topo	T3	HVRS	BB	---
IT	PZI1	5000	Carbonate rock	705	Meas	T1	HVNSR	BB	---

Table S3.2: Velocity models of a) Norcia area west of the Sibillini Thrust, and b) Amatrice area east of the Sibillini Thrust (Fig. 3.1a). The models are plotted in Fig. 3.1b.

a) Norcia area

Top depth (km)	Vp(km/s)	Vs(km/s)	Rho(g/cm3)	Qp	Qs
0.00	2.05	1.10	2.94	100	50
0.06	2.79	1.50	2.94	400	200
0.08	3.72	2.00	2.94	400	200
0.40	5.58	3.00	2.94	400	200
1.00	5.70	3.10	2.94	1000	500
2.00	5.76	3.10	2.94	2000	1000
5.00	6.51	3.50	3.15	2000	1000
27.00	7.00	3.80	3.26	2000	1000
42.00	7.80	4.20	3.50	2000	1000

b) Amatrice area

Top depth (km)	Vp(km/s)	Vs(km/s)	Rho(g/cm3)	Qp	Qs
0.00	1.49	0.80	1.90	50	50
0.06	2.23	1.20	1.90	100	100
0.16	3.16	1.70	2.00	100	100
1.00	4.83	2.60	2.84	1000	500
2.00	5.76	3.10	2.94	2000	1000
5.00	6.51	3.50	3.15	2000	1000
27.00	7.00	3.80	3.26	2000	1000
42.00	7.80	4.20	3.50	2000	1000

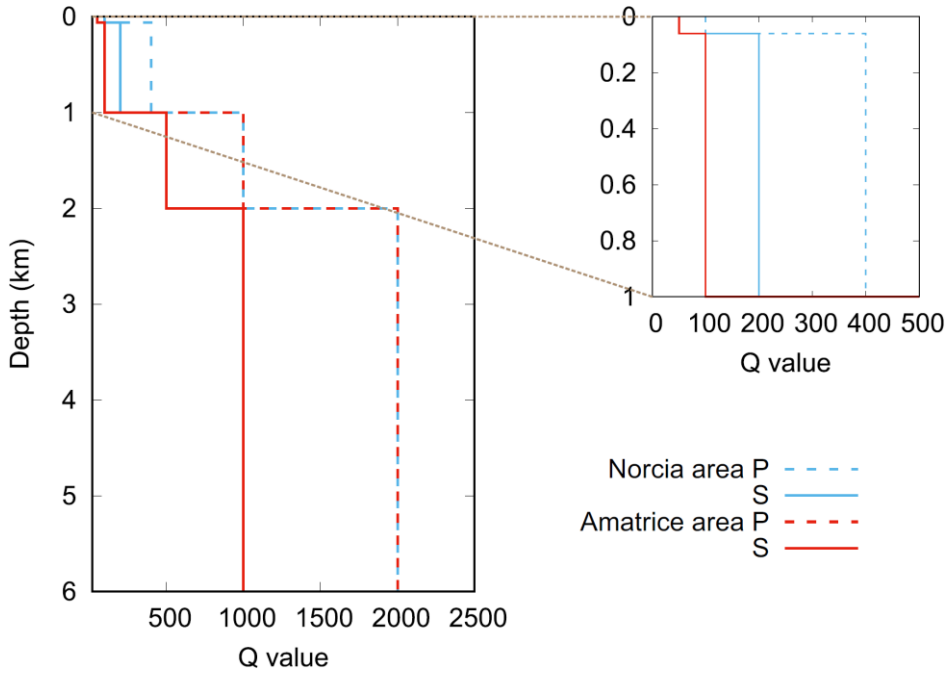

Figure S3.1: Depth dependence of quality factor Q for synthetic Green's function calculation in the Norcia (blue) and Amatrice (red) area, see also Tab. S1. The inset zooms in the uppermost 1 km.

Text S3.1: Effect of the κ parameter

The κ parameter describes the high-frequency decay of the ground motion spectra due to near-surface attenuation (Anderson and Hough, 1984). Here we adopted a value of 0.03 s, which corresponds to the mean value observed over Central Italy stations by Castro et al. (2022). Fig. S3.2 shows how this choice affects the SA bias. When κ is higher (0.06 s), the spectra of the synthetic ground motions decay faster resulting in the negative SA bias at short periods (Fig. S3.2a). On the other hand, when neglecting the high-frequency attenuation completely ($\kappa = 0$ s), the resulting SA bias tends to positive values with decreasing periods as the simulated waveforms are richer in the higher frequency content than the observed ones. We emphasize that the HIC model parameter a affects the level of the source high-frequency radiation, and thus, it may counterbalance the adopted κ value. Nevertheless, the κ parameter is much better estimated from the empirical studies (Castro et al., 2022; Lanzano et al., 2020), and therefore, we have decided to keep κ fixed at its regionally average value and treat parameter a as a free parameter in our study.

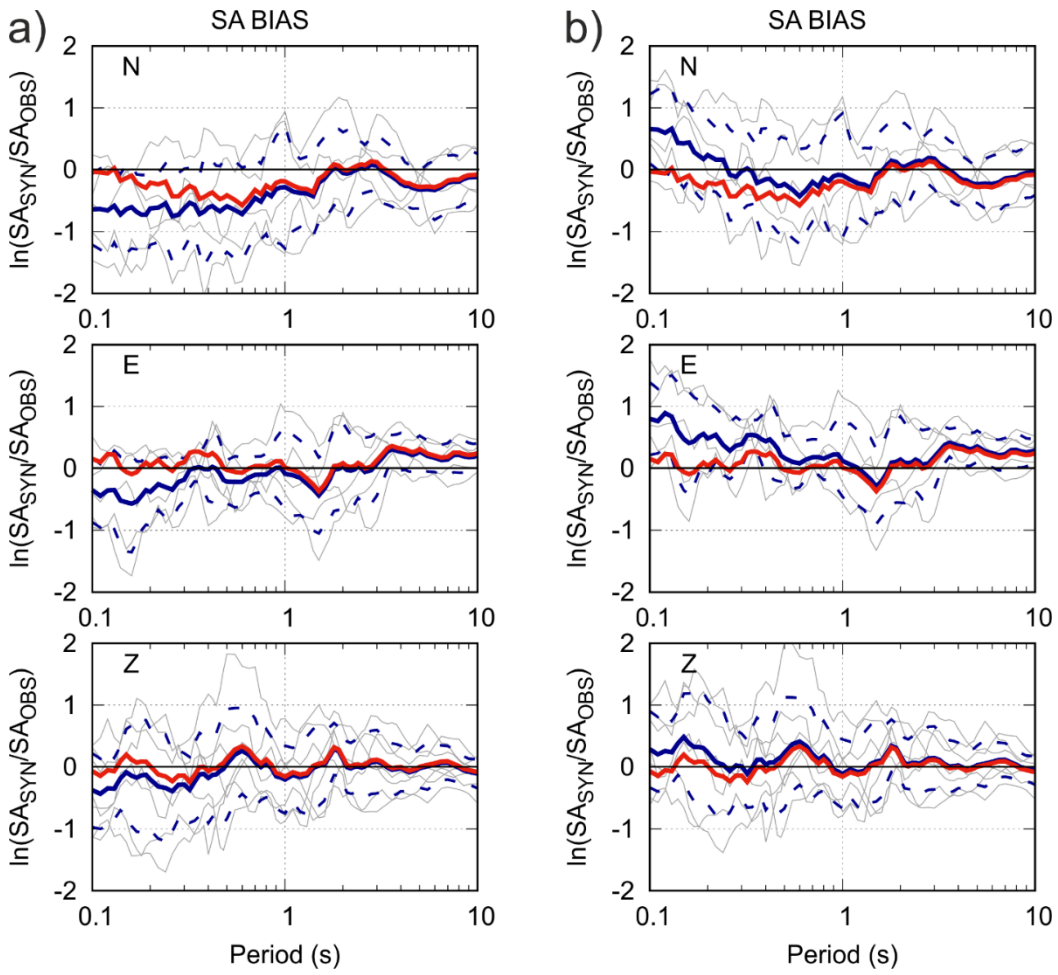

Figure S3.2: SA modeling bias for each component as a function of period between the observed and synthetic waveforms for the optimal model at reference stations (gray lines) considering different values of high-frequency attenuation parameter κ: a) κ = 0.06 s, and b) κ = 0 s. Blue solid and dashed lines represent the mean and standard deviations, respectively. Red lines represent the mean for the optimal model with κ = 0.03 s (Fig. 3.3b in the main text).

Text S3.2: Effect of the cross-over frequency range

One of the parameters affecting the modeling bias is the choice of cross-over frequencies f_1 and f_2 for the HIC model. Their values determine in which frequency range the source directivity of the integral model starts to decrease at f_1 until it diminishes completely at f_2, above which the model is purely composite. In hybrid methods, the cross-over frequency is usually preferred around 1 Hz (Graves and Pitarka, 2010), Here, we adopted values 0.15-0.6 Hz based on our previous HIC applications in Central Italy. To demonstrate how the different frequency ranges affect the modeling results, Fig. S3.3a shows the SA bias for each component when only the composite part is used, i.e., setting $f_1 = f_2 = 0$ Hz. Omitting the integral part results in the negative bias at long periods (mainly at Z component of Fig. S3.3a) that can be explained by synthetics missing directivity pulses observed at these periods (Čejka et al., 2023). Fig. S3.3b shows the spectral bias when selecting larger values of the cross-over frequency: 0.3-1.2 Hz. The positive SA bias in the cross-over range (components N and Z) indicates that the synthetic directivity effect is overestimated. In both cases, it is more difficult to fit the observed data compared to the original cross-over frequency range. This simple test shows the importance of the frequency cross-over parameters for individual applications.

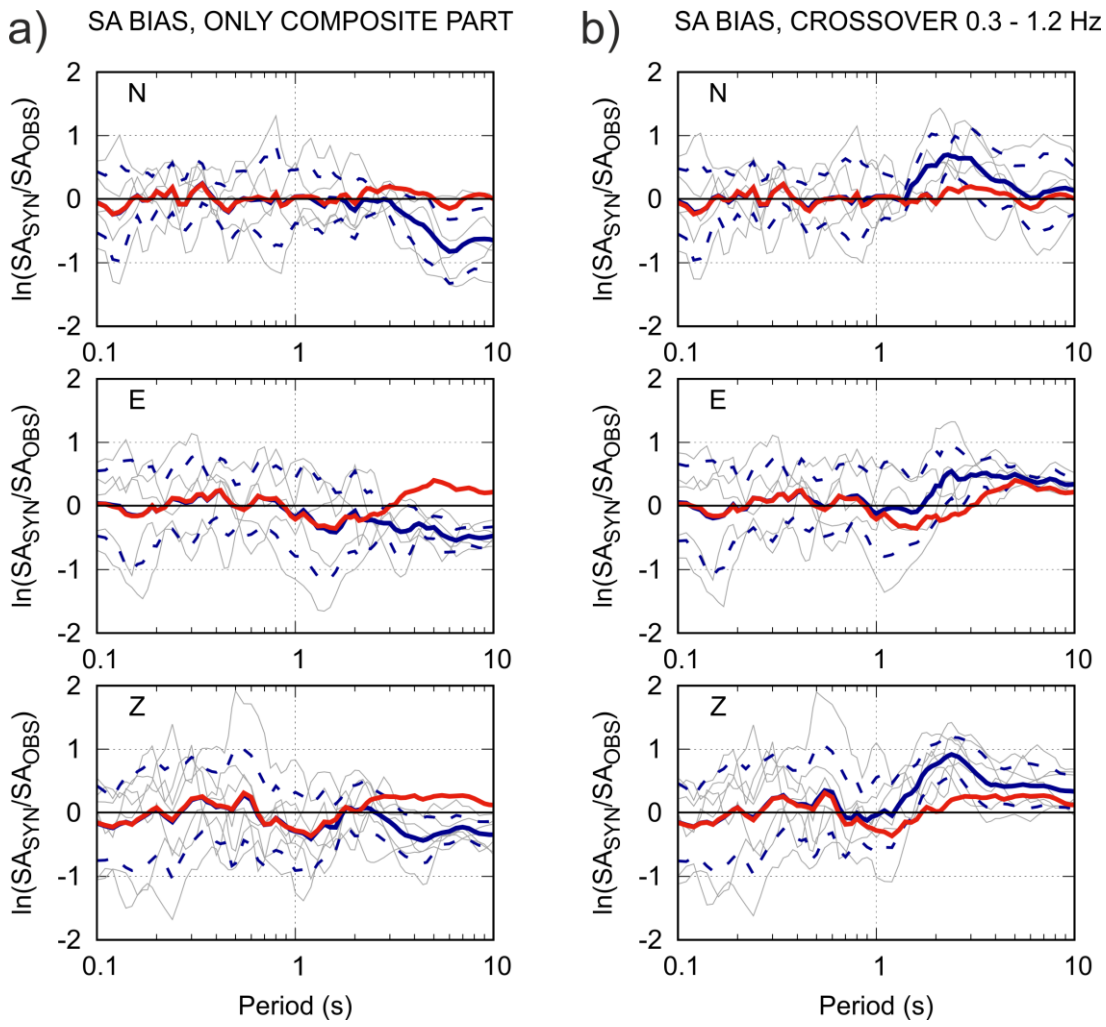

Figure S3.3: SA modeling bias for each component as a function of period between the observed and synthetic waveforms for the optimal model at reference stations (gray lines) considering different cross-over frequencies: a) only composite source modeling is employed, and b) the cross-over frequency range of 0.3-1.2 Hz is considered. The blue solid and dashed lines represent the mean and standard deviations, respectively. Red lines represent the mean for the optimal model with cross-over frequencies between 0.15-0.6 Hz (Fig. 3.2c in the main text).

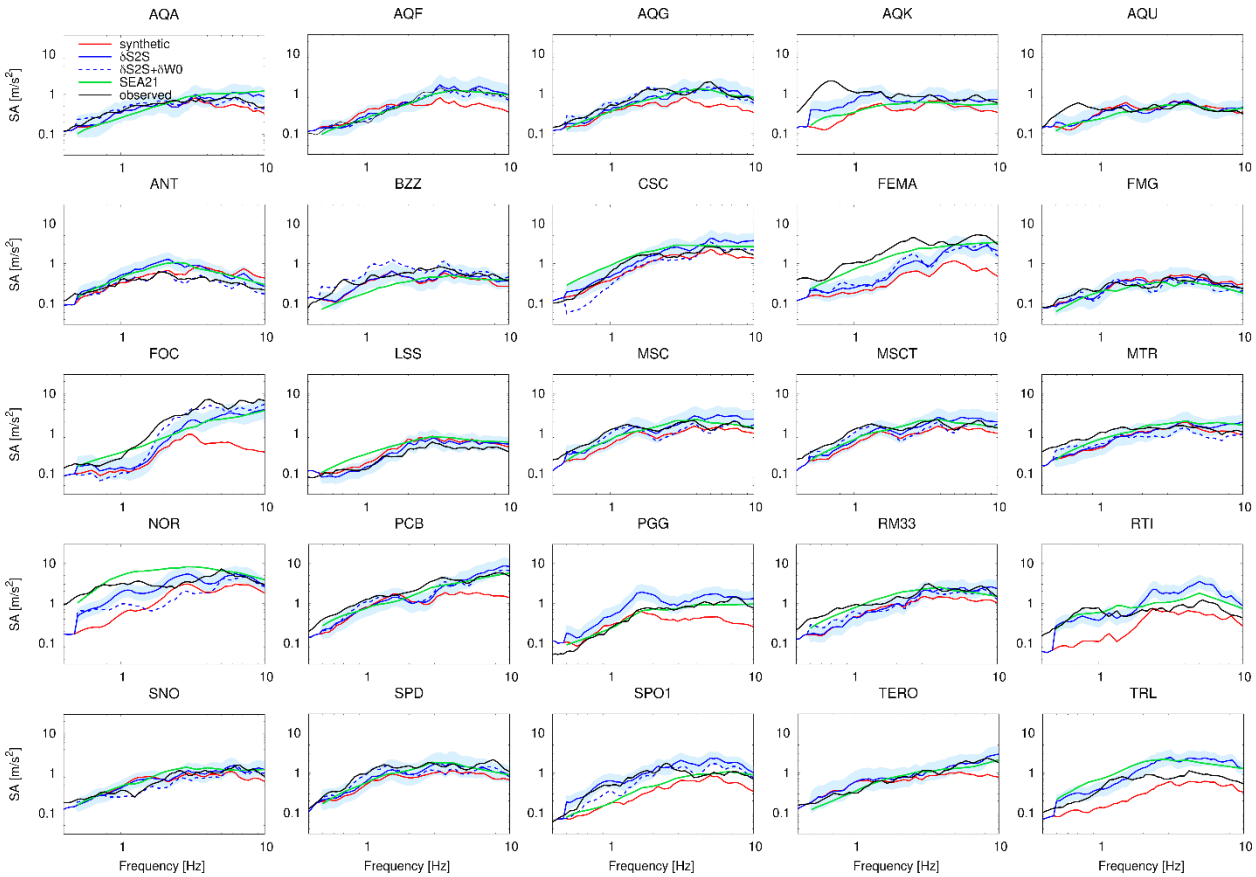

Figure S3.4: Site-corrected SAs at 25 stations. Black curves show the observed SAs. Red lines correspond to the SA simulated for the 1D rock site crustal models. Blue line is the synthetic SA corrected by the mean correction δS2S and blue shaded region marks its uncertainty in terms of ±1 standard deviation. Blue dashed line shows site-corrected spectra assuming both site term δS2S and residual δW0. Green curve shows the GMM prediction by Sgobba et al. (2021, SEA21) for the Amatrice earthquake including the source, site and path terms.

4. Constraining between-event variability of kinematic rupture scenarios by empirical ground-motion model: A case study in Central Italy

This chapter was published as Čejka et al. (2024b) in Bulletin of Seismological Society of America. We made only small notational and stylistic edits.

4.1. Abstract

The region of Central Italy is well known for its moderate to large earthquakes. Events such as Amatrice (Mw6.2, 2016), generated in the shallow extensional tectonic regime, motivate numerical simulations to gain insights into source-related ground motion complexities. We utilize a hybrid integral-composite kinematic rupture model by Gallovič and Brokešová (2007) to predict ground motions for other hypothetical Amatrice fault rupture scenarios (scenario events). The synthetic seismograms are computed in 1D crustal velocity models, including region-specific 1D profiles for selected stations up to 10 Hz. We create more than ten thousand rupture scenarios by varying source parameters. The resulting distributions of synthetic spectral accelerations at periods 0.2-2 s agree with the empirical nonergodic ground motion model of Sgobba et al. (2021) for Central Italy in terms of the mean and total variability. However, statistical mixed-effect analysis of the residuals indicates that the between-event variability of the scenarios exceeds the empirical one significantly. We quantify the role of source model parameters in the modeling and demonstrate the pivotal role of the so-called stress parameter that controls high-frequency radiation. We propose restricting the scenario variability to keep the between-event variability within the empirical value. The presented validation of the scenario variability can be generally utilized in scenario modeling for more realistic physics-based seismic hazard assessment.

4.2. Introduction

Characterization of ground motions, including their uncertainty, is one of the main ingredients in seismic hazard assessment, especially for large human-built structures such as power plants, infrastructure, or buildings in urban areas. Current approaches are based mainly on empirical ground motion models (GMM) determined by the statistical processing of earthquake recordings. GMMs describe ground shaking as a function of source parameters, source-to-site path, and site conditions. The predictive capabilities of such models have improved in recent years due to the increasing availability of seismic records, allowing GMMs to be regionalized by distinguishing source regions, geological domains, and/or specific soil conditions. Moreover, the use of advanced statistical techniques, such as the linear mixed-effects regression (Stafford, 2014, Bates et al., 2015), made it possible to handle the variability better and to calibrate a new generation of partially or totally nonergodic GMMs (Abrahamson et al., 2019; Kotha et al., 2016; Baltay et al., 2017; Rodriguez-Marek et al., 2013; Lin et al., 2011; Anderson and Brune, 1999; etc.). They represent a powerful tool to predict ground motions in moderate and high seismicity areas, where the abundance of data, especially in far-field regions, allows the models to be better constrained. Contrarily, GMMs are less resolved at near-source distances and for larger events due to their rare occurrence and the consequent paucity of recordings, even in well-instrumented regions.

This shortage of seismic records can be remedied by physics-based ground motion simulations, which are promising to fill the observational gaps (Ameri et al., 2012; Bradley et al., 2017; Paolucci et al., 2021). For example, the so-called hybrid simulations are employed frequently due to their efficiency in a broad frequency range (Mai and Beroza, 2003; Gallovič and Brokešová, 2007; Graves and Pitarka, 2010). They can predict ground motions for various rupture scenarios of hypothetical events in a particular region. In the case of scenario rupture modeling, the synthetic ground motions are usually assessed against the empirical GMMs. We point out that the validation of ground motion scenario modeling is still an open issue despite being a critical prerequisite to engineering applications. For example, the Broadband Platform (BBP) of the Southern California Earthquake Center (SCEC; Dreger et al. 2015; Goulet et al. 2015) performed various validation tests against both recorded ground motions of individual events and empirical GMMs. Nevertheless, most scenario simulation validations focus only on the median prediction at the current stage. Only a few studies assess the scenario simulations by comparing their ground motion variability with the empirical counterpart (e.g., Ameri et al., 2009; Cultrera et al., 2010; Song, 2016; Lin and Smerzini, 2022). Moreover, the studies are concerned only with total variability.

In the GMM community, it is common to discern two major constituents of variability: between-event (B-E) and within-event (W-E) (Strasser et al., 2009; Al Atik et al., 2010). While the former corresponds to the event-dependent deviation of the ground motion residuals averaged over all stations, the latter reflects the remaining variability over stations for a given event. We stress that the scenario modeling assessment should concern these two ingredients individually because they provide distinct constraints. The B-E residuals are connected only to the mean source characteristics (such as mean stress drop, mean rupture velocity, etc.) that affect all stations equally. The W-E residuals thus comprehend all the individual path effects (e.g., 3D medium, hanging or footwall), site effects, and site-specific source effects such as source directivity, asperity position, etc. Analysis of W-E and B-E variability from the scenario simulations poses different numerical/computational challenges. While the W-E variability can be studied using a few rupture scenarios with complex 3D source models and 3D wave propagation (e.g., Aochi and Douglas, 2006; Withers et al., 2018; Dujardin et al., 2018), the B-E variability assessment requires many rupture scenarios with various mean characteristics and is rarely studied. Recently, Parker et al. (2023) analyzed the B-E variability from their rupture scenarios, showing that the observed one is overestimated, likely due to the considered slip velocities.

We point out that recognizing the two ingredients of the variability in the scenarios enables modelers to bound any unconstrained free modeling source parameters unbiasedly. In particular, the so-called stress parameter describing high-frequency radiation is known to affect ground motions dominantly (Drouet and Cotton, 2015). Yet, it is often considered constant, leading to underestimating the B-E ground motion variability of the scenarios (Pacor et al., 2016; Lee et al., 2020; Douglas and Aochi, 2016). Alternatively, the parameter is varied in an *ad-hoc* manner (Crempien and Archuleta,

2017) or based on a theoretical model (Drouet and Cotton, 2015), and then the synthetic B-E standard deviation is compared with the empirical one. This study explores the possibility of restricting the source model parameters, set to rather ad-hoc values, by assessing their effects on the resulting B-E variability of the scenarios.

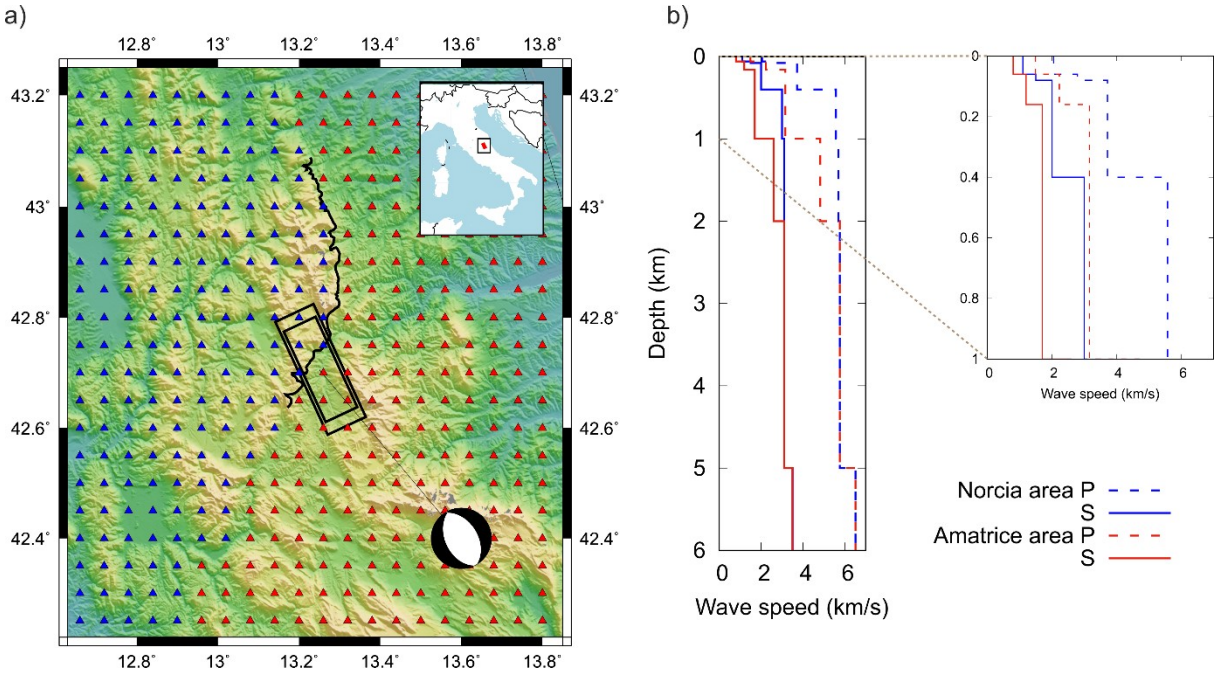

Figure 4.1: Study area and velocity models. (a) Epicentral area of the 2016 Amatrice earthquake with 400 virtual stations (triangles) used for ground motion modeling with variable source scenarios. Black curves correspond to the Sibillini Thrust separating different crustal regimes of the Norcia and Amatrice area. Colors distinguish velocity models used for stations in the Norcia (blue) and Amatrice areas (red). Black rectangles show the fault planes assumed in the scenario modeling and beach ball shows the corresponding mechanism. Map of Italy with the study area depicted by a black rectangle is shown in the inset. (b) Velocity models used to calculate Green's functions for stations in the Norcia (blue) and Amatrice (red) area, with inset zooming in the uppermost 1 km. See also Tab. S1 for the model definitions in numbers.

The target area of our study is the Central Italy region (see Fig. 4.1a), which is well known for its relatively large seismicity and complex tectonic structure. It features mainly seismogenic structures oriented NNW-SSE driven by the extensional tectonic regime of the Central Apennines. The fault segments generally dip SW, extending 20–25 km along the strike and 10–15 km along the dip (Boncio et al., 2004). Many earthquakes struck this area over the last centuries, and a large amount of data was acquired thanks to the increasing number of installed stations in the previous 40 years that were used to derive high-quality non-ergodic regional ground motion model (e.g., Sgobba et al., 2021). The events include the 1979 Mw5.9 Norcia, 1980 Mw6.9 Irpinia, 1984 Mw5.6 Gubbio, 1997 Mw6.0 Umbria-Marche, 2009 Mw6.1 L'Aquila and the 2016-2017 Amatrice-Visso-Norcia sequence, with Norcia being the largest event (Mw6.5).

The objective of the present study is to build a synthetic ground motion dataset in a broad frequency range (0-10 Hz) of kinematic rupture scenarios using the Hybrid Integral-Composite (HIC) model for a hypothetical virtual event. As a model event, we take the 2016 Mw6.2 Amatrice earthquake that has been extensively studied, e.g., with

kinematic modeling (Tinti et al., 2016; Cirella et al., 2018), broadband hybrid methods (Pischiutta et al., 2016; Pischiutta et al., 2021), or dynamic models (Gallovič et al., 2019; Taufiqurrahman et al., 2023). The HIC modeling approach has been validated for several Central Italian events, e.g., the 1980 Mw6.9 Irpinia (Ameri et al., 2011), the 2009 Mw6.3 L'Aquila (Ameri et al., 2012), and in other regions, e.g., the 2011 Mw7.1 Van (Eastern Türkiye; Gallovič et al., 2013), and recently the 2023 Mw7.8 Kahramanmaraş (Eastern Türkiye; Čejka et al., 2023) earthquakes. Recently, Čejka et al. (2024a) validated the HIC model against the 2016 Mw6.2 Amatrice earthquake recordings.

To build different rupture scenarios, we vary the parameters describing the HIC source model and simulate ground motions on a regular grid of receivers. We compare the synthetic response spectra at periods 0.2-2 s with the empirical regional GMM and perform mixed-effect regression on the residuals to discern the B-E and W-E variability. We explore the role of the individual source parameters contributing to the variability, demonstrating the pivotal role of the stress parameter aggregating all the source parameters. The analysis also shows that the synthetic B-E variability overestimates the empirical one. Therefore, we propose to restrict the source parameters to fit the synthetic B-E variability to the empirical value, assuming that i) the empirical B-E variability corresponds to the upper limit of the synthetic B-E variability of the scenarios, and ii) the nonergodic GMM variability constrained mainly by the abundant small- to moderate-sized events is representative of the variability from less frequent larger-magnitude events. Eventually, we discuss the relation between the stress parameters of the restricted scenario database and their estimates from empirical studies, so that the latter can be used to restrict the scenarios apriori in future studies. Our approach thus provides general guidelines for scenario generation to simulate ground motions for various seismo-tectonic regions worldwide where a good GMM is available.

4.3. Methods

Source model

To generate the kinematic rupture scenarios, we employ the Hybrid Integral-Composite (HIC) technique, in which the rupture process is represented by overlapping square subsources randomly distributed on the fault with fractal number-size distribution, where the number of subsources decreases linearly with increasing subsource size (see also Gallovič and Brokešová, 2007). The subsources are characterized by a constant stress-drop scaling, composing a slip distribution with k^{-2} decay at high wavenumbers k. These subsources are treated differently in the high- (above f_1) and low- (up to f_2) frequency ranges, and each of these procedures results in a seismogram, which overlap in the crossover frequency range f_1–f_2. Up to f_2, the *integral* of the representation theorem is calculated, assuming a rupture propagating at a constant rupture velocity. Above f_1, *the composite* approach is used, where the individual subsources are treated as point sources with Brune's source time function. The Brune's function is described by the subsource's seismic moment and corner frequency, assuming constant stress-drop scaling (see further for more details). In addition, we randomly vary the mechanism of the

subsources in the composite part to weaken the radiation pattern at high frequencies. Up to f_1, the resulting seismograms come purely from the integral approach, while above f_2, the seismograms are purely composite. As a result, the directivity of the rupture propagation is well captured at lower frequencies due to the coherent summation of the subfaults' wavefield contributions, while it is suppressed due to the incoherent summation of the subsources' wavefield contributions at high frequencies.

In the frequency crossover section (f_1– f_2), the combination of composite and integral seismograms is treated in the Fourier domain by weighted averaging of the real and imaginary parts of the two seismograms from the two approaches using $\cos^2$ and $\sin^2$ functions (see Fig. 2 in Gallovič and Brokešová, 2007). The crossover frequency range f_1–f_2 is considered to cover the corner frequency of the event, which has been estimated 0.19 Hz in the Amatrice validation paper (Čejka et al., 2024a) or empirical value of 0.35±0.09 Hz from the Brune stress-drop inversion by Morasca et al. (2019). Following

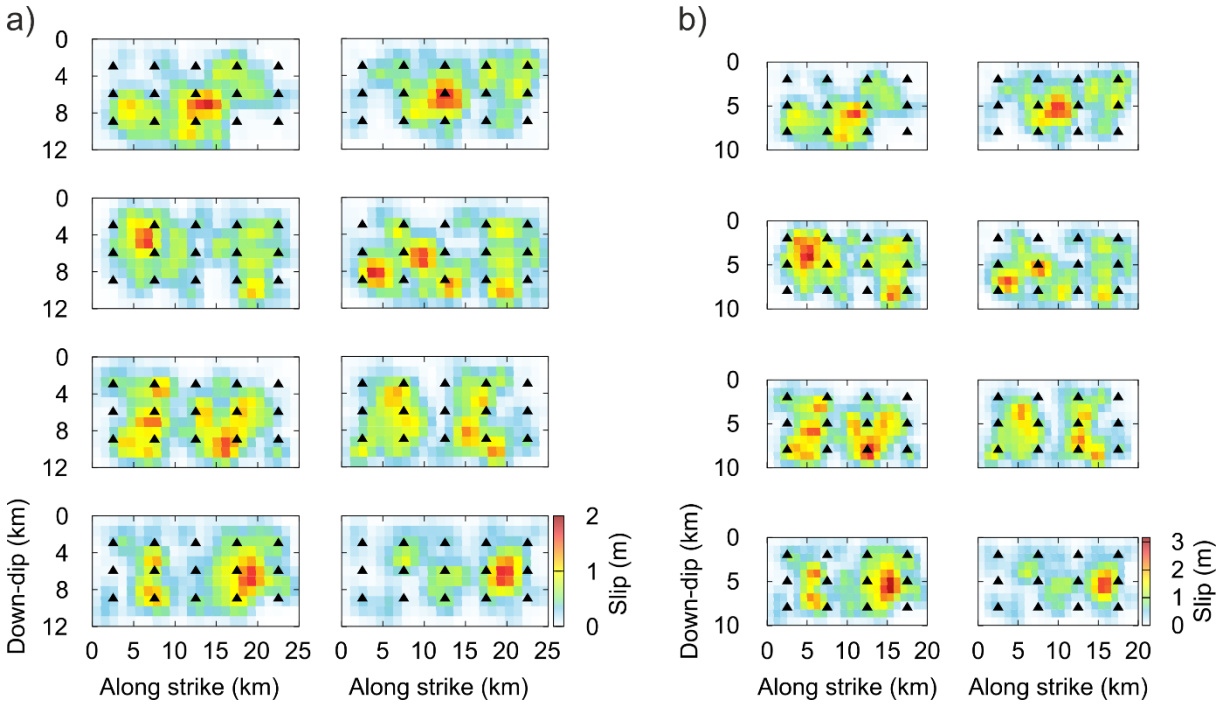

Figure 4.2: Eight slip distributions used in the scenario source modeling obtained by changing the distribution of subsources of the HIC model for fault sizes a) 25x12 km² and b) 20x10 km². The largest subsources are placed deterministically to simulate various positions of asperities, while the others are distributed randomly along the fault. Black triangles mark nucleation points from which the rupture propagates at constant speeds. Note the different color scales in the two panels.

Čejka et al. (2024a) and Ameri et al. (2012), who modeled the Mw6.2 Amatrice and Mw6.3 L'Aquila events in Central Italy, respectively, we set f_1 = 0.15 Hz and f_2 = 0.6 Hz.

In the high-frequency composite part, we assume the omega-square source model, in which the height of the acceleration spectral plateau above $\hat{f}_c$ is equal to $M_0\hat{f}_c^2$ with M_0 and $\hat{f}_c$ being the total scalar seismic moment and the event corner frequency, respectively.

In the HIC model, we generalize the corner frequency with $\hat{f_c} = \frac{a v_r}{L}$, where L is the rupture length, v_r is the rupture velocity, and parameter a is a tuning parameter controlling the strength of the high-frequency radiation. The height of the acceleration spectral plateau is

$$A = M_0 \hat{f_c}^2 = a^2 v_r^2 \frac{M_0}{S}, \tag{4.1}$$

where $S = L^2$. The proportionality constant a is considered to be related to the small-scale rupture evolution and its radiation strength. Because of this, we treat it as a free parameter in our study, although previous studies suggested a value close to 1 (Ameri et al., 2009, Ameri et al., 2011; Gallovič and Brokešová, 2007; etc.). Parameter a can also be interpreted in terms of the so-called stress parameter $\Delta\sigma$. Considering the latter corresponds to the stress drop of a crack model (e.g., Brune, 1970; Kaneko and Shearer, 2015; Wang and Day, 2017; Gallovič and Valentová, 2020), it reads

$$\Delta\sigma = \frac{7}{16}\left(\frac{\hat{f_c}}{k v_s}\right)^3 M_0 \tag{4.2}$$

where v_s is the shear-wave velocity, and k is a parameter depending on the details of the rupture model (heterogeneity of slip, v_r, rise time, etc.). Expressing $\hat{f_c}$ from (4.2), the alternative equation describing the acceleration plateau reads

$$A = M_0 \hat{f_c}^2 = k^2 v_s^2 \left(\frac{16}{7}\right)^{2/3} \Delta\sigma^{2/3} M_0^{1/3} \tag{4.3}$$

Comparing (4.1) and (4.3) suggests that stress parameter $\Delta\sigma$ is a combination of source parameters (rupture velocity v_r, rupture size L, and proportionality constant a) considering a fixed scalar seismic moment. Later, when analyzing our synthetic dataset, we treat $\Delta\sigma$ as a lumped (aggregate) parameter specific for each rupture scenario.

To summarize, the HIC model parameters for fixed M_0 are: i) the fault area, ii) the nucleation point position, iii) the subsources layout (i.e., the slip distribution), iv) the rupture velocity, and v) the subsource corner frequencies (alternatively parameter a).

To generate the synthetic scenarios, we set the strike/dip/rake angles to 155/45/-85 degrees, the latitude and longitude of the fault center to 42.7063° N, 13.2532° E, and the scalar seismic moment to 2.6×10^{18} Nm (Pizzi et al., 2017; Gallovič et al., 2019). We consider two fault dimensions, 25x12 km^2 and 20x10 km^2, representing the sizes of fault segments in Central Italy. We consider 15 and 12 nucleation points distributed regularly on the fault for the larger and smaller fault, respectively (Fig. 4.2). We use eight slip distributions with asperity in the middle, on one or the other side, and both sides, by prescribing the position of the largest subsources deterministically (while the others are placed randomly). We also change the random seed to get variations of these. The resulting slip distributions are shown in Fig. 4.2 for both fault sizes. Note that while the

spatial distributions are the same for the two fault sizes, the slip amplitudes are larger for the smaller fault since the seismic moment is fixed.

The rupture propagates from the prescribed nucleation radially at a constant speed. We vary rupture velocity v_r between 2.0 km/s and 3.4 km/s with a step of 0.2 km/s, covering the standard range of slow to fast ruptures. The last varying parameter is a, assuming values from 0.7 to 1.9 with a step of 0.2. The parameter ranges were chosen rather ad-hoc and are addressed later in the Discussion section, where they are constrained following the B-E variability of the GMM.

Green's functions and crustal velocity models

To calculate the synthetic seismograms, the HIC subsources are convolved with Green's functions according to the representation theorem for a regular grid of 400 virtual stations (Fig. 4.1a). The synthetic Green's functions are precalculated in the 1D velocity models using the Axitra code (Cotton and Coutant, 1997) at frequencies 0.05-10 Hz.

We consider a specific 1D velocity model for each of the two major geological domains divided by the Sibillini Thrust, which is the main structural discontinuity in the area (Fig. 4.1): i) the SSE unit of the Sibillini Thrust, which lies on the Laga formation (Amatrice area) and ii) the carbonate unit to the NNW of the thrust (Norcia area). For the Amatrice area, we supplement the crustal velocity model proposed by Ameri et al. (2012) used in ground motion simulations of the 2009 L'Aquila earthquake by three subsurface low-velocity layers, as considered in kinematic and dynamic source modeling of the Amatrice earthquake by Čejka et al. (2024a) and Gallovič et al. (2023), respectively. For the Norcia area, we adapt the 1D velocity model of Bianchi et al. (2010) to consider the observed wave propagation differences between the two main domains. The topmost kilometer in the Norcia area was obtained by resampling the Vs array profile at stations IT.CSC (Cascia) and IT.LSS (Leonessa). The two final velocity models proposed for the Amatrice and Norcia area are shown in Fig. 4.1b and Tab. S4.1.

The anelastic attenuation is modeled by depth-dependent quality factor Q and high-frequency decay parameter κ. Following Castro et al. (2022), we adopt $\kappa = 0.03$ s as a mean value for all the stations.

Ground motion model

To assess the scenarios, we compare the simulated ground motions with a fully nonergodic ground motion model (GMM) by Sgobba et al. (2021), hereafter named SEA, calibrated explicitly for the region of Central Italy on a dense dataset (about 30,000 waveforms) from 400 stations within 120 km from about 450 earthquakes in the magnitude range of 3.4-6.5. Unlike traditional ergodic models, the SEA is calibrated on reference rock sites (as identified by Lanzano et al., 2020) and then adjusted for systematic effects related to source area, propagation path, and site response, which are specific to the target region.

In our application, the SEA median is adjusted for the location-to-location contribution related to local systematic differences in source features (stress drop, focal depth, etc.) with respect to the average over all source regions in Central Italy (for more details, see Sgobba et al., 2021). On the other hand, we do not introduce any site correction term since the predictions refer to rock conditions. Moreover, we neglect the small contribution of propagation (i.e., the path-to-path terms) because our primary purpose is to reproduce the overall empirical attenuation trend, with no specific focus on the spatial distribution of the shaking. However, the missing corrections to the median are moved to the associated total variability, composed of the B-E and W-E terms (see the Appendix of Sgobba et al., 2021, for more details). As a result, for the present case study, the W-E variability includes the following sources of uncertainty: i) the response of the 36 reference rock sites used for the SEA calibration, ii) the systematic path terms, and iii) the remaining aleatory variability.

The adopted GMM model is defined for the spectral accelerations (SA). Therefore, if available, the simulations are compared to GMM in terms of SA. Nevertheless, the proposed methodology can be applied to other ground-motion measures, such as Fourier Amplitude Spectra (Kotha et al., 2022; Sgobba et al., 2023).

4.4. Results

Comparison with GMM and synthetic ground motion variability

In total, we generate 12096 source models and calculate the broadband seismograms at 400 virtual stations resulting in more than 4.8 million synthetic waveforms simulated up to maximum frequency of 10 Hz. From them, we evaluate the response spectral accelerations (SAs) for periods in the range of 0.2-2 s. Fig. 4.3 compares SAs at four vibration periods (0.2 s, 0.5 s, 1 s, and 2 s) with the predictions of the SEA model for the study region. To facilitate the comparison, we supplement the figure with the mean and standard deviations of binned data. We observe a good agreement with the empirical GMM regarding median and variability at all SA ordinates. We point out that the total variability comprises the within-event (azimuthal changes) and between-event (changes due to the event characteristics) terms. We further scrutinize these two components to avoid misinterpreting the modeling performance.

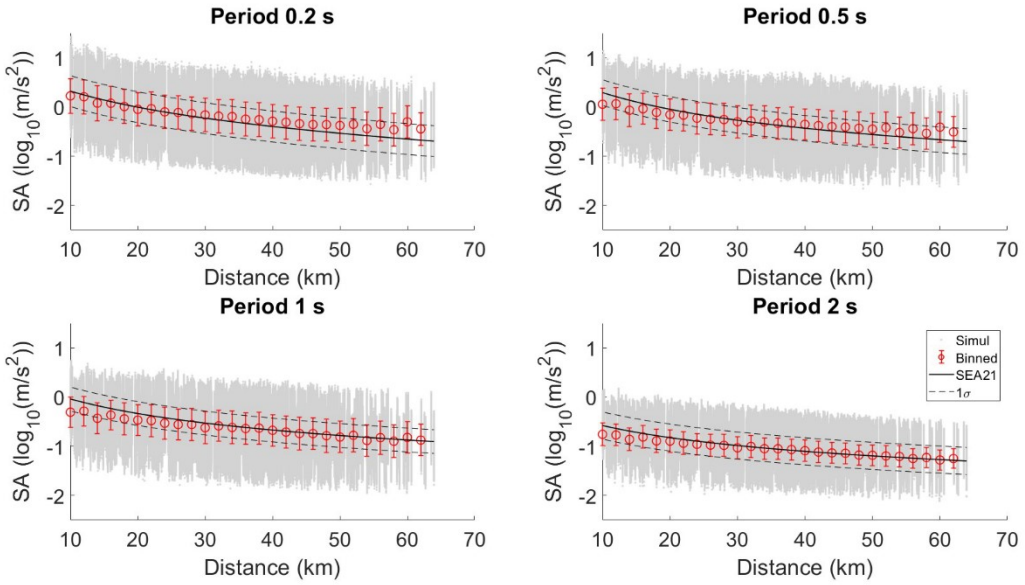

Figure 4.3: Spectral accelerations at four spectral ordinates at virtual receivers of Fig. 4.1 and for all source scenarios, plotted as a function of the Joyner-Boore distance by gray dots. Red circles with error bars are mean values and standard deviations over 2 km bins. Black solid and dashed lines are the GMM mean and uncertainty prediction, respectively (SEA, Sgobba et al., 2021).

To analyze the variability of the scenario simulations (Fig. 4.3), we use mixed-effect regression, which is standardly used in quantifying fixed and random effects of ground motions in the development of empirical GMMs (Bates, 2015). For each spectral period, the residuals R_{ij} between decadic logarithms (log10) of geometric means of the horizontal synthetic SAs, y_{ij}, and the corresponding empirical estimates from the SEA model of Sgobba (2021), y_{ij}^{GMM}, for event scenario *i* at station *j*, defined as $R_{ij} = y_{ij}^{GMM} - y_{ij}$, can be decomposed into

$$R_{ij} = C + \eta_i + \varepsilon_{ij}, \tag{4.4}$$

where C is the mean offset between the GMM and synthetic database, η_i are the between-event (B-E) residuals representing the mean offset over all stations of the *i*-th event scenario, and ε_{ij} are the within-event (W-E) residuals corresponding to the difference of synthetic measurement at observer j from the offset of event *i*. These variability terms are assumed to have independent normal distributions with zero mean and standard deviations denoted τ and ϕ for the B-E and W-E variabilities, respectively. The total standard deviation is then $\sigma = \sqrt{\phi^2 + \tau^2}$. The decomposition is here performed using Python package Statsmodel (www.statsmodels.org, Seabold and Perktold, 2010).

The period dependence of mean offset C, W-E deviation ϕ, B-E deviation τ, and total standard deviation σ is shown in Fig. 4.4a (violet). Tab. 4.1 (first row) lists the values for an example period 0.2 s. The W-E variability is slightly below the empirical value of the SEA model (black) for almost all periods. This underestimation could be ascribed to the fact that the synthetic W-E variability includes only some effects (two area-specific crustal

models, varying nucleation point position, radiation pattern, and directivity effects). In contrast, it lacks others, such as complex path effects due to the 3D velocity structure and topography, the uncertainty of reference rock sites, and remaining aleatory uncertainties, which are present in the real data. Note that the W-E variability is even smaller if only 1 crustal model is used (Fig. S4.1). We conclude that by adopting Green's function modeling with 1D models, we cannot reach the empirical value of the W-E variability in our synthetic dataset.

Explanatory variable	**Offset**	**Log S**	**Log a**	**Log v_r**	**Log Δσ**	τ	ϕ
-	-0.077	-	-	-	-	0.327	0.124
Log S	-9.963	-1.177	-	-	-	0.311	0.124
Log a	0.095	-	1.873	-	-	0.188	0.124
Log v_r	6.814	-	-	2.012	-	0.291	0.124
Log a + Log S + Log v_r	-2.901	-1.177	1.873	2.012	-	0.044	0.124
Log Δσ	0.995	-	-	-	0.644	0.047	0.124
Empirical GMM values (Sgobba et al., 2021)						0.142	0.314

Table 4.1: Parameters of the linear mixed-model regression of the SA residuals for period T = 0.2 s with different explanatory variables and corresponding between-event (τ) and within-event (ϕ) variabilities, see the main text and Eqs. (4.5) and (4.6). The first row corresponds to the regression without explanatory variables as in Eq. (4.4). Empirical values of τ^{GMM} and ϕ^{GMM} are specified in the last row.

The difference between observations and synthetics is larger for the B-E variability and increases towards the lower periods. Indeed, the scenario simulations provide about twice larger B-E standard deviations than the empirical ones for period 0.2 s (τ^{GMM} = 0.142 and τ = 0.327, see Tab. 4.1). We attribute this significant overestimation of the synthetic B-E variability to the exaggerated scenario variability. We point out that it would remain unnoticed without the additional analysis of the components of the variability by the mixed-model statistics. Indeed, the total variability shown in Fig. 4.3 and then in Fig. 4.4a shows a relatively good agreement between the simulations and the GMM for most of the periods because the overestimation of the synthetic B-E variability was compensated by the underestimation of the synthetic W-E variability. In the Discussion, we further scrutinize the effects of HIC source parameters on the synthetic B-E variability and propose restricting scenario parameter ranges to reduce the resulting between-event variability of the scenarios.

4.5. Discussion

Role of source parameters on the ground motion variability

To understand the contributions of the individual HIC parameters to the synthetic B-E variability, we expand the regression of Eq. (č.8), considering various explanatory terms corresponding to different varied parameters. In particular, to explain the variability of SA in Fig. 4.4a, we derive the regression model from the logarithm of the high-frequency theoretical source spectrum of Eq. (4.1),

$$R_{ij} = C' + C_a log a_i + C_{v_r} log v_{r_i} + C_S log S_i + \eta_i' + \varepsilon_{ij}, \quad (4.5)$$

where C' is the new mean offset, C_a, C_{v_r} and C_S are regression coefficients corresponding to the respective explanatory variables indicated by the subscript, and η'_i is the new B-E residual. To isolate the effects of the individual source parameters on the variability, we perform the regressions, taking one explanatory variable at a time and setting the other terms to zero. Fig. 4.4b shows period dependence of the mixed-model regression coefficients and B-E standard deviations (values for the example period 0.2 s are listed in rows 2-4 of Tab. 4.1). Note that we do not discuss the W-E standard deviations because the considered explanatory variables in the mixed-model regression are related exclusively to the mean source properties, and thus the W-E variability remains the same for all cases.

For short periods, the regression coefficients are generally close to their predicted theoretical values, i.e., powers in Eq. (4.1), indicated by arrows on the left side of Fig. 4.4b. The coefficients generally tend to decrease (in absolute values) with increasing periods. Theoretically, the effect of the considered parameters should attain zero for the longest periods as the finite-source model apparently becomes a point source described solely by the (fixed) seismic moment. However, this is not the case because our maximum analyzed period of 2 s is still shorter than the rupture duration.

The B-E variabilities estimated for each explanatory variable, corresponding to the remaining B-E variability after excluding the effect of the respective variable, are shown in Fig. 4.4b (see also Tab. 4.1 for values for the period of 0.2 s). For example, after removing the dependence on the fault size, the remaining B-E variability at period 0.2 s decreases from $\tau = 0.327$ to $\tau_S = 0.311$. The most significant decrease of the B-E standard deviation is attained for parameter a, demonstrating that the greatest portion of our scenario variability comes from the variability in this parameter (also note that $\tau_a = 0.188$ is closer to $\tau^{GMM} = 0.142$ for period 0.2 s). The drop of the synthetic B-E variability is smaller for rupture velocity v_r than for parameter a despite the fact that they both contribute to the variability with the same regression coefficient (approximately 2, in agreement with the second power in the theoretical model of Eq. 4.1), suggesting that parameter a has stronger control on the high-frequency radiation. The effect of the rupture velocity variations on the B-E variability is also weaker because it also translates partially in the W-E variability by altering the directivity effect. We note that the decrease of the B-E variability is controlled not only by the respective regression coefficient but also by the assumed parameter range. In this sense, the result found in this analysis cannot be generalized because it is tied to the construction of our dataset.

Fig. 4.4b ('Combined') and the fifth row of Tab. 4.1 show the regression results after we cleared the effects of all explanatory variables (so only nucleation point and slip distribution are not analyzed). The B-E standard deviation decreases well below the empirical value. Since such remaining variability is relatively small, it suggests that the effect of slip distribution on B-E variability is relatively weak. We note that the nucleation position controlling the directivity effect does not influence the between-scenarios variability because it does not make a repeatable contribution to the ground motion.

Conversely, it controls the spatial variability of the shaking within the same scenario event and is thus attributable to the W-E variability component.

As discussed in the Source model section, the source parameters that control the high-frequency spectrum can be lumped into one stress parameter $\Delta\sigma$ (Eq. 4.3). For each scenario, we determine the amplitude of the high-frequency acceleration source spectrum plateau by summing contributions from the HIC model subsources and calculate $\Delta\sigma$ by Eq. (4.3), assuming $k = 0.37$ (Brune, 1970). The histogram of the stress parameters for all the scenario events is shown in Fig. 4.5, resembling a log-normal distribution.

To analyze the effect of $\Delta\sigma$ on the residuals, we assume another form of the regression equation for the residuals,

$$R_{ij} = C'' + C_{\Delta\sigma} log\Delta\sigma + \eta_i'' + \varepsilon_{ij}, \quad (4.6)$$

where C'' is the mean offset value and $C_{\Delta\sigma}$ is the regression coefficient for $\Delta\sigma$ as the explanatory variable. The results are shown in Fig. 4.4b (in yellow) and listed in Tab. 4.1 for the 0.2 s period. The value of coefficient $C_{\Delta\sigma}$ is 0.64, which is very close to the theoretically derived value ⅔ in Eq. (4.3). As expected, the low value of the remaining B-E standard deviation (like the case of the combined regression) confirms the validity of Eq. (4.3), suggesting that the scenario variability is controlled dominantly by this aggregated parameter. Note also that the mutually canceling effect of the source parameters lumped in the stress parameter makes the B-E standard deviation stable over all periods.

Constraining the source parameters

As we have shown, the B-E variability of our scenario simulations exceeds its empirical counterpart. This calls for restricting the scenario variability by limiting their source parameters for further applications. We propose reducing the number of scenarios by constraining the synthetic B-E standard deviation τ to be close to the empirical value τ^{GMM} of Sgobba et al. (2021). Indeed, this GMM is a regional model describing the source contributions of the seismogenic structures with normal fault mechanisms in Central Italy.

We prescribe the probability density function (PDF) of the synthetic B-E residuals at the lowest considered period of 0.2 s to follow the empirical form, namely normal PDF with zero mean and standard deviation to be equal to the empirical value of the adopted GMM at 0.2 s. We use the rejection method, in which we randomly pick scenarios and accept or reject them stochastically based on their B-E residual. This way, the B-E

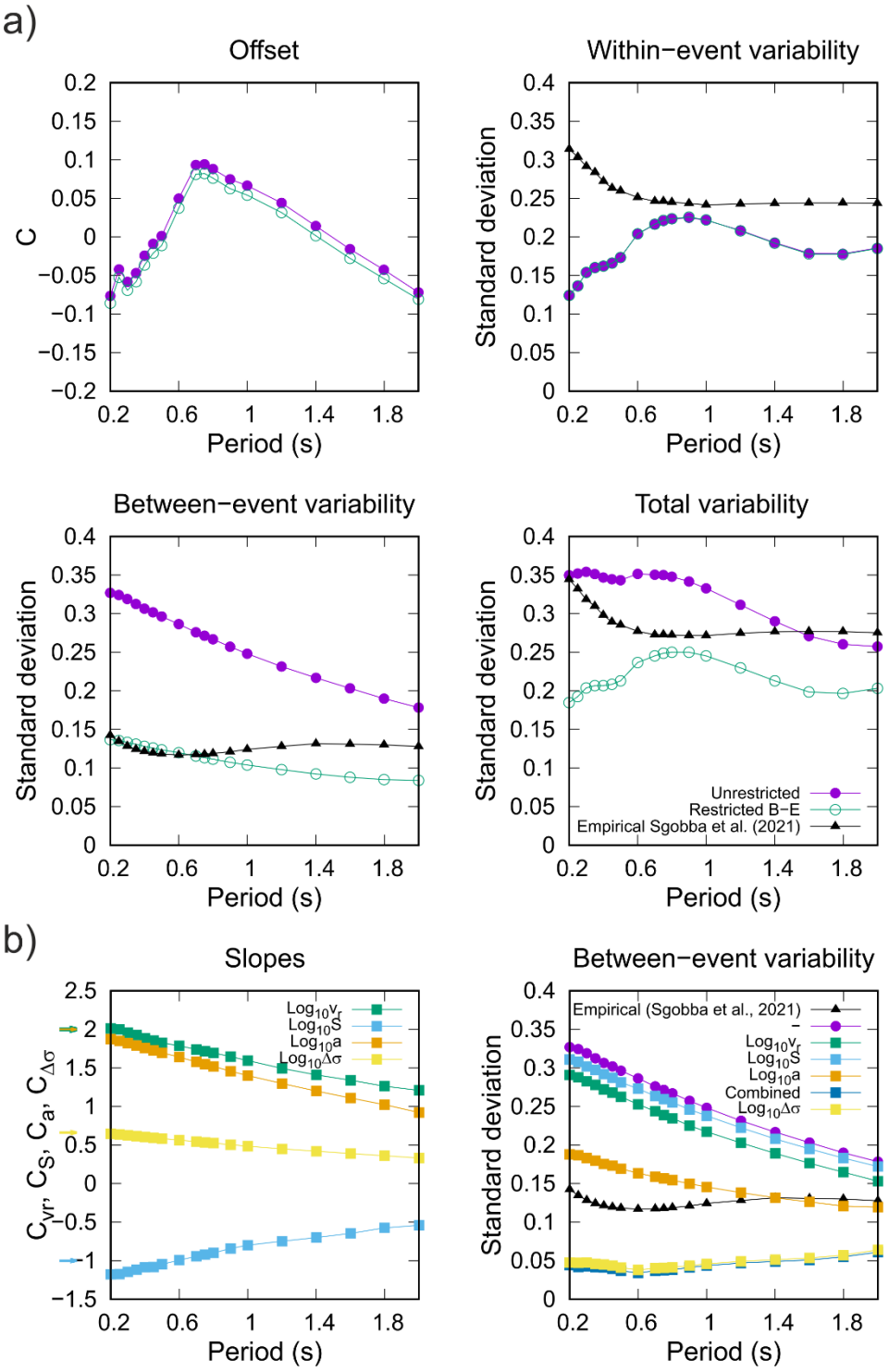

Figure 4.4: Results of the linear mixed model regression of spectral acceleration residuals with respect to SEA GMM at different spectral periods. a) Panels show offset, W-E, B-E, and total variability standard deviation (in log10). Models with unrestricted and restricted B-E residuals (see Section Constraining the source parameters) are distinguished by symbols and colors. Black triangles show the empirical variability. b) Coefficient values for the individual explanatory variables and the respective log10 standard deviation of the B-E variability (see Eqs. (4.5) and (4.6), distinguished by colors (see legend); 'combined' corresponds to the case when all the variables (except for the stress parameter) are considered together. Arrows outside the left graph are theoretical values at high frequencies, see Eqs. (4.1) and (4.3). Purple line is the B-E variability corresponding to the mixed model regression without any explanatory variable Eq. (4.4), same as in panel a. Black line is the empirical B-E variability of the GMM by Sgobba et al. (2021).

residuals of the resulting restricted database have PDF that agrees with the empirical one at 0.2 s; at higher periods, the B-E standard deviations are closer to or below the empirical values (Fig. 4.4a). In the restricted database, we choose to have about one-third of the scenario events (4000 scenarios with potential duplicate entries).

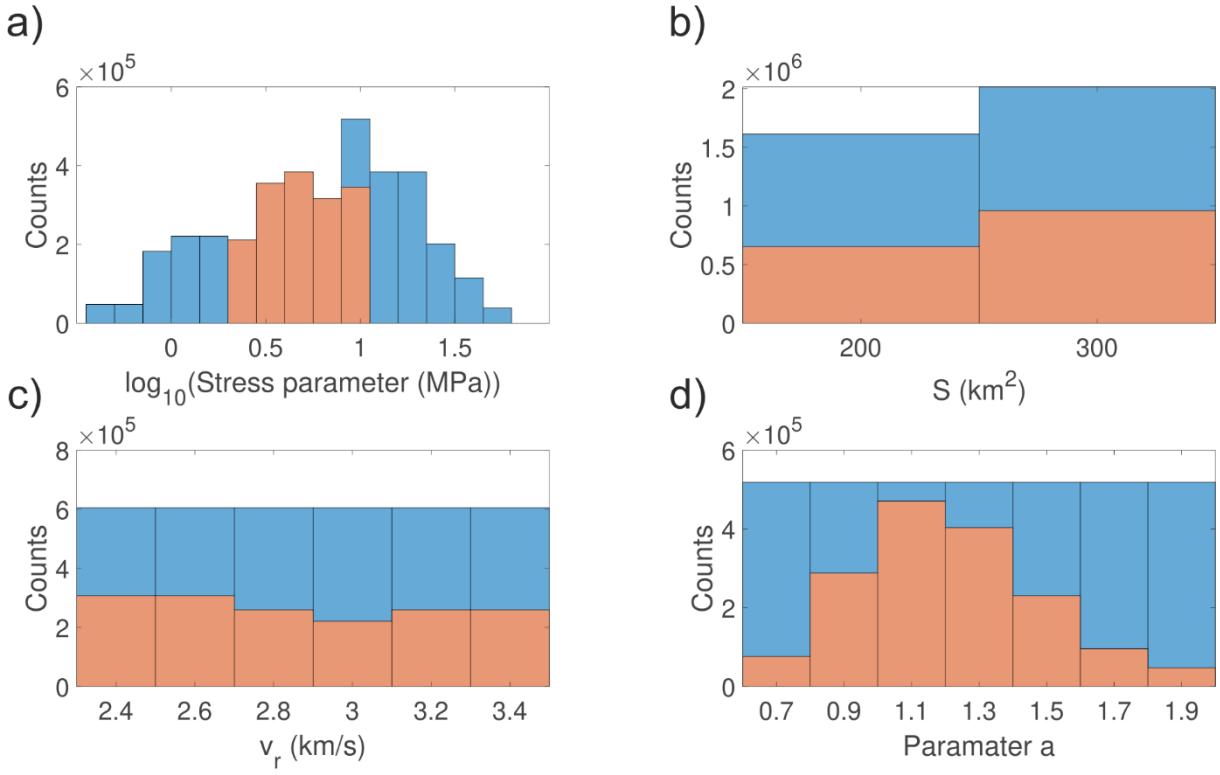

Figure 4.5: Histograms of source model parameters of the scenario database. Blue bars correspond to the unrestricted (full) database, while brown bars are for scenarios restricted to have the B-E residuals in agreement with the adopted GMM.

We explore the properties of the source parameters of the scenarios in the restricted database. The stress parameter has a narrower log-normal distribution with a mean of 4.3 MPa and log10 variability of 0.23 (see Fig. 4.5). The distributions of fault dimension S, rupture velocity v_r, and parameter a are shown in Fig. 4.5. We see that S and v_r retain their distributions from the unrestricted dataset, while parameter a attains a bell shape instead of uniform distribution. This is due to the exclusion of many 'extreme' scenarios, also associated with too high or too low stress parameters.

Concerning the ground-motion variability, the restricted scenario events database does not affect the offset and the W-E standard deviation (Fig. 4.4a, green). The former is because we assumed a zero mean for the prescribed PDF of the B-E residuals; if needed, prescribing a non-zero mean can be used to adjust the offset with respect to the empirical GMM. The combination of the B-E and W-E components also makes the total variability of the restricted dataset slightly smaller than the empirical one (Fig. 4.4a). This is, however, preferable, considering the unmodeled features, such as complex 3D path and variability among reference rock sites. In addition, there is no epistemic uncertainty in our synthetic

dataset (e.g., in magnitude) that would increase the variabilities as in empirical estimates because we know all our modeling parameters perfectly (Crempien and Archuleta, 2017; Valentová et al., 2021). Indeed, Fig. S4.3 shows that the B-E variability of the restricted database reaches the empirical value if we add random perturbation to each scenario's Mw(with ±0.1 standard deviation), representing the error in Mwestimation from real data.

Since the only constraint in the restricted database is placed on the synthetic B-E residuals and not the source model parameters, we examine the possible correlations between the parameters in the restricted database. For example, comparing the expressions for the spectral acceleration plateau from Eq. (4.1) and (4.3), we obtain:

$$\Delta\sigma = \frac{7}{16}\left(\frac{a}{k}\frac{v_r}{v_s}\right)^3 \frac{M_0}{S^{3/2}}, \tag{4.7}$$

where we see possible correlation between stress parameter $\Delta\sigma$ and, for example, rupture velocity v_r. While we see such a correlation in the unrestricted database, in the restricted database the stress parameter is independent of the rupture velocity (see Fig. S4.2a). This can be explained by the anticorrelation between v_r and a, which was not originally present in the scenario database, as suggested also by Eq. (4.7), see Fig. S4.2b. We point out that the anticorrelation is an outcome of the scenario restriction. Nevertheless, adopting such relationship from physical considerations (rupture dynamics) would be preferable.

Relation of the B-E variability to the stress drop variability

There is a long-lasting debate about whether the B-E variability is connected to the variability of stress drop or stress parameter (Atkinson and Beresnev, 1997; Causse and Song, 2015; Gallovič and Valentová, 2020). Moreover, the relation between the stress drop and stress parameter is ambiguous. In empirical studies, the stress drop is usually estimated using corner frequencies under the assumption of the Brune (omega-square) source model (Eq. 4.2) (Abercrombie, 2021). On the other hand, the stress parameter is related to the high-frequency ground motions (Eq. 4.3). The two empirical estimates are discrepant both in mean and variability, so they are suggested to be understood as two distinct, unrelated quantities (Atkinson and Beresnev, 1997).

There are two main reasons for this discrepancy. First, the epistemic error in the corner frequency estimation is amplified by the 3rd power in the relation between the corner frequency and the stress drop (Eq. 4.2), increasing the variability of the inferred Brune stress drop. Second and more substantial is the validity of the Brune model itself. For complex models, the source spectra deviate from the simple Brune spectra, and the corner frequency thus estimated is not directly related to stress conditions on the fault. Indeed, this issue has been recognized in real-event analyses (Archuleta and Ji, 2016; Denolle and Shearer, 2016; Liu et al., 2023) and dynamic source modeling (Gallovič and Valentová, 2020).

On the contrary, the HIC source model employed in this study is based on the Brune source spectrum (although strictly speaking, the Brune model is considered for the individual subsources). Therefore, the stress drop estimated from the corner frequency is directly related to the stress parameter controlling the high-frequency spectral radiation. For this reason, we found that the ratio between standard deviations of the high-frequency B-E ground motion variability τ^{GMM} (0.142 in log10) and the calculated Brune stress parameter Δσ of the restricted database (0.23 in log10) is close to the coefficient $C_{\Delta\sigma}$ from the residual regression analysis (Eq. 4.6) and the theoretically derived relation with power ⅔ (Eq. 4.3):

$$\tau \sim C_{\Delta\sigma}\,\mathrm{std}(\log \Delta\sigma) = 0.64\,\mathrm{std}(\log \Delta\sigma) \approx 2/3\,\mathrm{std}(\log \Delta\sigma) \quad (4.8)$$

An alternative theoretical relation between PGA variability and the stress parameter with a similar scaling coefficient of 5/6 was derived by Causse et al. (2008) and validated by Drouet and Cotton (2015). Our resulting value of 0.64 permits a larger variability of the stress parameter to fit the B-E variability than in Causse et al. (2008). Nevertheless, it depends on the methodology and thus can deviate from other theoretical predictions.

The relation between the standard deviation of the stress parameter and the B-E residuals (Eq. 4.8) can be thus utilized when generating scenarios using models based on the Brune spectrum. Let us emphasize that adopting empirical stress drop standard deviation to determine that of the stress parameter would lead to too large scenario variability. Indeed, in the standard empirical estimates from corner frequencies of apparent moment rate functions of real earthquakes, the Brune stress drop variability is inferred as 0.5 in log10 (i.e., 1.1 in ln) (e.g., Morasca et al., 2022; Bindi et al., 2018a,b; Oth et al., 2017; Baltay et al., 2011; Cotton et al., 2013; Causse and Song, 2015; and references therein). Adopting this value for the stress parameter variability, i.e., corresponding roughly to our unrestricted database, would result in the scenario B-E variability of 0.3 in log10 (0.7 in ln), much higher than the empirical estimate. Contrarily, the standard deviation of the stress parameter of our restricted database is 0.23 in log10, as if it was constrained by the empirical B-E value ($\tau^{GMM} = 0.142$ and Eq. 4.7). Although this analysis was made aposteriori on our dataset, for future applications the stress drop/parameter variability of the synthetic scenarios can be constrained apriori from the empirical B-E variability using Eq. (4.8). Since $\Delta\sigma$ aggregates effects of all other source parameters, one can also randomly sample parameters v_r, a, and S independently from their uniform distributions and limit the scenarios apriori (i.e., before performing the simulations), so that the resulting distribution of the stress parameter follows its target distribution with prescribed standard deviation of Δσ.

Let us also note that the empirical B-E variability might be biased by epistemic errors, such as uncertainty in the Mwestimation, as suggested by dynamic simulations (Valentová et al., 2021) and data analysis of large repeating earthquakes (Yagoda-Biran et al., 2015). Considering this overestimation in the empirical values, the stress parameter variability for the scenario simulations would be even smaller than the value derived from the B-E

one using Eq. (4.8). We acknowledge that our approach of constraining the scenario variability represents an upper limit.

4.6. Conclusions

We have employed a kinematic finite fault model to build a database of ~12000 Mw6.2 earthquake scenarios with varied source-related parameters. The total variability of the simulated scenarios agrees with the empirical one. The mixed-model analysis reveals that while the synthetic within-event (W-E) variability is underestimated, the between-event (B-E) variability (i.e., purely the variability due to changes in the source scenarios) exceeds the empirical values. The former is acceptable, considering the simplification of many path and site complexities in the modeling. However, the overestimation of the synthetic B-E variability related to the changes in source scenarios suggests too large variability in the mean source parameters.

To overcome this issue, we restricted the scenario database by randomly resampling the scenarios to conform their B-E residuals with the prescribed (empirical) distribution. We showed that the standard deviation of the stress parameter (aggregating all source modeling parameters in our models) attains approximately ⅔ of the empirical B-E standard deviation of the adopted Ground Motion Model, in agreement with theoretical considerations for our kinematic model. This relation can be used for future applications to restrict apriori the stress parameter variability of the scenarios (instead of adopting the likely overestimated variability from empirical source spectrum studies). In addition, since the empirical B-E standard deviation is affected by epistemic errors, the stress parameter variability can be considered even smaller for a single seismogenic source.

4.7. Supplemental Material

Table S4.1: Velocity models of (a) Norcia area west of the Sibillini Thrust, (b) Amatrice area, east of the Sibillini Thrust (Fig. 4.1a). The models are plotted in Fig. 4.1b.

(a) Norcia area

Top depth (km)	Vp(km/s)	Vs(km/s)	Rho(g/cm3)	Qp	Qs
0	2.05	1.1	2.94	100	50
0.06	2.79	1.5	2.94	400	200
0.08	3.72	2.0	2.94	400	200
0.4	5.58	3.0	2.94	400	200
1	5.70	3.1	2.94	1000	500
2	5.76	3.1	2.94	2000	1000
5	6.51	3.5	3.15	2000	1000
27	7.00	3.8	3.26	2000	1000
42	7.80	4.2	3.50	2000	1000

(b) Amatrice area

Top depth (km)	Vp(km/s)	Vs(km/s)	Rho(g/cm3)	Qp	Qs
0.00	1.49	0.80	1.90	50	50
0.06	2.23	1.20	1.90	100	100
0.16	3.16	1.70	2.00	100	100
1.00	4.83	2.60	2.84	1000	500
2.00	5.76	3.10	2.94	2000	1000
5.00	6.51	3.50	3.15	2000	1000
27.00	7.00	3.80	3.26	2000	1000
42.00	7.80	4.20	3.50	2000	1000

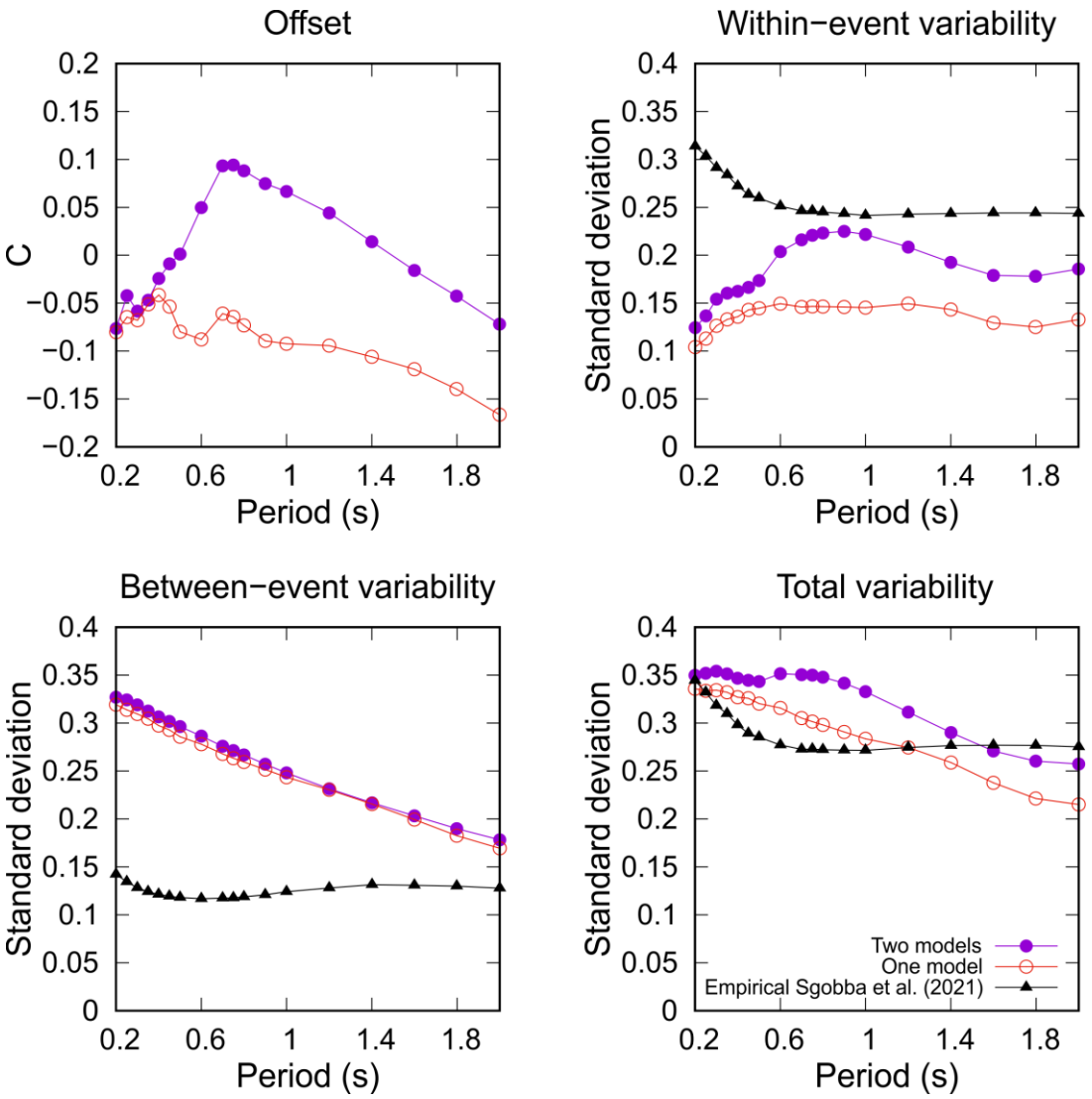

Figure S4.1: Effect of using only one crustal model on the GMM residuals compared to two regional crustal models: Offset, W-E, B-E and total variability (in log 10) of the GMM residuals when using two regional crustal models (violet line with full circles), or only one crustal model of the Amatrice area in the whole domain (red line with red circles). The black line shows the corresponding empirical values of GMM by Sgobba et al. (2021).

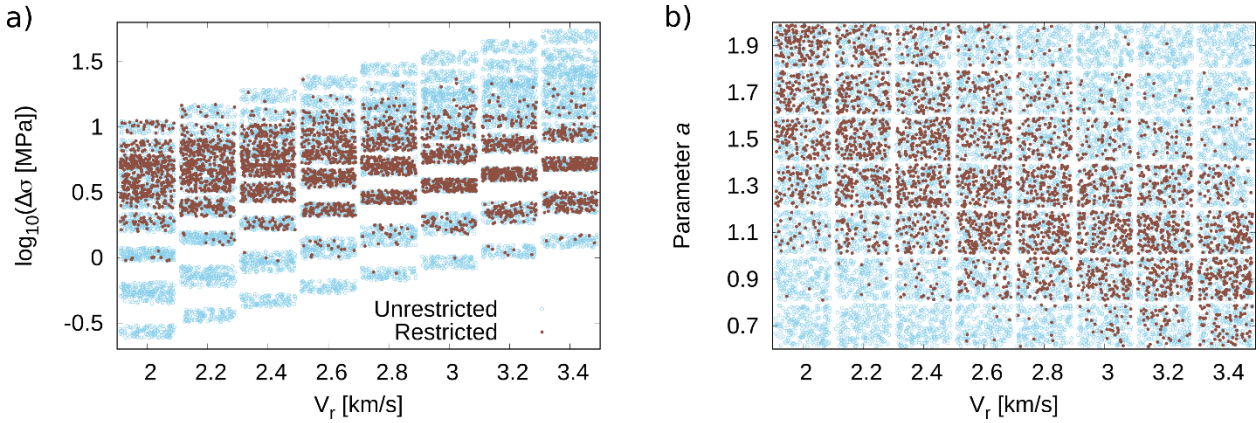

Figure S4.2: Distribution of source parameters in the restricted (brown) and unrestricted (blue) database: a) Stress parameter with respect to rupture velocity v_r, b) parameter a with respect to rupture velocity. For better graphical representations of the model counts, the gridded values are spread to clouds by randomly perturbing their values. The figure demonstrates that the stress parameter in the restricted database attains narrower distribution independent of v_r by anticorrelating v_r and a, which is not prescribed in the original unrestricted database.

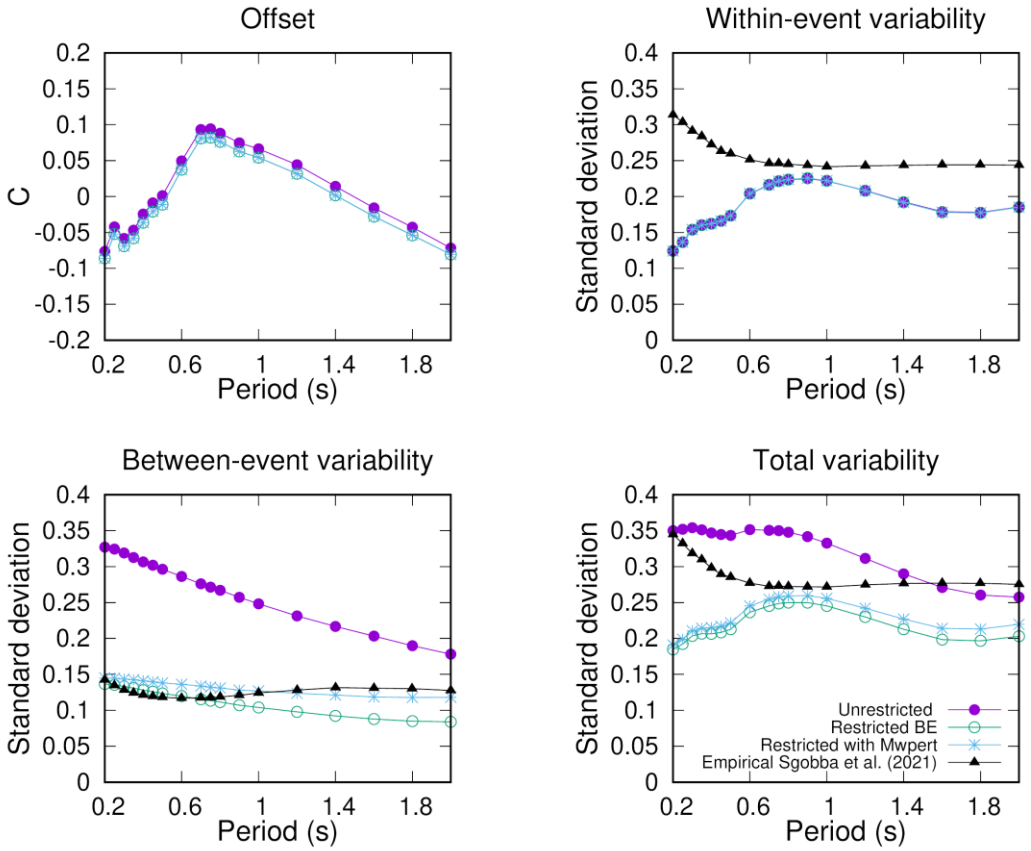

Figure S4.3: Experiment with adding random error in Mw(pretending uncertain real-data estimate) and its effect on the SA residuals: Offset, W-E, B-E, and total standard deviation (in log10) of the unrestricted (violet), restricted (green) and perturbed restricted (blue) database. The black lines show the respective empirical values of GMM by Sgobba et al. (2021). The perturbed SA residuals were generated from restricted database by perturbing the Mwvalue of 6.2 of each scenario using normal distribution with standard deviation of 0.1. The test demonstrates that the effect on the B-E variability is more pronounced on longer periods, where it brings the synthetic B-E standard deviation of the restricted database closer to its empirical value.

5. Conclusions

This Thesis contributes to the development of seismic hazard analysis (SHA) of a given earthquake and helps with understanding how the hazard of ground shaking is distributed in the specific area through a broadband spectrum of frequencies.

We develop kinematic source models using HIC method for two disastrous earthquakes. First the 2023, Mw7.8 Kahramanmaraş earthquake in Türkiye that was one of the largest events in the region. Second the 2016, Mw6.2 Amatrice, Central Italy that was first of the three earthquake sequence. Our aim was to fill the spatial gaps in the recordings that are used for developing GMM and develop a fast option of modeling scenarios.

Through this work we showed that we can create a simple kinematic model of the earthquake that is able to reliably reproduce the records (Paper 1&2). The HIC model combines the coherent wavefield contribution of the rupture propagation at low frequencies and the stochastic contribution of the randomly placed subsources at high frequencies. Throughout the work we showed a number of tests investigating the overlapping frequency band of these two approaches.

In Paper 1 we utilize the HIC model in a rapid manner to show its capabilities in modeling ground motions in broadband frequency for the Kahramanmaraş earthquake. Because of this, we kept the model rather simple. We used a simple kinked geometry of the fault, 1D area velocity model with inserted subsurface layers and constant velocity rupture. We showed that to satisfactorily fit the observed recordings, we need to adjust the rupture propagation with a delay on the southwest part of the fault as it was suggested by earlier studies and reports. We were also able to properly explain the peak ground motions (PGD, PGV, PGA) all around the fault including the strong directivity effect, which can be observed far from the fault. We also point to the limitations of the model, which are clearly visible from our results as we did not account for 3D structures beneath the sites. To precisely model those individual stations and their site effects is a possibility for future research.

With a simple rectangular fault and two 1D velocity models we modeled synthetic waveforms in broadband frequencies for the Amatrice earthquake (Paper 2). We showed different tests and their effect on the synthetics. This validation is very needed for any other work that would use this model, especially when doing hazard scenarios for a given earthquake. We also show how synthetic and empirical predictions can be combined when searching for an optimal model using reference stations, and after that, with the help of site and event terms of non-ergodic GMM, we improved the modeling even at non-reference sites.

The station networks in Central Italy are not dense enough to record earthquakes in a near source region as the coverage is not dense enough. We were able to expand our synthetic waveform coverage and substitute the missing areas with virtual stations and

then create a ground-shaking map of the whole area. That helps better understand the seismic hazard in Central Italy region.

In Paper 3 we use the HIC model as a prediction tool for engineers as it can create many scenarios in broadband frequency range. We modeled Amatrice earthquake scenarios and investigated the within-event (W-E) and between-event (B-E) ground-motion variabilities. We showed that the W-E variability is underestimated, due to the omission of many path and site complexities in our modeling. On the other hand, the B-E variability of our synthetic scenario dataset overestimates the empirical B-E variability of the regional ground motion model (GMM). This suggests that our ranges of source parameters were too wide. We then used the GMM model as a constraint and showed that we can restrict our dataset of synthetic scenarios to match the given B-E variability. As a result of this we propose to restrict the stress drop parameter in synthetic scenarios. This restriction is very valuable as it can a priori constrain the variability of synthetic scenarios for a given event.

With this work, we showed that physics-based modeling for hazard assessment or engineering represents a viable alternative to standard empirical approaches. This is especially true when we do not need to know a priori in detail all the specific features of the faulting process. Therefore, integrating modeling and standard empirical approaches has the potential to enhance seismic hazard assessment and, consequently, improve building codes. Along with stricter enforcement of engineering norms, the impact of the 2016 Amatrice and 2023 Kahramanmaraş events could have been significantly mitigated.

6. Data and resources

For **Paper 1** we used strong motion data, which were produced by the Disaster and Emergency Management Authority of Türkiye (AFAD – TK), https://tdvms.afad.gov.tr. We used GPS data of Event 1 from Taymaz et al., available at https://www.emsc-csem.org/Files/event/1218444/M7.8_updated_text_13-2-2023.pdf, provided by CORS-TR (TUSAGA-Aktif-Türkiye) administered by General Directorate of Land Registry and Cadastre (TKGM) and General Directorate of Mapping (HGM). We thank all the staff involved in building and running high-quality Turkish networks. A preliminary MPS model of both 2023 Türkiye earthquakes was submitted as a report to EMSC (https://static3.emsc.eu/Doc/Additional_Earthquake_Report/1218444/Report_EMSC.pdf).Code DC3D (Okada, 1992) is available at https://www.bosai.go.jp/e/dc3d.html. Continuous static GPS inversion was performed using LinSlipInv (http://fgallovic.github.io/LinSlipInv/). The ISOLA software used in this paper (Zahradník and Sokos, 2018) can be downloaded from https://geo.mff.cuni.cz/~jz/for_ISOLAnews/ and https://github.com/esokos/isola. The maps were generated using the Generic Mapping Tools v6 (Wessel et al., 2019).

All data and metadata for **Paper 2** used for the analyses, were taken from the ITalian ACcelerometric Archive (ITACA) (https://itaca.mi.ingv.it/ItacaNet_32/#/home; Russo et al., 2022) and the Engineering Strong-Motion (ESM) (https://esm-db.eu/#/home) database (Lanzano et al., 2021).

The **Paper 3** is solely based on synthetic calculations.

7. References

Abdelmeguid, M., C. Zhao, E. Yalcinkaya, G. Gazetas, A. Elbanna, and A. Rosakis (2023). Revealing The Dynamics of the Feb 6th 2023 M7.8 Kahramanmaraş/Pazarcik Earthquake: near-field records and dynamic rupture modeling, *preprint*. Doi: https://doi.org/10.48550/arXiv.2305.01825

Abercrombie, R. E. (2021). Resolution and uncertainties in estimates of earthquake stress drop and energy release, *Phil. Trans. R. Soc. A.* 379, 20200131, 20200131.

Abrahamson, N. A., N. M. Kuehn, M. Walling, and N. Landwehr (2019). Probabilistic seismic hazard analysis in California using nonergodic ground-motion models, *Bull. Seismol. Soc. Am.* 109 (4), 1235–1249.

Acarel, D., M. D. Cambaz, F. Turhan, A. K. Mutlu, and R. Polat (2019). Seismotectonics of Malatya Fault, Eastern Turkey, *Open Geosci.* 11, 1098–1111.

Aki, K. and P. G. Richards (2002). Quantitative Seismology. 2nd Edition, *CA: Univ. Sci. Books,* Sausalito, 700.

Akinci, A., H. Aochi, A. Herrero, M. Pischiutta, and D. Karanikas (2017). Physics-based broadband ground-motion simulations for probable Mw≥7.0 earthquakes in the Marmara Sea region (Turkey). *Bull. Seismol. Soc. Am.* 107 (3), 1307–1323. doi: doi.org/10.1785/0120160096.

Al Atik, L., N. Abrahamson, J. J. Bommer, F. Scherbaum, F. Cotton, and N. Kuehn (2010). The variability of ground-motion prediction models and its components, *Seismol. Res. Lett.* 81, no. 5, 794–801.

Ameri, G., A. Emolo, F. Pacor, and F. Gallovič (2011). Ground-motion simulations for the 1980 M 6.9 Irpinia earthquake (southern Italy) and scenario events, *Bull. Seismol. Soc. Am.* 101, no. 3, 1136-1151.

Ameri, G., F. Gallovič, and F. Pacor (2012). Complexity of the Mw6.3 2009 L'Aquila (Central Italy) earthquake: 2. Broadband strong-motion modeling, *J. Geophys. Res.*, 117, B04308.

Ameri, G., F. Gallovič, F. Pacor, and A. Emolo (2009). Uncertainties in strong ground-motion prediction with finite-fault synthetic seismograms: An application to the 1984 M 5.7 Gubbio, Central Italy, earthquake, *Bull. Seismol. Soc. Am.* 99 (2A), 647–663. doi: https://doi.org/10.1785/0120080240

Anderson, J. G., and S. Hough (1984). A model for the shape of the Fourier amplitude spectrum of acceleration at high frequencies, *Bull. Seismol. Soc. Am.* 74, 1969–1984.

Anderson, J. G., J. N. Brune (1999). Probabilistic seismic hazard analysis without the ergodic assumption, *Seism. Res. Lett.* 70 (1): 19–28.

Andrews, D. J. (1980). A stochastic fault model: 1. Static case, *J. Geophys. Res.*, 85(B7), 3867–3877, doi:10.1029/JB085iB07p03867.

Aochi, H., and J. Douglas (2006). Testing the validity of simulated strong ground motion from the dynamic rupture of a finite fault, by using empirical equations, *Bull. Earthq. Eng.* 4, 211–229. doi: doi.org/10.1007/s10518-006-0001-3

Archuleta, R. J., and C. Ji (2016). Moment rate scaling for earthquakes 3.3≤ M≤ 5.3 with implications for stress drop, *Geophys. Res. Lett.* 43, no. 23, 12–004

Atkinson, G. M., and I. Beresnev (1997). Don't call it stress drop, *Seism. Res. Lett.* 68, 3-4.

Baltay, A., and T. Hanks (2017). Uncertainty, variability, and earthquake physics in ground-motion prediction equations, *Bull. Seismol. Soc. Am.* 107.

Baltay, A., S. Ide, g. Prieto, and G. Beroza (2011). Variability in earthquake stress drop and apparent stress, *Geophys. Res. Lett.* 38, L06303. doi:10.1029/2011GL046698.

Baltzopoulos, G., R. Baraschino, E. Chioccarelli, P. Cito, A. Vitale, and I. Iervolino (2023). Near-source ground motion in the M7. 8 Gaziantep (Turkey) earthquake, *Earthq. Eng. Struct. Dyn.*, 1- 10.

Bard P. Y., S. S. Bora, F. Hollender, A. Laurendeau, and P. Traversa (2020). Are the standard Vs30-kappa host-to-target adjustments the only way to get consistent hard-rock ground motion prediction?, *Pure Appl. Geophys.* 177, 2049–2068.

Bates, D., B. Mächler, B. Bolker, and S. Walker (2015). Fitting linear mixed-effects models using lme4, 2015, *J. Stat. Software* 67(1), 1-48.

Bernard, P., A., Herrero, and C. Berge (1996). Modeling directivity of heterogeneous earthquake ruptures, *Bull. Seism. Soc. Am.* 86, 1149–1160.

Bianchi, I., C. Chiarabba, and N. P. Agostinetti (2010). Control of the 2009 L'Aquila earthquake, Central Italy, by a high-velocity structure: A receiver function study, *J. Geophys. Res.* 115, B12326. doi:10.1029/2009JB007087.

Bindi, D., Picozzi, M., Spallarossa, D., Cotton, F. and Kotha, R. (2018b). Impact of magnitude selection on aleatory variability associated with ground-motion prediction equations: Part II - Analysis of the between-event distribution in Central Italy, *Bull. Seismol. Soc. Am.*, 109(1), 251-262.

Bindi, D., Spallarossa, D., Picozzi, M., Scafidi, D., and Cotton, F. (2018a). Impact of magnitude selection on aleatory variability associated with ground-motion prediction equations: Part I - Local, energy, and moment magnitude calibration and stress-drop variability in Central Italy, *Bull. Seismol. Soc. Am.*, 108(3A), 1427-1442. doi: 10.1785/0120170356.

Boncio, P., G. Lavecchia, and B. Pace (2004). Defining a model of 3D seismogenic sources for seismic hazard assessment applications: The case of Central Apennines (Italy), *Journal of Seismology*. 8. 407-425. 10.1023/B:JOSE.0000038449.78801.05.

Boore, D. M. (1983). Stochastic simulation of high-frequency ground motions based on seismological models of the radiated spectra, *Bull. Seism. Soc. Am.* 73, 1865–1894.

Boore, D. M. (2010). Orientation-independent, nongeometric-mean measures of seismic intensity from two horizontal components of motion, *Bull. Seismol. Soc. Am.* 100, no. 4, 1830–1835.

Boore, D. M., J. P. Stewart, E. Seyhan, and G. M. Atkinson (2014). NGAWest2 equations for predicting PGA, PGV, and 5% damped PSA for shallow crustal earthquakes, *Earthq. Spectra* 30, no. 3, 1057–1085.

Bouchon, M. (1981). A simple method to calculate Green's functions for elastic layered media, *Bull. Seism. Soc. Am.*, 71, 959–971.

Bradley, B., D. Pettinga, J. Baker, and J. Fraser (2017). Guidance on the utilization of earthquake-induced ground motion simulations in engineering practice, *Earthq. Spectra* 33.

Brune, J. N. (1970). Tectonic stress and the spectra of seismic shear waves from earthquakes, *J. Geophys. Res.*, 75 (26), 4997– 5009.

Calderoni, G., and Abercrombie, R. E. (2023). Investigating spectral estimates of stress drop for small to moderate earthquakes with heterogeneous slip distribution: Examples from the 2016–2017 Amatrice earthquake sequence, *J. Geophys. Res.: Solid Earth*, 128, e2022JB025022. https://doi.org/10.1029/2022JB025022

Castro, R., L. Colavitti, C. Vidales-Basurto, F. Pacor, S. Sgobba and G. Lanzano (2022). Near-source attenuation and spatial variability of the spectral decay parameter kappa in Central Italy, *Seism. Res. Lett.* 93, 1-12.

Causse, M., and S. G. Song (2015). Are stress drop and rupture velocity of earthquakes independent? Insight from observed ground motion variability, *Geophys. Res. Lett.* 42, 7383– 7389. doi:10.1002/2015GL064793.

Causse, M., Cotton, F., Cornou, C., and P.-Y. Bard (2008). Calibrating Median and Uncertainty Estimates for a Practical Use of Empirical Green's Functions Technique, Bull. Seism. Soc. Am. 98, 344–353.

Čejka, F., J. Zahradník, F. Turhan, E. Sokos, and F. Gallovič (2023). Long-period directivity pulses of strong ground motion during the 2023 Mw7.8 Kahramanmaraş earthquake, *Commun. Earth Environ* 4, 413. https://doi.org/10.1038/s43247-023-01076-x

Čejka, F., Ľ. Valentová Krišková, S. Sgobba, F. Pacor, C. Felicetta, and F. Gallovič (2024a). Ground motion modeling of the 2016 Mw6.2 Amatrice (Italy) earthquake by a broadband hybrid kinematic approach, including empirical site effects, Seism. Res. Lett. https://doi.org/10.1785/0220230409

Čejka, F., S. Sgobba, F. Pacor, C. Felicetta, Ľ. Valentová and F. Gallovič (2024b). Constraining between-event variability of kinematic rupture scenarios by empirical ground-motion model: A case study in Central Italy, *Bull. Seismol. Soc. Am*., 114 (4): 2138–2150. https://doi.org/10.1785/0120230251.

Cetin, K., and M. Ilgaç (2023). Reconnaissance Report on February 6, 2023 Kahramanmaraş-Pazarcık (Mw=7.7) and Elbistan (Mw=7.6) Earthquakes, T*ürkiye Earthquake Reconnaissance and Research Alliance*. Doi: https://doi.org/10.13140/RG.2.2.15569.61283/1

Champion, C., and A. Liel (2012). The effect of near-fault directivity on building seismic collapse risk, *Earthq. Eng. Struct. Dyn.*, 41, 1391-1409.

Chiaraluce, L., R. Di Stefano, E. Tinti, L. Scognamiglio, M. Michele, E. Casarotti, M. Cattaneo, P. De Gori, C. Chiarabba, G. Monachesi, A. Lombardi, L. Valoroso, D. Latorre, and S. Marzorati (2017). The 2016 Central Italy Seismic Sequence: A First Look at the Mainshocks, Aftershocks, and Source Models, *Seismol. Res. Lett.* 88 (3), 757–771. https://doi.org/10.1785/0220160221.

Cirella, A., G. Pezzo, and A. Piatanesi (2018). Rupture kinematics and structural-rheological control of the 2016 Mw6.1 Amatrice (Central Italy) earthquake from joint inversion of seismic and geodetic data, *Geophys. Res. Lett.* 45, 12, 302–12,311. doi.org/10.1029/2018GL080894.

Colavitti, L., G. Lanzano, S. Sgobba, F. Pacor, and F. Gallovič (2022). Empirical Evidence of Frequency-Dependent Directivity Effects from Small-to-Moderate Normal Fault Earthquakes in Central Italy, *J. Geophys. Res. Solid Earth* 127, e2021JB023498.

Cornell, C. A. (1968). Engineering seismic risk analysis. *Bull. Seismol. Soc. Am.*, 58(5), 1583–1606.

Cotton, F., and O. Coutant (1997). Dynamic stress variations due to shear faults in a plane-layered medium, *Geophys. J. Int.* 128, 3, 676–688.

Cotton, F., R. Archuleta, M. Causse (2013). What is sigma of the stress drop?, *Seism. Res. Lett.* 84 (1): 42–48. doi: https://doi.org/10.1785/0220120087

Crempien, J.G.F., and R. J. Archuleta (2017). Within-event and between-events ground motion variability from earthquake rupture scenarios, *Pure Appl. Geophys.* 174, 3451–3465. doi.org/10.1007/s00024-017-1615-x

Cultrera, G., A. Cirella, E. Spagnuolo, A. Herrero, E. Tinti, and F. Pacor (2010). Variability of kinematic source parameters and its implication on the choice of the design scenario, *Bull. Seismol. Soc. Am.*100 (3): 941–953. doi: doi.org/10.1785/0120090044

Dal Zilio, L. and J.-P. Ampuero (2023). Earthquake doublet in Turkey and Syria, *Commun. Earth Environ.*, 4, 71.

Denolle, M. A., and P. M. Shearer (2016). New perspectives on selfsimilarity for shallow thrust earthquakes, *J. Geophys. Res.* 121, no. 9, 6533–6565.

Douglas, J., and H. Aochi (2016). Assessing components of ground-motion variability from simulations for the Marmara Sea region (Turkey), *Bull. Seismol. Soc. Am.* 106, 300-306.

Dreger, D. S., G. C. Beroza, S. M. Day, C. A. Goulet, T. H. Jordan, P. A. Spudich, and J. P. Stewart (2015). Validation of the SCEC broadband platform V14. 3 simulation methods using pseudo spectral acceleration data, *Seism. Res. Lett.* 86(1), 39-47.

Drouet, S., and F. Cotton (2015). Regional stochastic GMPEs in low-seismicity areas: Scaling and aleatory variability analysis—Application to the French Alps, *Bull. Seismol. Soc. Am.* 105, 1883–1902.

Dujardin, A., M. Causse, C. Berge-Thierry, and F. Hollender (2018). Radiation patterns control the near-dource ground-motion saturation effect, *Bull. Seismol. Soc. Am.* 108 (6), 3398-3412.

Duman, T. Y., and Ö. Emre (2013). The East Anatolian Fault: geometry, segmentation and jog characteristics, Geological Development of Anatolia and the Easternmost Mediterranean Region, Author(s): A. H. F. Robertson, O. Parlak, U. C. Ünlügenç.

Duputel, Z., and L. Rivera (2017). Long-period analysis of the 2016 Kaikoura earthquake, *Phys. Earth Planet. Inter.* 265, 62–66.

Esteva L. (1969). Seismicity Predction, A Bayesian Approach, paper presented at 4th World Conference on Earthquake Engineering, Santiago, Chile.

Felicetta, C., C. Mascandola, D. Spallarossa, F. Pacor, S. Hailemikael, and G. Di Giulio (2021). Quantification of site effects in the Amatrice area (Central Italy): Insights from ground-motion recordings of the 2016–2017 seismic sequence, *Soil Dyn. Earthq. Eng.*, 142, 106565.

Frankel, A. (1991). High-frequency spectral falloff of earthquakes, fractal dimension of complex rupture, b value, and the scaling of strength on faults, *J. Geophys.* 96, 6291–6302

Galli P., E. Peronace, and A. Tertulliani (2016a). Rapporto sugli effetti macrosismici del terremoto del 24 agosto 2016 di Amatrice in scala MCS, Roma, Rapporto congiunto DPC, CNRIGAG, 15pp. doi:10.5281/zenodo.161323.

Gallovič, F. (2016). Modeling velocity recordings of the Mw6.0 South Napa, California, earthquake: unilateral event with weak high-frequency directivity, *Seism. Res. Lett.* 87, 2-14.

Gallovič, F., and J. Burjánek (2007). High-frequency Directivity in Strong Ground Motion Modeling Methods, *Ann. Geophys.*, 50 (2), 203-211.

Gallovič, F., and J. Brokešová (2007). Hybrid k-squared source model for strong ground motion Simulations: Introduction, *Phys. Earth Planet. Interiors* 160, 34-50. doi: 10.1016/j.pepi.2006.09.002.

Gallovič, F., and Ľ. Valentová (2020). Earthquake stress drops from dynamic rupture simulations constrained by observed ground motions, *Geophys. Res. Lett.* 47, e2019GL085880. doi.org/10.1029/2019GL085880.

Gallovič, F., and Valentová, Ľ. (2023). Broadband strong ground motion modeling using planar dynamic rupture with fractal parameters, *J. Geophys. Res. Solid Earth* 128, e2023JB026506. doi: 10.1029/2023JB026506.

Gallovič, F., G. Ameri, J. Zahradník, J. Janský, V. Plicka, E. Sokos, A. Askan, and M. Pakzad (2013). Fault process and broadband ground-motion simulations of the 23 October 2011 Van (Eastern Turkey) earthquake, *Bull. Seismol. Soc. Am.*, 103, 3164-3178.

Gallovič, F., J. Zahradník, V. Plicka, E. Sokos, C. Evangelidis, I. Fountoulakis, and F. Turhan (2020). Complex rupture dynamics on an immature fault during the 2020 Mw6.8 Elazığ earthquake, Turkey, *Commun. Earth Environ.* 1, 40.

Gallovič, F., Ľ. Valentová, J.-P. Ampuero, and A.-A. Gabriel (2019). Bayesian dynamic finite-fault inversion: 2. Application to the 2016 Mw6.2 Amatrice, Italy, earthquake, *J. Geophys. Res. Solid Earth* 124, 6970-6988.

Gallovič, F., W. Imperatori, and P. M. Mai (2015). Effects of three-dimensional crustal structure and smoothing constraint on earthquake slip inversions: case study of the Mw6.3 2009 L'Aquila earthquake, *J. Geophys. Res.* 120, 428-449.

Gerstenberger, M. C., Marzocchi, W., Allen, T., Pagani, M., Adams, J., Danciu, L., et al. (2020). Probabilistic seismic hazard analysis at regional and national scales: State of the art and future challenges. *Reviews of Geophysics*, 58, e2019RG000653. https://doi.org/10.1029/2019RG000653

Goldberg, D. E., T. Taymaz, N. G. Reitman, A. E. Hatem, S. Yolsal-Çevikbilen, W. D. Barnhart, T. S. Irmak, D. J. Wald, T. Öcalan, W. L. Yeck, B. Özkan, J. A. Thompson Jobe, D. R. Shelly, E. M. Thompson, C. B. DuRoss, P. S. Earle, R. W. Briggs, H. Benz, C. Erman, A. H. Doğan, and C. Altuntaş (2023). Rapid Characterization of the February 2023 Kahramanmaraş, Türkiye, Earthquake Sequence, *The Seismic Record*, 3 (2), 156–167.

Goulet, C. A., N. A. Abrahamson, P. G. Somerville, and K. E. Wooddell (2015). The SCEC broadband platform validation exercise: methodology for code validation in the context of seismic-hazard analyses, *Seism. Res. Lett.* 86(1), 17-26.

Graves, R., and A. Pitarka (2010). Broadband ground-motion simulation using a hybrid approach, *Bull. Seismol. Soc. Am.* 100. 2095-2123.

Graves, R., T.H. Jordan, S. Callaghan, et al. (2011). CyberShake: A Physics-Based Seismic Hazard Model for Southern California. *Pure Appl. Geophys.* 168, 367-381.

Gürer, D., J. Hubbard, and W. Bohon (2023). Science on social media, *Commun. Earth Environ.* 4, 148.

Hall, J. F., T. H. Heaton, M. W. Halling, and D. J. Wald (1995). Near-source ground motion and its effects on flexible buildings, *Earthq. Spectra* 11, 569-605.

Hall, S., (2023). What Turkey's earthquake tells us about the science of seismic forecasting, *Nature*, 615, 388-389.

Hancılar, U., K. Şeşetyan, E. Ç. N. Yenihayat, H. Süleyman, N. Açıkgöz, Ş. Dede, and Ş. Acar (2023). Kahramanmaraş – Gaziantep Türkiye M7.7 Earthquake, 6 February 2023 (04:17 GMT+03:00): Strong Ground Motion and Building Damage Estimations Preliminary Report (v6), *Boğaziçi University, Kandilli Observatory and Earthquake Research Institute, Department of Earthquake Engineering*.

Haskell, N. (1964), Total energy and energy spectral density of elastic wave radiation from propagating faults, *Bull. Seismol. Soc. Am.*, 54, 1811–1851.

Hicks, S. P., R. Okuwaki, A. Steinberg, C. A. Rychert, N. Harmon, R. E. Abercrombie, P. Bogiatzis, D. Schlaphorst, J. Zahradnik, J-M. Kendall, Y. Yagi, K. Shimizu, and H. Sudhaus (2020). Back-propagating supershear rupture in the 2016 Mw7.1 Romanche transform fault earthquake, *Nat. Geosci.* 13, 647–653.

Irikura, K., and K. Kamae (1994). Estimation of strong ground motion in broad-frequency band based on a seismic source scaling model and empirical Green's function technique, *Ann. Geofis.* XXXVII, 1721–1743.

Jia, Z., Z. Jin, M. Marchandon, T. Ulrich, A.-A. Gabriel, W. Fan, P. Shearer, X. Zou, J. Rekoske, F. Bulut, A. Garagon, and Y. Fialko (2023). The complex dynamics of the 2023 Kahramanmaraş, Turkey, Mw7.8-7.7 earthquake doublet, Science, eadi0685.

Jiang, J., Y. Bock, and E. Klein (2021). Coevolving early afterslip and aftershock signatures of a San Andreas fault rupture, *Sci. Adv.* 7, eabc1606.

Kaneko, Y., and P. M. Shearer (2015). Variability of seismic source spectra, estimated stress drop, and radiated energy, derived from cohesive-zone models of symmetrical and

asymmetrical circular and elliptical ruptures, *J. Geophys. Res. Solid Earth* 120, 1053–1079, doi:10.1002/2014JB011642.

Kaneko, Y., N. Lapusta, and J.-P. Ampuero (2008). Spectral element modeling of spontaneous earthquake rupture on rate and state faults: Effect of velocity-strengthening friction at shallow depths, *J. Geophys. Res.*, 113, B09317.

Karabacak, V., Ç. Özkaymak, H. Sözbilir, O. Tatar, B. Aktuğ, Ö. C. Özdağ, R. Çakir, E. Aksoy, F. Koçbulut, M. Softa, E. Akgün, A. Demir, and G. Arslan (2023). The 2023 Pazarcık (Kahramanmaraş, Türkiye) earthquake (Mw7.7): implications for surface rupture dynamics along the East Anatolian Fault Zone, *J. Geol. Soc.* 180 (3), jgs2023–020.

Karabulut, H., S. E. Güvercin, J. Hollingsworth, and A. Ö. Konca (2023). Long silence on the East Anatolian Fault Zone (Southern Turkey) ends with devastating double earthquakes (6 February 2023) over a seismic gap: implications for the seismic potential in the Eastern Mediterranean region, *J. Geol. Soc*., 180 (3), jgs2023-021.

Kemna, K. B., Verdecchia, A., and Harrington, R. M. (2021). Spatio-temporal evolution of earthquake static stress drop values in the 2016–2017 central Italy seismic sequence, *J. Geophys. Res.*: Solid Earth, 126(11), e2021JB022566.

Kikuchi, M., and H. Kanamori (1991). Inversion of complex body waves. III, *Bull. Seism. Soc. Am.*, 81, 2335–2350.

Kotha, S. R., D. Bindi, and F. Cotton (2016). Partially non-ergodic region specific GMPE for Europe and Middle-East, *Bull. Earthq. Eng.* 14, 1245–1263.

Kotha, S. R., D. Bindi, and F. Cotton (2022). A regionally adaptable ground-motion model for fourier amplitude spectra of shallow crustal earthquakes in Europe, *Bull. Earthq. Eng.* 20, 711-740.

Kotha, S. R., F. Cotton, and D. Bindi (2019). Empirical Models of Shear-Wave Radiation Pattern Derived from Large Datasets of Ground-Shaking Observations, *Scientific Reports*, 9, 981. https://doi.org/10.1038/s41598-018-37524-4.

Krinitzsky, E. L. (1995). Deterministic versus probabilistic seismic hazard analysis for critical structures. Engineering Geology, 40(1-2), 1–7. https://doi.org/10.1016/0013-7952(95)00031-3

Lanzano, G., Ch. Felicetta, F. Pacor, D. Spallarossa, and P. Traversa (2020). Methodology to identify the reference rock sites in regions of medium-to-high seismicity: An application in Central Italy, *Geophys. J. Int.* 222, 2053–2067. doi.org/10.1093/gji/ggaa261.

Lanzano, G., Felicetta, C., Pacor, F., Spallarossa, D. and P. Traversa (2022). Generic-To-Reference Rock Scaling Factors for Seismic Ground Motion in Italy. *Bull. Seismol. Soc. Am.* 112 (3),1583–1606. https://doi.org/10.1785/0120210063

Lanzano, G., L. Luzi, C. Cauzzi, et al. (2021). Accessing European Strong-Motion Data: An update on ORFEUS coordinated services, *Seism. Res. Lett.* 92, 1642–1658. doi: doi.org/10.1785/0220200398.

Lanzano, G., M. D'Amico, C. Felicetta, L. Luzi, and R. Puglia (2017). Update of the single-station sigma analysis for the Italian strong-motion stations, *Bull. Earthquake Eng.* 15, 2411–2428. https://doi.org/10.1007/s10518-016-9972-x.

Lawson, C. L., and R. J. Hanson (1974). Solving least squares problems. In: *Prentice-Hall Series in Automatic Computation*, vol. 340, Prentice-Hall, Upper Saddle River, N. J.

Lee, R. L., A. Brendon, P. J. Bradley, R. W. Stafford, A. Graves, and M. Rodriguez (2020). Hybrid broadband ground motion simulation validation of small magnitude earthquakes in Canterbury, New Zealand, *Earthq. Spectra* 36, 673–699. doi: doi.org/10.1177/8755293019891718.

Lekkas, E., P. Carydis, E. Vassilakis, S. Mavroulis, I. Argyropoulos, A. Sarantopoulou, M. Mavrouli, A. Konsolaki, M. Gogou, K.-N. Katsetsiadou, E. Kotsi, N.-I. Spyrou, M. Diakakis, H. Kranis, E. Skourtsos, S. Lozios, and K. Soukis (2023). The 6 February 6 2023 Turkey-Syria Earthquakes, *Newsletter of Environmental, Disaster and Crises Management Strategies*, 29, ISSN 2653-9454.

Lin J., and C. Smerzini (2022). Variability of physics-based simulated ground motions in Thessaloniki urban area and its implications for seismic risk assessment, *Front. Earth Sci.* 10:951781. doi: 10.3389/feart.2022.951781

Lin, P.-S., B. Chiou, N. Abrahamson, M. Walling, C.-T. Lee, and C.-T. Cheng (2011). Repeatable Source, Site, and Path Effects on the Standard Deviation for Empirical Ground-Motion Prediction Models, *Bull. Seismol. Soc. Am.* 101, 2281–2295.

Liu, J., and J. Zahradník (2020). The 2019 MW5.7 Changning earthquake, Sichuan Basin, China: A shallow doublet with different faulting styles, *Geophys. Res. Lett.* 47, e2019GL085408.

Liu, J., L. Li, J. Zahradník, E. Sokos, C. Liu, and X. Tian (2018). North Korea's 2017 test and its nontectonic aftershock, *Geophys. Res. Lett.* 45.

Liu, M., Y. Huang, and J. Ritsema (2023). Characterizing multisubevent earthquakes using the Brune source model, *Bull. Seismol. Soc. Am.* 113 (2), 577–591. doi: 10.1785/0120220192

Loviknes, K., S. R. Kotha, F. Cotton, and D. Schorlemmer (2021). Testing Nonlinear Amplification Factors of Ground-Motion Models, *Bull. Seismol. Soc. Am.* 111 (4): 2121–2137. https://doi.org/10.1785/0120200386.

Luzi, L., M. D'Amico, M. Massa, and R. Puglia (2019). Site effects observed in the Norcia intermountain basin (Central Italy) exploiting a 20-year monitoring, *Bull. Earthquake Eng.* 17, 97–118. https://doi.org/10.1007/s10518-018-0444-3.

Mai, P. and G. C. Beroza (2003). A hybrid method for calculating near-source, broadband seismograms: Application to strong motion prediction, *Phys. Earth Planet. Inter.* 137, 183-199.

Mai, P. M., T. Aspiotis, T. A. Aquib, E. V. Cano, D. Castro-Cruz, A. Espindola-Carmona, B. Li, X. Li, J. Liu, R. Matrau, A. Nobile, K. H. Palgunadi, M. Ribot, L. Parisi, C. Suhendi, Y. Tang, B. Yalcin, U. Avşar, Y. Klinger, and S. Jónsson (2023). The Destructive Earthquake Doublet of 6 February 2023 in South-Central Türkiye and Northwestern Syria: Initial Observations and Analyses, *The Seismic Record* 2023, 3 (2), 105–115.

Mariucci, M. T., and P. Montone (2020). Database of Italian present-day stress indicators, IPSI 1.4, *Sci. Data* 7, 298. doi: 10.1038/s41597-020-00640-w. PMID: 32901031; PMCID: PMC7479623.

McCallen D., F. Petrone, M. Miah, A. Pitarka, A. Rodgers, and N. Abrahamson (2021). EQSIM - A multidisciplinary framework for fault-to-structure simulations on exascale computers Part II: Regional simulations of building response. *Earthquake Spectra* (37) 2, 736-761.

Melgar, D., T. Taymaz, A. Ganas, B. Crowell, T. Öcalan, M. Kahraman, V. Tsironi, S. Yolsal-Çevikbil, S. Valkaniotis, T. S. Irmak, T. Eken, C. Erman, B. Özkan, A. H. Dogan, and C. Altuntaş (2023). Sub- and super-shear ruptures during the 2023 Mw7.8 and Mw7.6 earthquake doublet in SE Türkiye, *Seismica*, 2, 3.

Morasca, P., D. Bindi, K. Mayeda, J. Roman-Nieves, J. Barno, W. R. Walter, and D. Spallarossa (2022). Source scaling comparison and validation in Central Italy: Data intensive direct s-waves versus the sparse data coda envelope methodology, *Geophys. J. Int.* 231, Issue 3, 1573–1590. doi.org/10.1093/gji/ggac268

Morasca, P., W. R. Walter, K. Mayeda, and M. Massa (2019). Evaluation of earthquake stress parameters and its scaling during the 2016-2017 Amatrice-Norcia-Visso sequence—Part I, *Geophys. J. Int.* 218 (1), 446–455, doi: 10.1093/gji/ggz165.

Ojeda, J., A. Akinci, E. Tinti, S. Arriola, and S. Ruiz (2021). Hybrid broadband strong-motion simulation to investigate the nearsource characteristics of the M6.5, 30 October 2016 Norcia, Italy earthquake, *Soil Dynam. Earthq. Eng.* 149, 106866. doi.org/10.1016/j.soildyn.2021.106866.

Okada, Y. (1992). Internal deformation due to shear and tensile faults in a half-space. *Bull. Seismol. Soc. Am.* 82 (2): 1018–1040.

Okuwaki, R., Y. Yagi, T. Taymaz, and S. P. Hicks (2023). Multi-scale rupture growth with alternating directions in a complex fault network during the 2023 south-eastern Türkiye and Syria earthquake doublet, *Geophys. Res. Lett.* 50, e2023GL103480.

Oth, A., H. Miyake, and D. Bindi (2017). On the relation of earthquake stress drop and ground motion variability, *J. Geophys. Res. Solid Earth* 122, 5474– 5492. doi:10.1002/2017JB014026.

Ozer, C., M. Ozyaziciglu, E. Gök, and O. Polat (2019). Imaging the Crustal Structure Throughout the East Anatolian Fault Zone, Turkey, by Local Earthquake Tomography, *Pure Appl. Geophys.* 176, 2235–2261.

Özkan, A., H. H. Yavaşoglu, and F. Masson (2023). Present-day strain accumulations and fault kinematics at the Hatay Triple Junction using new geodetic constraints, *Tectonophysics*, 854, 229819.

Pacor, F., D. Spallarossa, A. Oth, L. Luzi, R. Puglia, L. Cantore, A. Mercuri, M. D'Amico, and D. Bindi (2016). Spectral models for ground motion prediction in the L'Aquila region (Central Italy): evidence for stress-drop dependence on magnitude and depth, *Geophys. J. Int.* 204, Issue 2, 697–718. doi.org/10.1093/gji/ggv448

Pacor, F., Gallovič, F., Puglia, R., Luzi, L., & D'Amico, M. (2016). Diminishing high-frequency directivity due to a source effect: Empirical evidence from small earthquakes in the Abruzzo region, Italy. Geophysical Research Letters, 43(10), 5000-5008

Paolucci, R., C. Smerzini, and M. Vanini (2021). BB-SPEEDset: A validated dataset of broadband near-source earthquake ground motions from 3D physics-based numerical simulations, *Bull. Seismol. Soc. Am.* 111 (5): 2527–2545.

Paolucci, R., F. Gatti, M. Infantino, C. Smerzini, A. G. Özcebe, and M. Stupazzini (2018). Broadband Ground Motions from 3D Physics-Based Numerical Simulations Using Artificial Neural Networks, *Bull. Seismol. Soc. Am.* 108 (3A): 1272–1286. doi: https://doi.org/10.1785/0120170293

Parker, G. A., M. P. Moschetti, and E. M. Thompson (2023). Ground-Motion Variability from Kinematic Rupture Models and the Implications for Nonergodic Probabilistic Seismic Hazard Analysis, Seismol. Res. Lett., doi: 10.1785/0220220380.

Petersen, G. M., P. Büyükakpinar, F. O. V. Sanhueza, M. Metz, S. Cesca, K. Akbayram, J. Saul, and T. Dahm (2023). The 2023 Southeast Türkiye Seismic Sequence: Rupture of a Complex Fault Network, *The Seismic Record*, 3 (2), 134–143.

Pilz, M., F. Cotton, and C. Zhu (2022). How much are sites affected by 2-D and 3-D site effects? A study based on single-station earthquake records and implications for ground motion modelling, *Geophys. J. Int.* 228, Issue 3, 1992–2004, https://doi.org/10.1093/gji/ggab454.

Pischiutta, M., A. Akinci, E. Tinti, and A. Herrero (2021). Broad-band ground-motion simulation of 2016 Amatrice earthquake, Central Italy, *Geophys. J. Int.* 224, Issue 3, 1753–1779. doi.org/10.1093/gji/ggaa412.

Pischiutta, M., A. Akinci, L. Malagnini, and A. Herrero (2016). Characteristics of the strong ground motion from the 24th August 2016 Amatrice earthquake, *Ann. Geophys.* 59.

Pitarka, A., A. Akinci, P. DeGori, and M. Buttinelli (2021b). Deterministic 3D Ground-Motion Simulations (0-5Hz) and Surface Topography Effects of the 30 October 2016 Mw6.5 Norcia, Italy Earthquake, *Bull. Seismo. Soc. Am.* 1-25, doi: 10.1785/0120210133.

Pitarka, A., R. Graves, K. Irikura, K. Miyakoshi, C. Wu, H. Kawase, A. Rodgers, and D. McCallen (2021a). Refinements to the Graves–Pitarka kinematic rupture generator, including a dynamically consistent slip-rate function, applied to the 2019 Mw7.1 Ridgecrest earthquake, *Bull. Seismol. Soc. Am.* 112 (1), 287–306. doi: doi.org/10.1785/0120210138.

Pizzi, A., A. Di Domenica, F. Gallovič, L. Luzi, and R. Puglia (2017). Fault segmentation as constraint to the occurrence of the main shocks of the 2016 Central Italy seismic sequence. *Tectonics*, 36, 2370– 2387. doi.org/10.1002/2017TC004652.

Premus, J. (2023). Joint inverse modeling of coseismic and postseismic slip of the 2014 South Napa, California, earthquake, Doctoral thesis, Charles university, Faculty of Mathematics and Physics, Department of Geophysics.

Razafindrakoto, H. N. T., B. A. Bradley, and R. W. Graves (2018). Broadband ground-motion simulation of the 2011 Mw6.2 Christchurch, New Zealand, earthquake, *Bull. Seismol. Soc. Am.* 108 (4): 2130–2147. doi: doi.org/10.1785/0120170388.

Reiter, L. (1991). Earthquake hazard analysis issues and insights, (p. 254). New York: Colombia University Press.

Reitman, N.G., R. W. Briggs, W. D. Barnhart, J. A. Thompson Jobe, C. B. DuRoss, A. E. Hatem, R. D. Gold, S. Akçiz, R. D. Koehler, J. D. Mejstrik, and C. Collett (2023), Fault rupture mapping of the 6 February 2023 Kahramanmaraş, Türkiye, earthquake sequence from satellite data: U.S. Geological Survey data release. Doi: https://doi.org/10.5066/P985I7U2

Rodriguez-Marek, A., F. Cotton, N. A. Abrahamson, S. Akkar, L. Al Atik, B. Edwards, G. A. Montalva, and H. M. Dawood (2013). A model for single-station standard deviation using data from various tectonic regions, *Bull. Seismol. Soc. Am.* 103 (6): 3149–3163. doi: doi.org/10.1785/0120130030

Romeo R., and A. Prestininzi (2000). Probabilistic versus deterministic seismic hazard analysis: an integrated approach for siting problems, *Soil Dynamics and Earthquake Engineering*, Volume 20, Issues 1–4, Pages 75-84, ISSN 0267-7261, https://doi.org/10.1016/S0267-7261(00)00039-7.

Rosakis, A., M. Abdelmeguid, and A. Elbanna (2023). Evidence of Early Supershear Transition in the Mw7.8 Kahramanmaraş Earthquake From Near-Field Records, pre-print, *EarthArXiv*. Doi: https://doi.org/10.31223/X5W95G.

Russo E., C. Felicetta, M. D'Amico, S. Sgobba, G. Lanzano, C. Mascandola, F. Pacor, and L. Luzi (2022). Italian Accelerometric Archive v3.2 - Istituto Nazionale di Geofisica e Vulcanologia, Dipartimento della Protezione Civile Nazionale. doi: 10.13127/itaca.3.2.

Seabold, Skipper, and Josef Perktold (2010). "Statsmodels: Econometric and statistical modeling with python." Proceedings of the 9th Python in Science Conference.

Sgobba, S., Felicetta, C., Bortolotti, T., Menafoglio, A., Lanzano, G., Pacor, F. (2024). A geostatistical modelling of empirical amplification functions and related site proxies for shaking scenarios in Central Italy, *Soil Dynamics and Earthquake Engineering*, Volume 179, 108496, ISSN 0267-7261, https://doi.org/10.1016/j.soildyn.2024.108496.

Sgobba, S., G. Lanzano, and F. Pacor (2021). Empirical nonergodic shaking scenarios based on spatial correlation models: An application to Central Italy, *Earthquake Engineering & Structural Dynamics*, 50(1), 60–80. https://doi.org/10.1002/eqe.3362.

Sgobba, S., G. Lanzano, L. Colavitti, P. Morasca, M. C. D'Amico, and D. Spallarosa (2023). Physics-based parametrization of a FAS nonergodic ground motion model for Central Italy, *Bull. Earthq. Eng.* 21, 4111–4137.

Sokos, E., and J. Zahradnik (2013). Evaluating Centroid-Moment-Tensor Uncertainty in the New Version of ISOLA Software. *Seismol. Res. Lett.* 84, 656-665.

Sokos, E., F. Gallovič, C.P. Evangelidis, A. Serpetsidaki, V. Plicka, J. Kostelecký, and J. Zahradník (2020). The 2018 Mw6.8 Zakynthos, Greece, earthquake: Dominant strike-slip faulting near subducting slab, *Seismol. Res. Lett.* 1–12.

Sokos, E., J. Zahradník, F. Gallovič, A. Serpetsidaki, V. Plicka, and A. Kiratzi (2016). Asperity break after 12 years: The Mw6.4 2015 Lefkada (Greece) earthquake, *Geophys. Res. Lett.*, 43, 6137–6145.

Song, G. S. (2016). Developing a generalized pseudo-dynamic source model of Mw6.5–7.0 to simulate strong ground motions, *Geophys. J. Int.* 204, Issue 2, 1254–1265. doi.org/10.1093/gji/ggv521

Spagnuolo, E., A. Akinci, A. Herrero, and S. Pucci (2016). Implementing the Effect of the Rupture Directivity on PSHA for the City of Istanbul, Turkey, Bull. Seism. Soc. Am., 106 (6), 2599-2613.

Spudich, P., B. Rowshandel, S. K. Shahi, J. W. Baker, and B. S.-J. Chiou (2014). Comparison of NGA-West2 directivity models, Earthq. Spectra, 30, 1199–1221.

Stafford, P. J. (2014). Crossed and nested mixed-effects approaches for enhanced model development and removal of the ergodic assumption in empirical ground-motion models, *Bull. Seism. Soc. Am.* 104 (2): 702–719. doi: doi.org/10.1785/0120130145.

Strasser, F. O., N. A. Abrahamson, and J. J. Bommer (2009). Sigma: Issues, insights, and challenges, *Seismol. Res. Lett.* 80, no. 1, 40–56.

Supino, M., Festa, G., and Zollo, A. (2019). A probabilistic method for the estimation of earthquake source parameters from spectral inversion: application to the 2016–2017 Central Italy seismic sequence, *Geophys. J. Int.*, 218(2), 988-1007.

Taufiqurrahman, T., A.-A. Gabriel, T. Ulrich, Ľ. Valentová, and F. Gallovič (2023). Broadband dynamic rupture modeling with fractal fault roughness, frictional heterogeneity, viscoelasticity and topography: The 2016 Mw6.2 Amatrice, Italy earthquake, *Geophys. Res. Lett.*, 49, e2022GL098872. doi: doi.org/10.1029/2022GL098872.

Taymaz, T., A. Ganas, S. Yolsal-Çevikbilen, F. Vera, T. Eken, C. Erman, D. Keleş, V. Kapetanidis, S. Valkaniotis, I. Karasante, V. Tsironi, P. Gaebler, D. Melgar, and T. Ocalan (2021). Source mechanism and rupture process of the 24 January 2020 Mw6.7 Doğanyol-Sivrice earthquake obtained from seismological waveform analysis and space geodetic observations on the East Anatolian Fault Zone (Turkey), *Tectonophysics*, 804, 228745.

Tinti, E., L. Scognamiglio, A. Michelini, and M. Cocco (2016). Slip heterogeneity and directivity of the ML 6.0, 2016, Amatrice earthquake estimated with rapid finite-fault inversion, *Geophys. Res. Lett.*, 43, 10,745– 10,752. doi: 10.1002/2016GL071263.

Trugman, D. T., S. X. Chu, and V. C. Tsai (2021). Earthquake Source Complexity Controls the Frequency Dependence of Near-Source Radiation Patterns, *Geophys. Res. Lett.*, 48, e2021GL095022.

Turhan, F., D. Acarel, V. Plicka, M. Bohnhoff, R. Polat, and J. Zahradník (2023). Coseismic faulting complexity of the 2019 Mw5.7 Silivri earthquake in the Central Marmara Seismic Gap, offshore Istanbul, *Seismol. Res. Lett.* 94 (1), 75–86.

Valentová, Ľ., F. Gallovič, and S. Hok (2021). Near-source ground motions and their variability derived from dynamic rupture simulations constrained by NGA-West2 GMPEs, *Bull. Seismol. Soc. Am.* 111 (5): 2559–2573. doi: doi.org/10.1785/0120210073.

Wang, Y., and S. M. Day (2017). Seismic source spectral properties of crack-like and pulse-like modes of dynamic rupture, *J. Geophys. Res. Solid Earth*, 122, 6657–6684. doi:10.1002/2017JB014454.

Wang, Z., W. Zhang, T. Taymaz, Z. He, T. Xu, and Z. Zhang (2023). Dynamic rupture process of the 2023 Mw7.8 Kahramanmaraş earthquake (SE Türkiye): Variable rupture speed and implications for seismic hazard. *Geophys. Res. Lett.*, 50, e2023GL104787.

Ward, S. N. (1994). A multidisciplinary approach to seismic Hazard in southern California. *Bull. Seismol. Soc. Am.*, 84(5), 1293–1309.

Wesnousky, S. G. (1999). Crustal deformation processes and the stability of the Gutenberg-Richter relationship. *Bull. Seismol. Soc. Am.*, 89(4), 1131–1137.

Withers, K. B., K. B. Olsen, Z. Shi, and S. M. Day (2018). Validation of deterministic broadband ground motion and variability from dynamic rupture simulations of buried thrust earthquakes, *Bull. Seismol. Soc. Am.* 109 (1): 212–228. doi: 10.1785/0120180005.

Worden, C. B., E. M. Thompson, J. W. Baker, B. A. Bradley, N. Luco, and D. J. Wald (2018). Spatial and Spectral Interpolation of Ground-Motion Intensity Measure Observations, *Bull. Seism. Soc. Am.*, 108, 866-875.

Wu, F., J. J. Xie, Z. An, C. H. Lyu, T. Taymaz, T. S. Irmak, X. J. Li, Z. P. Wen, and B. F. Zhou (2023). Pulse-like ground motion observed during the 6 February 2023 MW7.8 Pazarcık Earthquake (Kahramanmaraş, SE Türkiye). *Earthq. Sci.*, 36, 328–339.

Yagoda-Biran, G., J. G. Anderson, H. Miyake, and K. Koketsu (2015). Between-event variance for large repeating earthquakes, Bull. Seismol. Soc. Am. 105 (4): 2023–2040. doi.org/10.1785/0120140196.

Yue, H., and T. Lay (2020). Resolving complicated faulting process using Multi-Point-Source representation: Iterative inversion algorithm improvement and application to recent complex earthquakes, *J. Geophys. Res. Solid Earth,* 125, e2019JB018601.

Zahradník, J., and E. Sokos (2018). ISOLA code for multiple-point source modeling—Review, in Moment Tensor Solutions: A Useful Tool for Seismotectonics, S. D'Amico (Editor), Springer International Publishing, Cham, Switzerland, 1–28.

Zahradník, J., F. Turhan, E. Sokos, and F. Gallovič (2023). Asperity-like (segmented) structure of the 6 February 2023 Turkish earthquakes, *EarthArXiv*. Doi: https://doi.org/10.31223/X5T666.

8. List of included publications

1. Čejka, F., J. Zahradník, F. Turhan, E. Sokos, and F. Gallovič (2023). Long-period directivity pulses of strong ground motion during the 2023 Mw7.8 Kahramanmaraş earthquake, *Commun. Earth. Environ.,* 4, 413. https://doi.org/10.1038/s43247-023-01076-x
2. Čejka, F., Ľ. Valentová Krišková, S.Sgobba., F Pacor, and F. Gallovič (2024a). Ground-Motion Modeling of the 2016 Mw6.2 Amatrice, Italy, Earthquake, by a Broadband Hybrid Kinematic Approach, Including Empirical Site Effects, *Seism. Res. Lett*. https://doi.org/10.1785/0220230409
3. Čejka, F., S. Sgobba, F. Pacor, C. Felicetta, Ľ. Valentová, and F. Gallovič (2024b). Constraining Between-Event Variability of Kinematic Rupture Scenarios by Empirical Ground-Motion Model: A Case Study in Central Italy, *Bull. Seismol. Soc. Am.,* 114 (4): 2138–2150. https://doi.org/10.1785/0120230251